Si modification in hypereutectic Al-Si: Combining rapid solidification and alloying

by

Daniela Diaz Jimenez

A thesis submitted in partial fulfillment of the requirements for the degree of

Master of Science

in

Materials Engineering

Department of Chemical and Materials Engineering
University of Alberta

Abstract

Four alloys were studied to observe the effects of Rapid Solidification and alloying on the morphology of a hypereutectic Al-40Si. Impulse Atomization was used to produce the samples studied. This processing technique was used to attain high undercoolings and liquid cooling rates ranging 10^3-10^5 K/s, thus producing rapidly solidified microstructures. Chemically modified alloys include Al-40Si-1.5Ce, Al-40Si-9.2Mg, and Al-40Si-2.75Fe-2.75Mn-1.5Sc. The resulting microstructures were qualitatively analyzed by comparing the changes in primary Si morphology and distribution across different powder sizes for each alloy and across all alloys for specific powder sizes. Quantitative results include measured phase fractions of primary Si for all alloys, and halo and eutectic for Al-40Si and Al-40Si-1.5Ce.

The results presented suggest Ce and Mg additions are suitable for modifying primary Si shape and distribution in rapidly solidified Al-40Si. Both alloying approaches led to an improvement in primary Si distribution when produced at high cooling rates as compared to Al-40Si. Al-40Si-1.5Ce presents a similar primary Si morphology evolution to that seen in Al-40Si as cooling rate increases. This alloy also contains a large Al-halo vol%, which may be conducive to improved toughness in this alloy compared to Al-40Si. Primary Si morphology in Al-40Si-9.2Mg does not respond to changes in cooling rate. However, primary Si in this alloy consistently presents a small aspect ratio, which leads to a more homogeneous primary Si distribution in this alloy than in Al-40Si (particularly at slow cooling rates).

Acknowledgements

I would like start by thanking my supervisor, Dr. Hani Henein, who constantly challenged me throughout our work together. Thank you for never letting up and helping me become the researcher I am today. And thank you for showing me compassion even when I couldn't do so for myself.

Thank you to Dr. Abdoul-Aziz Bogno, who helped me immensely in my experimental work and who was an ever-present sounding board.

Thank you to my friends of the Advanced Materials and Processing Laboratory. You were all a constant reminder that I wasn't in this alone.

Thank you to my family, who, through the ups and downs of my degree, never let me feel alone.

Contents

List of Tables

List of Figures

xi

List of Symbols

- B: pre-exponential term in thermal conductivity equation of the cooling gas as a function of temperature

- C_d: drag coefficient

- C_o: nominal composition

- C_o^*: weighted eutectic tie line

- C_{pm}: specific heat of droplet

- C_s: solidus composition

- d: powder diameter

- D: diffusion coefficient

- f_s: solid fraction

- f_α, f_β: volume fraction of α, β phase in eutectic

- g: acceleration due to gravity

- G: eutectic thermal gradient

- Γ: Gibbs-Thomson coefficient

- H_a: alternate hypothesis

- h_{eff}: effective heat transfer coefficient

- H_o: null hypothesis

- k: partition coefficient

- k_m: thermal conductivity of droplet

- k_s: thermal conductivity of the cooling gas

- L: heat of fusion of Al-Si eutectic

- λ: eutectic spacing

- λ_a: average eutectic spacing

- λ_e: extremum eutectic spacing

- λ_m: minimum eutectic spacing

- λ_M: maximum eutectic spacing

- m: exponent in thermal conductivity equation of the cooling gas as a function of temperature

- $\overline{m}$: weighted liquidus slope

- m_α, m_β: liquidus slope

- μ: sample average

- μ_s: viscosity of gas at free stream temperature

- μ_∞: viscosity of gas at droplet's surface temperature

- n: sample size

- Nu: Nusselt number

- Pr: Prandtl number

- Re: Reynolds number

- ρ_g: gas density

- ρ_m: droplet density

- s: standard deviation

- s_p: pooled variance

- SR: scanning rate

- t: t-statistic

- T_{eut}: eutectic reaction temperature

- T_p: primary Si reaction temperature

- T_s: surface temperature of droplet

- T_∞: free stream gas temperature

- θ: contact angle

- v: droplet velocity

- V: eutectic growth velocity

Chapter 1

Introduction

Hypereutectic Al-Si alloys benefit from good wear resistance provided by the Si grains in their microstructure while also being relatively lightweight. One limitation that has stopped these alloys from being widely used is the hinderance that the faceted nature of Si grains poses to their toughness. Si morphology modification has, however, been shown to be attainable through rapid solidification (RS) and alloying. Morphology modification introduces the possibility of reducing the downsides associated with the faceting tendency of Si. Laser Powder-Bed Fusion (LPBF), which is a RS process, can potentially be used with hypereutectic Al-Si and result in a more desirable primary Si morphology than would be obtained under slow cooling conditions. Additionally, alloy selection can be expanded to include more complex alloy systems to integrate the RS and alloying modification approaches.

This work uses four alloys (Al-40Si, Al-40Si-1.5Ce, Al-40Si-9.2Mg, and Al-40Si-2.75Fe-2.75Mn-1.5Sc) produced by Impulse Atomization (IA) to explore:

- the effects of RS on the microstructure of hypereutectic Al-Si,

- the effects of alloying with Ce, Mg, and mixed Fe/Mn/Sc on the microstructure of RS hypereutectic Al-Si, and

- the effects of cooling rate on chemically-modified hypereutectic Al-Si.

Qualitatively, this work describes the scale and distribution of the microstructure produced under varying liquid cooling rates, as well as the morphology of the primary and eutectic Si present in said microstructure. Quantitatively, microstructure distribution is assessed as a function of liquid cooling rate. For Al-40Si, the correlations between eutectic spacing, growth velocity, undercooling, and thermal gradient are presented. Best efforts are made to compare the microstructures of IA samples to those expected from the Gulliver-Scheil (G-S) solidification model. This includes qualitative analysis of the differences in phases observed in IA from those expected from G-S, and quantitative comparisons between the amount of each component present in the microstructure and its G-S value. These results are used to indentify the deviation from equilibrium observed in each alloy and provide a basis for comparison across all alloys. Ultimately, the combined qualitative and quantitative results presented in this work are used to suggest potential alloy systems for further experimentation in an LPBF apparatus.

Chapter 2

Literature Review

2.1   Al-Si System

Th Al-Si phase diagram is shown in Figure 2.1. A eutectic reaction producing both phases occurs at 12.6wt% Si and 577°C. On the Al-rich side of the system, a liquidus describing the production of primary α extends from 660.5°C and 100% Al to the eutectic point. On the Si-rich side of the system, a liquidus associated with the production of primary Si phase extends from the eutectic point to 1414° C and 100% Si. The α phase is rich in Al and has a maximum Si solubility of 1.65wt% at the eutectic temperature [1].The Si phase has no Al solubility. Hypoeutectic Al-Si alloys solidify by primary α growth and subsequent eutectic growth. In hypereutectic alloys, the focus of this thesis, primary Si solidifies first, and the eutectic subsequentyly forms.

2.2   Alloy Properties

Individually, α and Si display very different properties. α, mainly composed of Al, is a soft and ductile metallic phase. Si is a non-metallic phase with covalent bonds, which produces hard but brittle grains. Additionally, while α grows isotropically, Si growth is anisotropic [1]. This means that Si grains tend to have sharp surfaces, which can serve as locations for stress

3
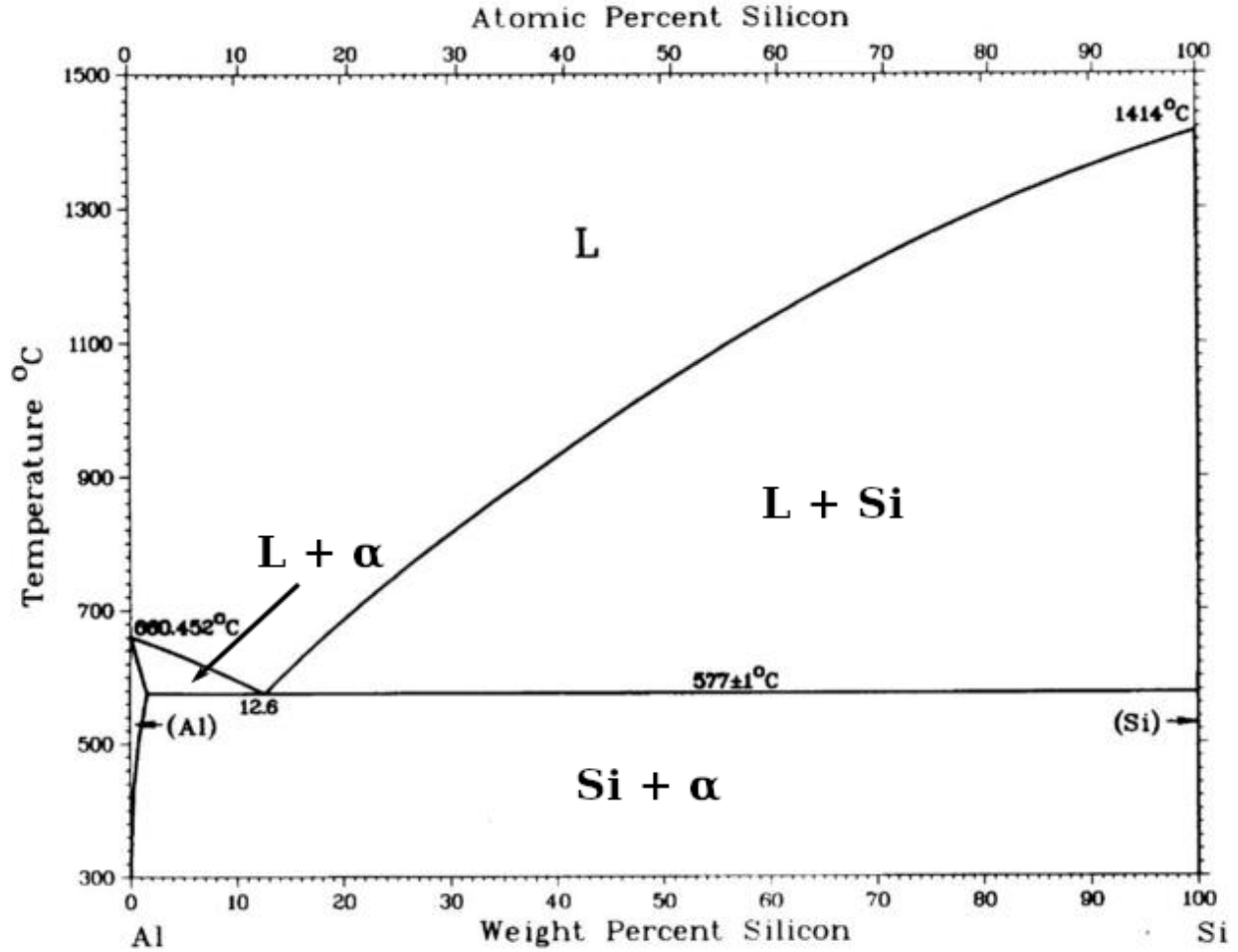
Figure 2.1: Al-Si phase diagram [2]

concentration and hinder the toughness of the alloy. The interaction of a ductile matrix and harder particles distributed througout the same makes Al-Si alloys behave as composites. This composite-like behaviour has important implications on the role that Si morphology, size, and distribution have on the overall properties of these alloys.

In hypereutectic Al-Si, wear resistance is strongly correlated to the size and distribution of primary Si grains [3]. Smaller and more homogenously distributed primary Si exhibits better wear resistance. This tendency is explained by the wear mechanism observed by primary Si. When tested under small loads, primary Si particles serve as load-bearing elements, allowing reduced wear to the matrix. Under very high loads, primary Si grains can fracture, making

them easier to detach from the matrix. Multiple works have identified that coarser grains are more prone to fracturing, increasing the possibility of third-body wear mechanism due to debris from fractured Si serving as abrasive media and increasing the wear rate of the material [4, 5].

Si morphology most notably affects toughness due to the impact morphology has on stress concentration. Si grains are commoly faceted and present sharp surfaces. For this reason, the interface shared between these grains and the surrounding matrix can be a location of high stress concentration. Primary and eutectic Si morphology can vary in response to changes in solidification conditions. Careful consideration of the interaction between thermal history and Si morphology can be used to promote the formation of Si grains with minimal faceting. This reduction in faceting and corresponding decrease in stress concentration can reduce the tendency for crack initiation at the surface of Si grains, thereby enhancing toughness. In particular, rapid solidification and alloying have been widely studied for their effect on Si morphology. Sections 2.4 and 2.7 delve into the available literature for these modification mechanisms.

2.3   Si growth mechanism

Si crystals form a Face-Centered Cubic (FCC) lattice and follow a cF8 diamond cubic prototype [1]. During solidification, Si growth directions show strong anisotropy, effectively limiting Si growth to a few specific directions, thus producing faceted particles. Under near equilibrium conditions, growth tends to be fastest in the <112>family of directions, while the slowest growth is commonly observed in <111>[6, 7]. These tendencies are explained by {111} being the closest-packed planes FCC lattices. Due to their anisotropy, Si crystals have a tetrahedral equilibrium habit bound by six {111} planes.

Atomic attachment in Si grains is generally accepted to occur by the Twin-Plane Re-Entrant mechanism (TPRE) [8]. Under this growth mode, the most basic Si unit is made up

of two tetrahedra sharing a twin relationship, forming an octahedron bound by eight {111} planes (Figure 2.2a). The TPRE mechanism relies on the presence of twin planes to create energetically favourable sites for atomic attachment. In a basic Si octahedron, which contains a single twin plane, the intersections of {111} planes produce three 219° angles (ridges) and three 141° angles (re-entrant corners) on the outer surface of the crystal. Re-entrant corners are preferable sites for growth, as a smaller number of bonds need to form for an atom to attach (in comparison to ridges and {111} facets). In crystals containing a single twin plane, growth at re-entrant corners eventually forms ridges at each of these locations, limiting growth (Figure 2.2). As shown in Figure 2.3, when a second twin plane is introduced to the original crystal, six re-entrant edges become available for growth. More importantly, growth at these locations forms more re-entrant edges, allowing the crystal to continue growing while only subject to the availability of Si solute in the liquid around it.

(a) Twinned tetrahedra   (b) Ridge-bound octahedron
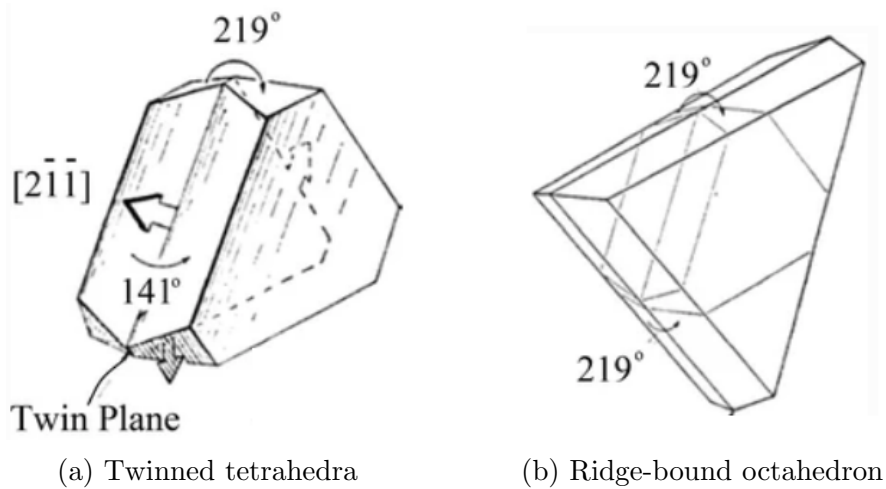
Figure 2.2: TPRE growth with single twin plane [6]

2.4 Si morphology

Primary and eutectic Si can take on various morphologies. Processing conditions play an important role in defining the morphologies that form in an alloy. This section discusses the existing understanding of how the selection of specific processing conditions can determine

(a) Twinned tetrahedra   (b) Formation of new re-entrant edges
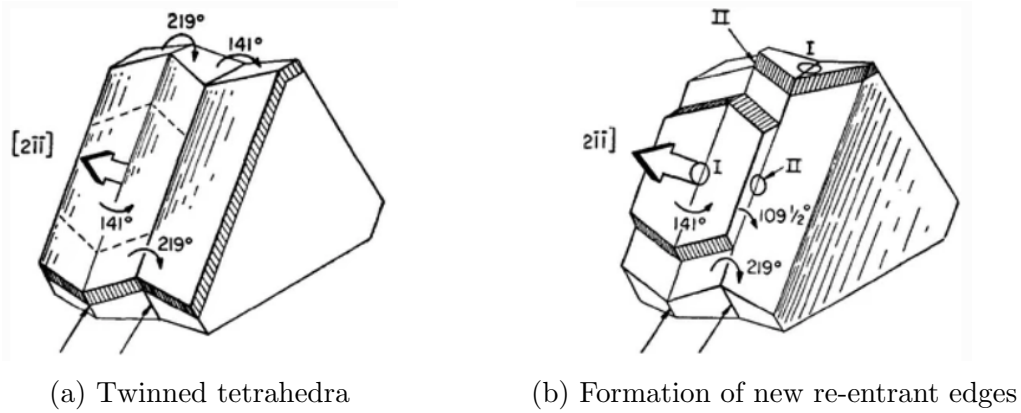
Figure 2.3: TPRE growth with two twin planes [6]

the formation of a given morphology.

2.4.1 Primary Si

Primary Si often forms one of three morphologies: star-like, plate-like, and octahedral. This section describes how melt conditions may affect the predominant morphology formed for a given alloy.

2.4.1.1 Star-like Si

The star-like morphology of primary Si is characterized by the presence of five branches growing radially from a single point (Figure 2.4). This morphology has been observed under both slow and rapid cooling conditions [9, 10]. Star-like Si grains arise from decahedral nuclei bounded by {111} planes [11]. These nuclei are made up of five Si tetrahedra that share a common <110>axis. Within the decahedral nucleus, five twin boundaries separate the individual tetrahedra. Generally, adjacent twin planes are oriented at 70.5° from each other [10]. The magnitude of these angles means a 7.5° mismatch exists within the particle. Kobayashi and Hogan [10] and Pei and De Hosson [9] identified the presence of small-angle grain boundaries (SAGB) to account for the mismatch. Kobayashi and Hogan [10] found a single SAGB, while Pei and De Hosson [9] found multiple SAGB distributed throughout the particle. The strain introduced by the mismatch of the tetrahedra in the nucleus is

thought to explain the branching observed in this morphology. During the first stages of growth, equiaxed growth is stable due to the low surface energy of {111} planes and low twin-boundary energy. As the nucleus becomes larger, the strain energy contribution of the 7.5° mismatch in the particle becomes too large and branching occurs.
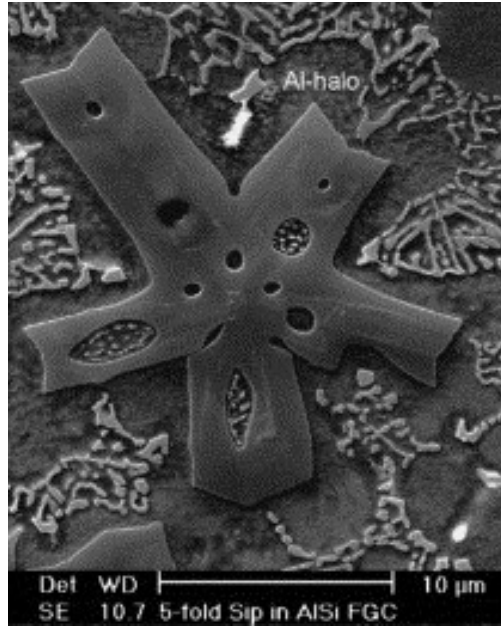
Figure 2.4: Star-like primary Si [9]

Regarding the formation of decahedral nuclei, Kobayashi and Hogan [10] suggest the presence of tetrahedral Si clusters in the liquid prior to solidification. This is supported by a Bernal's dense-random-packing model of geometry in liquids [12]. This model considers a monoatomic liquid near its freezing point to be made up of polyhedral clusters, of which the majority are tetrahedra.

Pei and De Hosson [9] pose a case of particular interest due to the difference in morphology observed under different thermal cycles. In this study, Al-40Si was laser clad onto a commercial Al substrate. The microstructure at the free surface of the cladding contained a larger proportion of star-like Si than that closest to the substrate. Temperature field modelling of the process indicates the free surface experienced longer periods under high heat input than did the material closest to the substrate. The difference in heat input provides

the conditions for more material to fully melt at the free surface than near the substrate. This argument would have more of the material near the substrate remaining solid than at the free surface throughout the cladding process. This means that nucleation is more likely to arise from molten material at the free surface than near the substrate. The larger proportion of star-like Si at the free surface thus supports the understanding that decahedral nuclei arise from the liquid by attachment of separate tetrahedra.

2.4.1.2 Plate-like Si

Plate-like primary Si (Figure 2.5) has been reported under regular casting conditions [13] and various extents of Rapid Solidification (RS) [14, 15]. The widest surface in particles with this morphology presents {111} facets. As can be seen in Figure 2.6, the cross section of a plate-like particle contains multiple twin planes. Crystallographically, these particles are bound by {111} facets on their widest surface and follow <110>on their logest dimension. This orientation indicates <211>growth directions, and suggests growth of this morphology occurs by the TPRE growth mechanism. The tips of plate-like particles form 120° or 240° angles, with the 120° angles serving as potential re-entrant corners for TPRE growth.
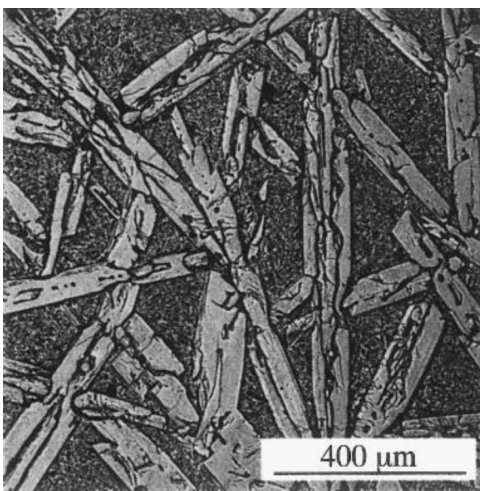
Figure 2.5: Plate-like primary Si [14]
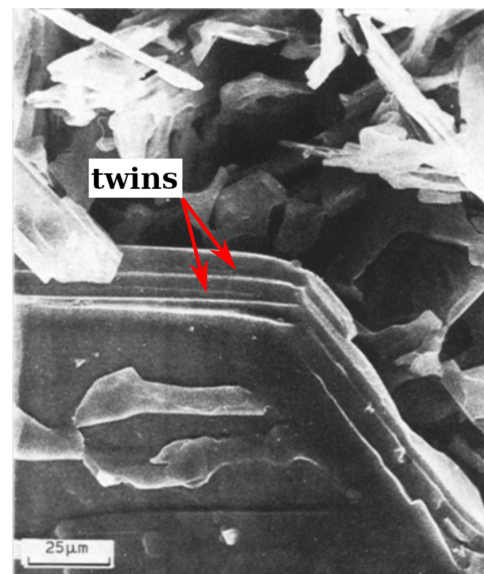
Figure 2.6: Twinning in plate-like primary Si [13]

9

Liu et al[14] and Ge et al[15] provide a good basis to discuss the effects that RS imposes on plate-like primary Si. These works test the same composition (Al-50at%Si) under different RS techniques. Liu et al [14] used Electromagnetic Levitation (EML), imposing large undercoolings on the molten metal. Ge et al [15] produced droplets through Drop Tube Atomization, allowing for high cooling rates to be achieved. In both cases, the conditions closest to equilibrium (undercooling: 10-70 K [14]; cooling rate: 500-1,000 K/s [15]) produced microstructures with large plate-like Si, much like those reported for regular casting conditions. As solidification conditions became more rapid (undercooling: 208-320 K [14]; cooling rate: 2,000-3,500 K/s [15]), primary Si grains appeared to break down into more granular shapes, although they generally maintained some semblance to the plate-like morphology. Both studies also found stratitified deposits of Al within and around primary Si. These are likely formed due to insufficient diffusion of Al away from the growing grain during solidification. These deposits subtly change as cooling rate increases. Deposits encased within a single primary Si grain become less prevalent as cooling rate or undercooling increase, probably due to higher supersaturation of Al in primary Si. The deposits surrounding primary Si increase in size as solidification becomes more rapid. An extreme case of this behaviour occured for ΔT=320 K (largest undercooling tested by Liu et al [14]), with the deposits becoming large enough that no eutectic matrix forms. The widening of Al deposits that accompanies plate-like Si break-up thus suggests that solute buildup ahead of the solidification front plays a role in primary Si grain refinement under RS conditions. The formation of an Al-rich region in hypereutectic Al-Si alloys is well-documented and commonly refered to as halo formation. Section 2.5 describes the accepted mechanism for this phenomenon.

2.4.1.3   Octahedral Si

Octahderal primary Si is produced under a wide range of solidification conditions. This morphology is particularly common in phosphorus-modified alloys [16]. Octahedral growth does not occur by the TPRE mechanism, but is rather diffusion-controlled. Despite the

difference in growth mechanism, the resulting particles are still faceted due to high anisotropy of Si growth directions. Xu et al [17] describe three growth stages for this morphology: spherical, sub-octahedral, and octahedral Si growth (Figure 2.7).
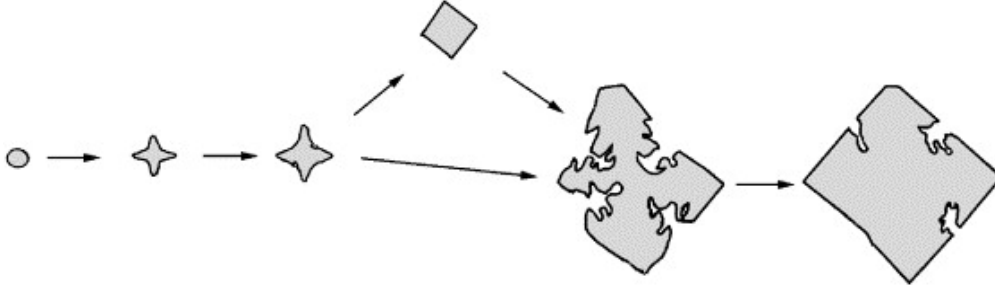
Figure 2.7: Growth stages of octahedral morphology [17]

Spherical growth is thought to occur as a result of microsegregation in the liquid, which allows the formation of small nuclei growing isotropically. Once the nucleus grows beyond a critical size, six hillocks form on the surface in <100>directions. Once the liquid ahead of the tip of each hillock becomes too saturated with Al, secondary branches form in <110>directions. These secondary branches grow until they connect the tips of adjacent primary branches. This growth sequence results in the formation of a skeletonized octahedron (Figure 2.8). During this process, there is also atomic attachment on <111>, which forms {111} facets. At this stage, these facets are relatively close to the original nucleus and do not line up with outer edge of the octahedral skeleton.

During the octahedral growth stage, differences in impurity concentration at different locations in the particle lead to the formation of distinct types of octahedron. Figure 2.9 shows the distinctive surface of perfect and imperfect (or hopper) crystals. These two crystal shapes differ in the extent of the formation of {111} facets. A perfect octahedral crystal is fully dense, with the space that was originally empty in the octahedral skeleton now filled by Si in {111} planes. In contrast, hopper crystals present gaps in their {111} facets. Growth of the {111} facets begins at the corners and edges of the octahedral skeleton, and the centre of these planes is the last part to solidify. This means that Al solute is pushed toward the
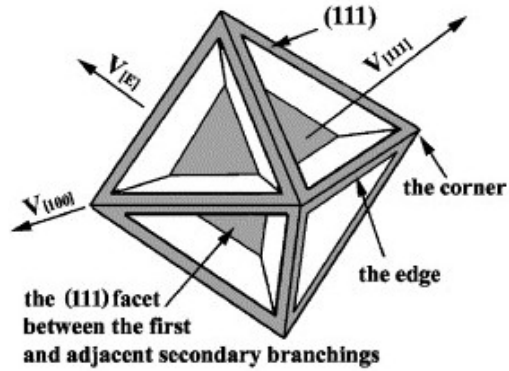
Figure 2.8: Skeletonized octahedron produced by end of sub-octahedral growth [17]

centre of these facets, and is thus more concentrated at these locations than at the edges. This is combined with solute near the corners and edges of the particle being easier to diffuse into the bulk of the liquid due to the diffusion field around them. This difference in Al concentration introduces a difference in driving force for further growth of the crystal. {111} facets, for which further diffusion of Al is most difficult, thus stop growing before <100>and <110>branches do, causing a deviation from perfect octahedrons and producing hopper crystals instead.
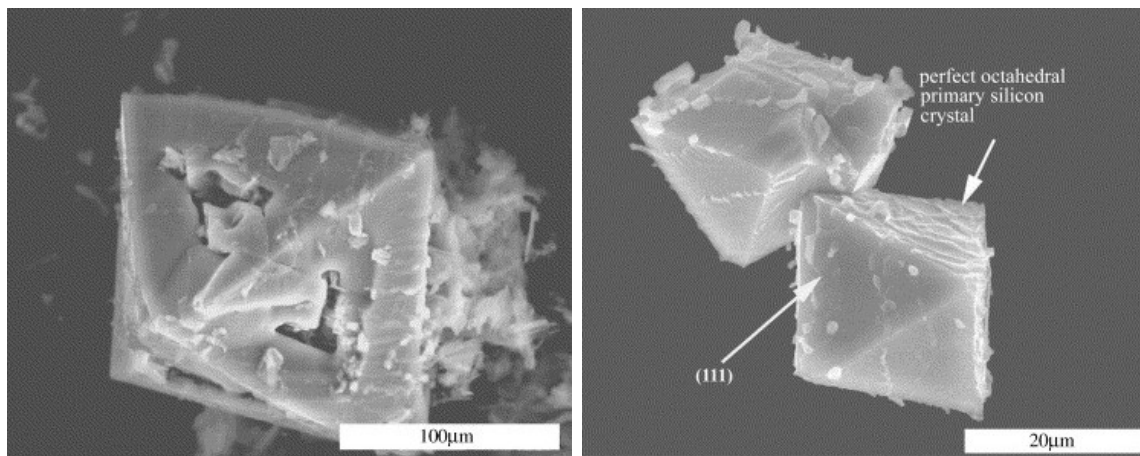
(a) Hopper octahedron

(b) Perfect octahedron

Figure 2.9: Possible shapes of octahedral primary Si [17]

2.4.2 Eutectic Si

Eutectic Si can take on three main morphologies: flaky, fibrous, and globular. As shown in Figure 2.10, these morphologies differ in average Si grain size, extent of faceting, and distribution. As outlined in Section 2.2, these differences lead to variations in the performance of microstructures containing each morphology. The faceted nature of flaky Si suggests that microstructures containing this morphology can experience higher stress concentration and are more likely to fail prematurely than those containing globular Si. Flaky Si also contains larger and less homogeneously distributed grains than globular Si, with the former contributing less to the microstructure's wear resistance than the latter.

(a) Flaky eutectic   (b) Fibrous eutectic   (c) Globular eutectic
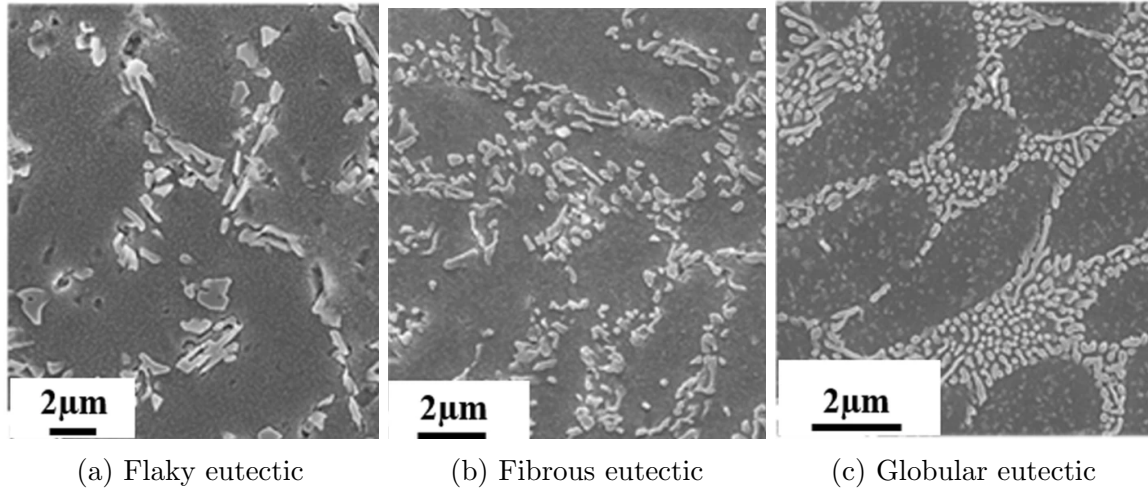
Figure 2.10: Eutectic Si morphology [18]

In the literature, both RS and alloying have been used to modify predominant eutectic morphology. Hearn et al [18] analyzed the local solidification conditions that produced different eutectic Si morphologies. This study, carried out on Al-10wt%Si powders found the local cooling rate at the solidification front to be a defining factor for the morphology formed. Specifically, they found transitions in the predominant morphology to occur at 60K/s (flaky → fibrous), 350 K/s (fibrous → globular + fibrous), and 1600 K/s (globular + fibrous → globular). Common elements used for modification include Na, Sr, Ca, and various rare-earth elements. A detailed description of the modification mechanisms attributed to these elements

is provided in Section 2.7.

2.5   Halo Formation

An important aspect of hypereutectic Al-Si solidification is the reported formation of an α-Al envolope surrounding primary Si. This feature is commonly referred to as a halo. Halo formation is not unique to Al-Si. Various binary faceted-nonfaceted alloy systems have been studied for their tendency to form haloes of the nonfaceted phase surrounding the faceted one.

Sudquist et al [19] were the first to propose a possible mechanism for the formation of haloes. They suggested relative ease of nucleation as a factor to predict halo formation. Consider a binary alloy system containing α and β phases, and which forms a eutectic made up of both phases. These authors assume the concept of nonreciprocal nucleation of alloy pairs. This dictates that if α is a good nucleant for β, then β is likely to be a poor nucleant for α. In the scenario where this assumption holds true, a large secondary undercooling can be expected when β is the primary phase. Likewise, a smaller undercooling is expected when α is the primary phase. In each of these cases, undercooling is accompanied by an adequate change in composition of the liquid as dictated by the metastable extension of the liquidus. Growth of the non-primary phase is thus required to bring the liquid back to the eutectic composition in order for eutectic solidification to occur. Mathematically, this mechanism would form haloes that are proportional in size to secondary undercooling.

In her work on the possible shapes of coupled zones in organic binary systems, Kofler [20] identified the formation of haloes in an azobenzol-trional system when azobenzol, but not when trional, was the primary phase. In this work, Kofler proposes a mechanism for halo formation that includes the effect of the shape of the coupled zone. Consider a system where the coupled zone is skewed to one side of the phase diagram (Figure 2.11). If during solidification β is the primary phase and there is significant undercooling prior to secondary
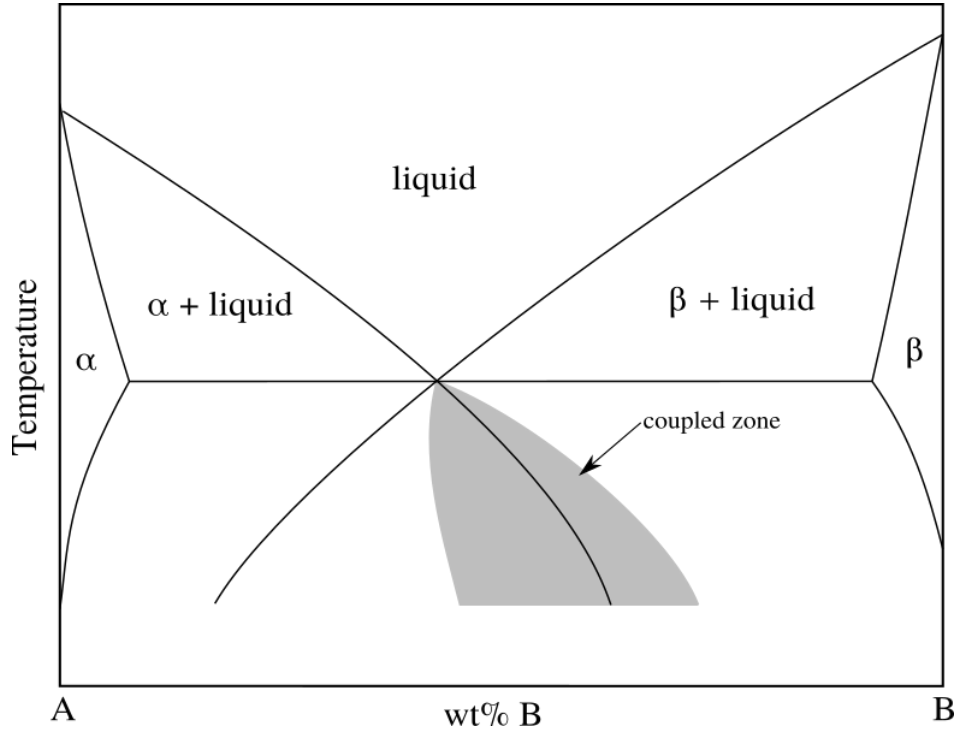
Figure 2.11: Binary phase diagram with skewed coupled zone

nucleation, the liquid composition dictated by the liquidus extension exists outside of the coupled zone. In this region (to the left of the coupled zone), α grows more rapidly than β, and thus growth of α occurs readily upon nucleation. This solidification step also allows for the composition of the liquid to move back to the coupled zone. In contrast, if solidification takes place such that α is the primary phase, the composition of the liquid at the moment of secondary undercooling is likely to exist within the coupled zone. In this case, eutectic growth would occur without prior halo formation.

To test the validity of these mechanisms, Gigliotti et al [21] studied four faceted-nonfaceted systems. Of these, three held to Sudquist's nonreciprocal nucleation assumption (Sn-Bi, Pb_2Bi-Bi, and Al-CuAl$_2$), and one (Al-Si) did not. In Al-Si, both phases are relatively poor nucleants for the other. In the systems with nonreciprocal nucleation, when the phase that was a good nucleant was the primary phase, halo formation occur. And when the poor nucleant was the primary phase, no halo was present. These results contradict the mechanism

15

proposed by Sundquist et al. In each case, including that of Al-Si, the faceted phase was primary when a halo formed, and the nonfaceted phase made up the halo. Likewise, the coupled zone in each of these systems is skewed toward the faceted phase. This is consistent with growth rate determining halo formation, as proposed by Kofler.

2.6 Rapid Solidification

Rapid Solidification (RS) processes are distinguished by a large driving force for solidification. This induces rapid growth of the solid once nucleation occurs. This rapid growth limits diffusion distance during solidification, and produces finer microstructures than would be present under casting conditions. By forcing solidification to occur far from equilibrium conditions, rapid growth tends to cause supersaturation in the formed phases and has the potential to produce metastable phases. In general, RS can be achieved through rapid cooling or by imposing large undercoolings on the molten material [22]. Common RS processes include various atomization techniques, twin roll casting, laser remelting, directional solidification, and electromagnetic levitation. This section introduces Laser-Powder Bed Additive Manufacturing and outlines the factors that make it a RS process. The Gulliver-Scheil solidification model is also presented as an appropriate starting point to use when analyzing features present rapidly solidified microstructures.

2.6.1 Laser Powder-Bed Additive Manufacturing

Laser Powder-Bed Additive Manufacturing processes (LPB-AM) are used for the creation of components through a layer by layer formation mechanism. LPB-AM is an umbrella for two main processing approaches: Laser Sintering (LS) and Laser Melting (LM). Figure 2.12 shows the equipment set-up used for LPB-AM. Prior to processing, component design is carried out through Computer-Aided Design. This is used to formulate vectors for the motion of the equipment (laser and powder bed) during production. During processing, a laser is used to

selectively apply heat to the material, and the mechanized powder bed distributes individual layers of powder. The use of a laser in these processes introduces rapid heating and cooling to the material. Typical cooling rates for LPB-AM range 10^3-10^7 K/s [23, 24], meaning LPB-AM processes produce rapidly solidified microstructures.

The equipment set-up and process mechanics of LS and LM are very similar. The main difference between them lies in the metallurgical phenomena taking place within each process [25]. LS, as its name suggests, relies on sintering of individual powders. Given the short processing time, LS may rely on partial melting of the material. When using pre-alloyed powder, the target temperature for the material is set between its solidus and liquidus. This region is commonly referred to as the mushy zone. This temperature selection allows for the coexistence of solid and liquid material, so that the available liquid can be used as a binder for the remaining solid. This process, however, requires highly precise temperature control, as the material's temperature must remain within the mushy zone. Due to rapid thermal cycling and localized heat input, this condition is not usually met. For this reason, LS tends to produce components that are not fully dense when using pre-alloyed powders. These can also display heterogeneous microstructures and properties, and commonly require post-processing. In contrast to LS, LM works by fully melting the powder exposed to the laser. The solidification of the entire material as a single unit allows for the production of components of near-net density, improved surface smoothness, and a more homogeneous microstructural distribution. This use of fully molten metal can also be accompanied by instability in the molten pool, which can produce porosity. Additionally, the melting and subsequent solidification of the material can cause solidification shrinkage and lead to stress accumulation. These downsides are addressed by optimization of processing parameters in the literature of LM.
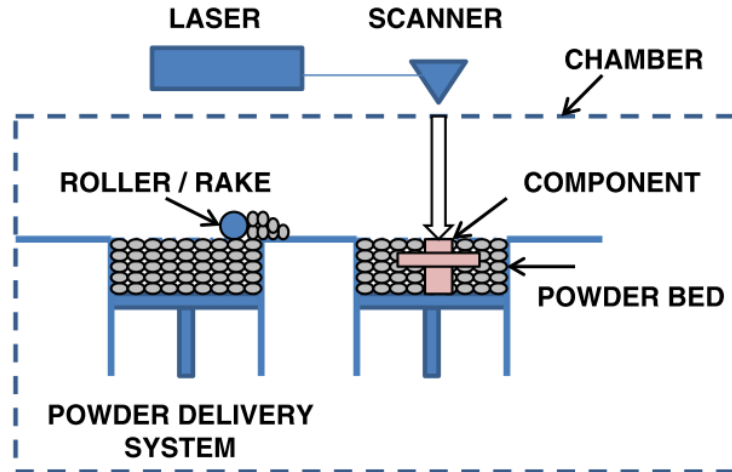
Figure 2.12: Laser Powder-Bed process setup [26]

2.6.2 Gulliver-Scheil solidification

The microstructures obtained through RS differ from those obtained via casting processes due to fundamental differences in solute diffusion during processing. These differences are best explained as products of deviation from equilibrium. Two important concepts related to the variation in extents of deviation from equilibrium are global and local equilibrium. Global equilibrium of a system is described by its equilibrium phase diagram. This condition produces microstructures in which each phase has a homogeneous composition, which is indicated by the solidus of that phase. This homogeneity results from a very slow growth velocity (slower than diffusion), which allows for solute redistribution to bring the system to its most thermodynamically state. Due to the slow growth velocity required, global equilibrium is highly uncommon in typical processes. In contrast to global equilibrium, local equilibrium describes a solidifying system in which the composition of the solid varies across individual grains according to temperature of the solid-liquid interface during growth. This condition more closely fits a majority of processes involving solidification, as it exists when the difference between solidification growth velocity and diffusion is smaller than it is for global equilibrium.

18

The Gulliver-Scheil (G-S) solidification model is a common way of modelling the solidification of alloys under local equilibrium conditions [27]. G-S solidification assumes no diffusion occurs within the solid. This represents the formation of a solid containing a nonzero composition gradient. A second assumption of this model is that diffusion in the liquid is very fast, allowing the remaining liquid to have a homogeneous composition at any point during solidification. Mathematically, the G-S model is based on the mass balance of the solute rejected from the solid and re-distributed in the liquid as the solid grows. The final form of the G-S model is presented in Equation 2.1, where C_S is solidus composition, $k = \frac{C_S}{C_L}$ is the partition coefficient, C_o is nominal composition, and f_S is solid fraction.

$$C_S = kC_o(1 - f_S)^{k-1} \tag{2.1}$$

The G-S model allows for a more realistic estimate of the microstrucural distribution within the solid than what is provided by the equilibrium phase diagram. G-S predictions are not expected to appropriately describe microstructures formed under RS, but they provide a good starting point to which these microstructures can be compared. For this reason, G-S solidification will be used as a starting point in the discussion of the alloys examined in this document.

2.7 Alloying

Chemical modification of Al-Si casting alloys has long been used as a way to refine microstructure and modify the morphology of primary and eutectic Si. Section 2.7.1 outlines the most common modification approaches for hypereutectic Al-Si and analyzes their potential benefit for use in rapidly solidified Al-40Si. Section 2.7.2 introduces the use of macroalloying as a way of refining and modifying primary Si by changing amount of primary Si predicted from the system's equilibrium.

2.7.1 Conventional Approaches

This section discusses the mechanisms at play in the modification of Al-Si by alloying with P, Na or Sr, and various Rare-Earth Elements.

2.7.1.1 Enhanced Nucleation

Phosphorus is perhaps the best-established alloying addition for the modification of primary Si morphology. When added to the Al-Si melt, P reacts with Al to form AlP at high temperatures (m.p.(AlP)=2530 °C). This compound thus serves as a preferential site for heterogeneous nucleation of primary Si [28, 29]. Having the same lattice structure (FCC) and a lattice parameter similar to that of Si (0.542 nm for AlP vs 0.545 nm in Si), AlP is a particularly good compound for this purpose, as epitaxial growth of primary Si can easily occur on the surface of the existing AlP grains [3, 30]. Use of AlP thus enhances the nucleation rate in the melt and allows formation of a larger number of primary Si grains, yielding smaller individual grains (which also tend to be equiaxed). Despite these benefits, use of P in an Al melt introduces Occupational Health and Safety (OHS) hazards that can severely hinder its industrial adoption. AlP, when in contact with moisture, produces toxic and flammable phosphine gas [31, 32].

The proven effectiveness of AlP as a nucleation agent opens up the possibility of other similar compounds that may achieve the same goal. A large range of FCC compounds was considered as a safer alternative to AlP. Of the compounds considered, six have a lattice parameter that is sufficiently similar to that of Si to be considered feasible nucleation agents. However, use of any of these compounds presents difficulties for the intended purpose, as they present either health hazards or physical properties that are incompatible with Al-40Si. A more detailed discussion of the compounds considered and the limitations of their use can be found in Appendix A.

2.7.1.2 Twin Density Increase

Sodium has long been used for modification of hypoeutectic Al-Si alloys commercially. The effectiveness of this addition is associated with an increase in twinning density, which is best described by the widely accepted impurity-induced twinning theory (IIT) [33]. IIT describes the modification of Si by twinning via attachment of atoms of appropriate radius onto preferential Si attachment sites. This selective attachment introduces twinning at the location where the impurity is attached, thereby creating more locations for Si attachment and allowing to disrupt the growth of the existing crystal. By the nature of crystal growth taking place, the modification achieved in Si yields a microfacetted crystal, rather than a continuous surface. An example of this behaviour in primary Si is presented in Figure 2.13.
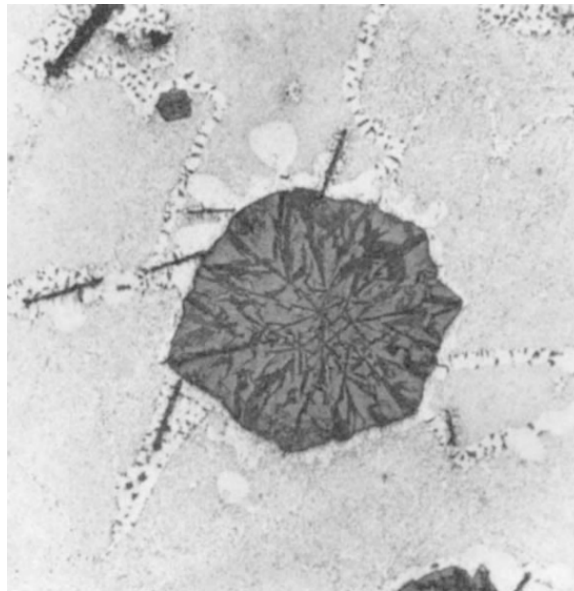
Figure 2.13: Na-modified primary Si [34]

The initial formulation of IIT established the ratio of the modifying element's atomic radius to Si atomic radius as a key characteristic in determining the effectiveness a given element might have in modifying Si morphology. Based on the assumption that the modifying element causes the Si stacking sequence to miss a monolayer step, the ideal ratio of modifier to Si radii is 1.65. Based on this ratio, various possible modifying elements have been identified,

21

such as Sr, Eu, Ca, Yb, La, Na, Ce, Pr, Nd, Sm, and Y. From this list, substantial research supporting twinning as the modifying mechanism only exists for Sr and Na[33, 34, 35].

With respect to its applicability for RS in Al-Si, this modification mechanism is largely absent from the literature. One of the most relevant accounts comes from Lu and Hellawell, who first introduced IIT. They studied the change in incidence of twinning when eutectic Al-Si was quenched [36]. In comparing slowly cooled and quenched alloys, the quenched alloy presented a much lower twinning density than its slowly cooled counterpart did. They correlated these observations with the nature of Si growth at high undercoolings and identified that the increasing driving force for growth in non-preferential directions (i.e [110]) decreased the crystal's reliance on twinning as a growth mechanism with increasing undercooling. These findings suggest a likely loss in modification efficiency should be expected when using this mechanism under RS conditions.

2.7.1.3 Solute Buildup

Rare earth elements (REE) have also been considered as possible modifiers of primary and eutectic Si in the existing literature. Many of these attempts followed their apparent suitability to modify Si via IIT, as predicted by the radius ratio criterion set forth in this theory. To date, however, the modification mechanism at play in RE-modified Al-Si alloys remains a subject of debate. Nogita et al. studied the effect of fourteen REE on the morphology of eutectic Si in a hypoeutectic Al-Si alloy [37]. The breadth of alloying elements used in this study was selected largely to test the applicability of the IIT radius ratio criterion as a sole means of identifying elements that modify Al-Si alloys by this mechanism. Castings were produced for various Al-10Si alloys modified with REE, allowing for eutectic nucleation and growth temperatures to be measured for each casting, and producing samples to study the resulting eutectic Si morphology. Of the tested REE, only Eu-modified alloys showed changes in eutectic Si morphology, while the rest presented varying levels of refinement. This is in contrast to Eu having the second closest r_{REE}/r_{Si} to the 1.65 identified in IIT (r_{Eu}/r_{Si}=1.70). Yb,

which was also tested in this study but did not show eutectic modification, has r_{Yb}/r_{Si}=1.65. This discrepancy points to the IIT radius ratio criterion being useful but not solely telling of the applicability of REE as modifiers for Al-Si alloys. In contrast to this study, multiple cases of REE fully modifying eutectic Si do exist [38]. The most glaring difference between these accounts is the composition of the studied alloys, with those reporting modification referring to hypereutectic alloys. A more conclusive aspect of existing studies on REE modification is a more universal agreement that differences in twinning density between unmodified and REE-modified alloys cannot fully explain the extent of morphology modification between the two [38, 39, 40]. These key inconsistencies between REE modification of Al-Si and IIT thus indicate a need to consider REE as a category of modifiers separate from Na and Sr.

Studies testing the effect of REE content on microstructure generally agree that, with additions of up to 3% REE, increasing REE content tends to refine primary and eutectic Si microstructure [38, 41, 42, 43]. This trend, however, tends to break down at a relatively low REE content, with further increases causing coarsening of Si phases [41, 42, 43]. These results indicate that any addition of REE to Al-Si alloys must carefully consider the REE content to ensure optimal microstructure and properties.

To understand the modification mechanism introduced by REE, Chang et al. studied the elemental distribution of a mischmetal-modified Al-21Si alloy [44]. Figure 2.14 includes this distribution across two primary Si grains and the matrix between them. Within primary Si grains, there is low RE content (0.2%), while these elements were highly concentrated in the matrix (5.3%). These results are not unexpected, as the solubility of REE in Si is generally accepted to be negligible. However, they do provide some insight into the possible mechanisms by which REE induce Si modification. With this study resulting in primary Si modification from star-like to polyhedral (Figure 2.15), as well as the latter morphology grains being much smaller than the former, the authors suggest the addition of REE supressed anisotropic growth in the alloy. Based on the elemental distribution observed, they present the possibility of changes in the surface energy of primary Si (due to supersaturation of RE

in the crystal) or the solid-liquid interfacial energy (due to the buildup of REE solutes at the solidification front).
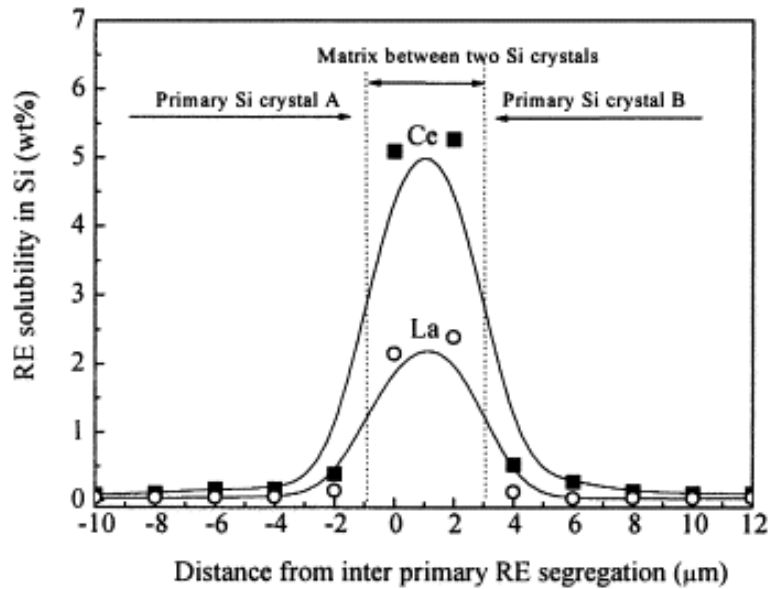
Figure 2.14: REE concentration profile in and around primary Si [44]
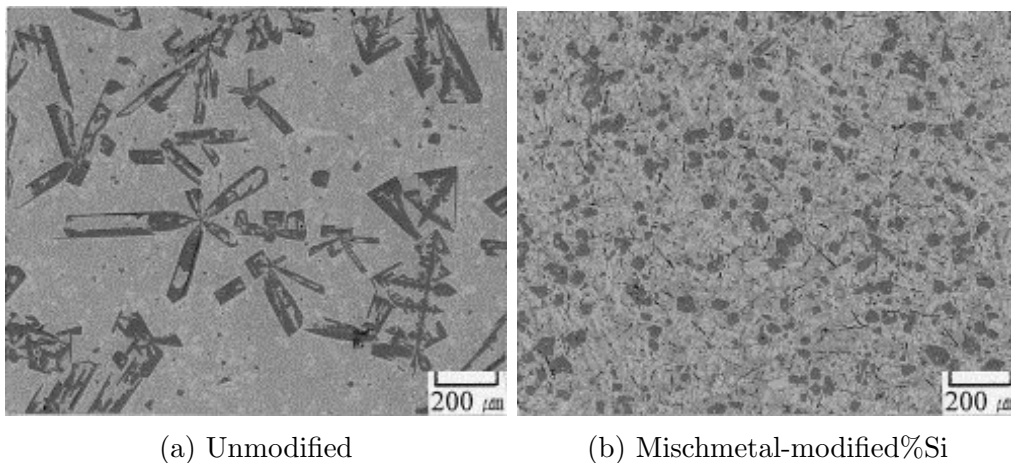
(a) Unmodified   (b) Mischmetal-modified%Si

Figure 2.15: Microstructure of cast Al-21wt%Si [44]

In a separate paper, the same authors further their study of REE-modified Al-21Si by casting this alloy in a wedge mold, achieving cooling rates between 33 and 130°C/s [38]. Just as before, they found increasing REE content to refine primary and eutectic Si, with samples containing 2% REE or more also presenting modified primary Si crystals. Two

contributions from this study are worth noting. The first one, resulting from differential thermal analysis (DTA), is the observation of primary and eutectic reaction temperature depression as a function of REE content. Both temperatures were lowered significantly by the initial addition of REE, with further increase in REE content decreasing them further. The changes amount to 2-7°C for the eutectic and 12-17°C for the primary reaction. These observations provide further support to the possibility that solute buildup is a significant component in the modification mechanism induced by REE. The second set of results to point out is the response of primary Si size to increases in both REE content and cooling rate. Figure 2.16 depicts these correlations. As can be seen from this diagram, increasing REE content is associated with decreasing particle size at any cooling condition. However, as cooling rate increases, the fraction of refinement that can be attributed to REE mechanism decreases, since the average particle size when no REE is present decreases with increasing cooling rate. While the presented results span a somewhat small range of cooling conditions, they raise the question of how further cooling rate increases could affect the modification mechanism.

2.7.2 Macroalloying

Given the limitations of each of the previously mentioned mechanisms, a fourth category of modification, based on a foundational understanding of the thermodynamic equilibrium of the alloying systems in use, is presented. Under this category, the uniting characteristic is a macroscopic shift in the equilibrium of the alloy, brought about by the addition of large additions of a third element, henceforth called X. The purpose of this change in equilibrium is to decrease the primary Si volume fraction and thus refine individual primary Si grains.

The most important consideration in the selection of X is the nature of its interaction with Al and Si. This notion can be summarized by the solubility of X in existing phases and the formation of intermetallic compounds. The solubility of X in Al and Si is relevant for two main reasons: strengthening of existing phases by solid solubility, and ensuring modification
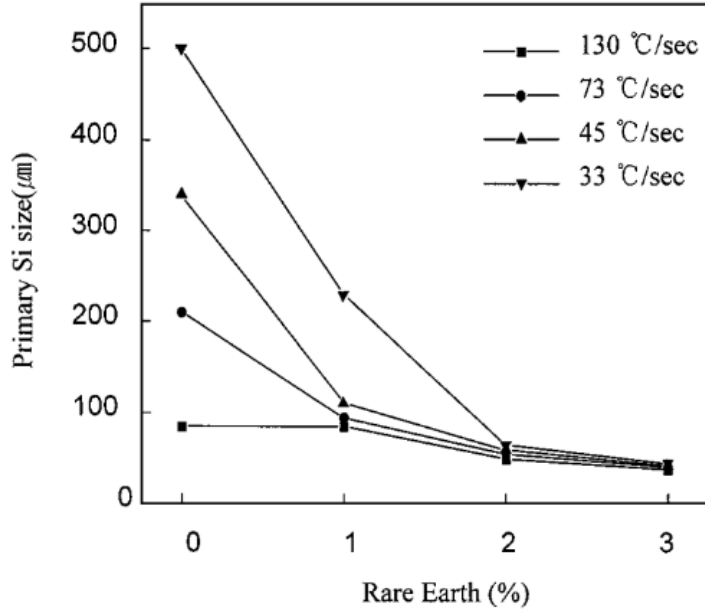
Figure 2.16: Combined effect of cooling rate and REE addition on primary Si refinement [38]

occurs by changes in equilibrium rather than solute buildup in the liquid. Few elements have any solubility in primary Si, rendering this parameter null. Solid solubility in α-Al is thus a deciding factor in the selection of potential alloying elements. Regarding the desired decrase in primary Si volume fraction, this change must be accompanied by an increase in α-Al or eutectic Si, or by the formation of a new phase. The latter of these options makes the formation of intermetallic compounds potentially beneficial for the intended use. Ideally, these intermetallics should use up some of the Si in the alloy. This is easiest to achieve by selecting systems with intermetallics that contain Si in their chemistry.

This section introduces Mg and Mn as potential elements for the modification of primary Si via macroalloying. These elements fit the solubility and intermetallic formation set forth above. Microstructural distribution and known intermetallic behaviour are also considered.

2.7.2.1 Solidification Path and Expected Microstrucutre

Figures 2.17 and 2.18 show the liquidus projections of the ternary phase diagrams for Al-Si-Mg and Al-Si-Mn, respectively. These diagrams were produced using ThermoCalc 2017a software and TTAL7 database (version 7.1) [45]. They provide a comprehensive view of the possible solidification reactions for each alloy system. Based on the composition of the baseline alloy used in this work, the use of these ternary systems will be simplified to alloy compositions containing 40wt%Si. This means that within the context of this section, any addition of Mg or Mn must be balanced by a decrease in Al content in the alloy. Figures 2.19 and 2.20 depict isopleths of each alloy system at a constant 40wt%Si. These diagrams can be used to identify the possible solidification paths and ultimate microstructural distribution of different compositions within each alloy system.
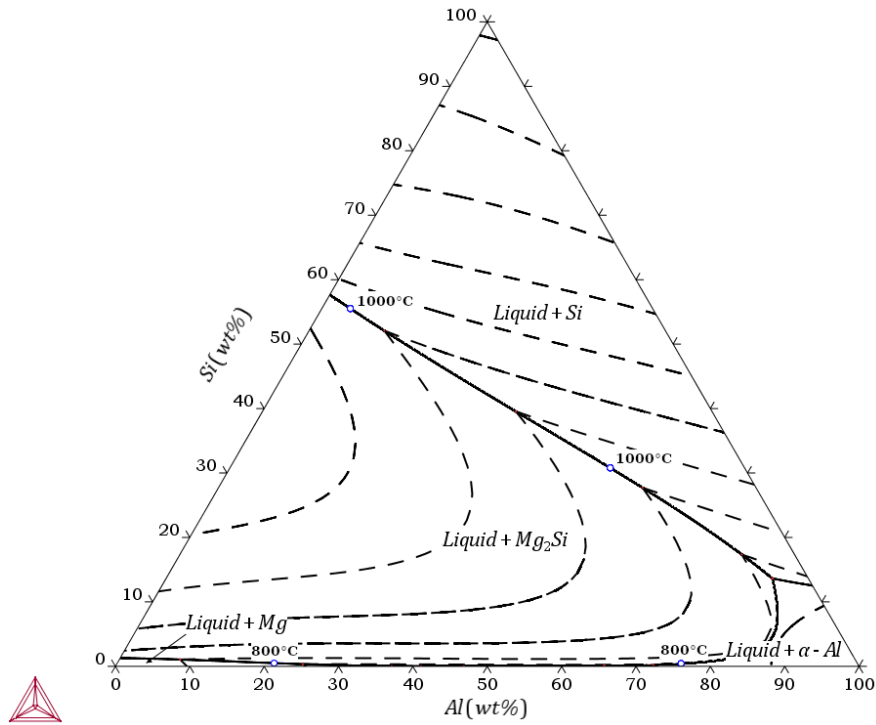
Figure 2.17: Al-Si-Mg liquidus projection
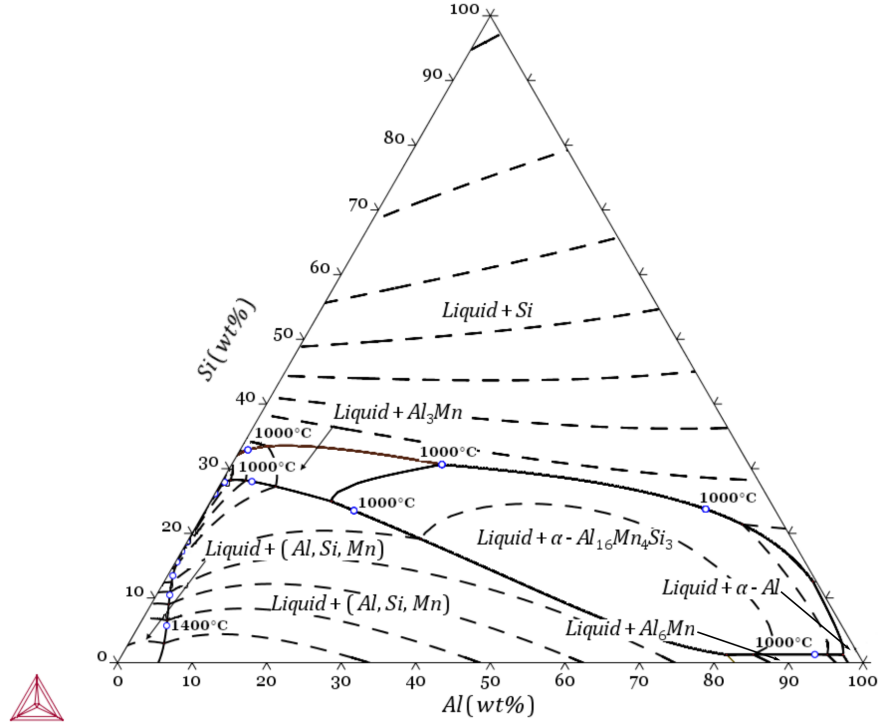
Figure 2.18: Al-Si-Mn liquidus projection

Figure 2.19 shows an Al-40Si-Mg pseudobinary. This diagram describes the changes in solidification path when Si is kept at 40wt% while Mg (and Al) content varies. The initial addition of Mg produces a liquid → liquid + primary Si → liquid + Si + Mg_2Si → ternary eutectic (α-Al + Si + Mg_2Si) solidification sequence. With increasing Mg content, the volume fraction of primary Si in the microstructure decreases while the volume fraction of ternary eutectic increases. At approximately 27wt% Mg, the solidification path changes to liquid → liquid + Si + Mg_2Si → α-Al + Si + Mg_2Si. When Mg content increases beyond this point, the solidification path changes once again to liquid → liquid + primary Mg_2Si → liquid + Si + Mg_2Si → α-Al + Si + Mg_2Si. Considering the goal of Mg alloying is to refine primary Si, only the first solidification path is viable for this purpose. This narrows down the range of Mg content for use in Al-40Si to under 27wt%.

As shown in the Al-40Si-Mn pseudobinary (Figure 2.20), Si remains the primary phase at all Mn levels. Depending on Mn content, the secondary reaction can produce α-$Al_{16}Mn_4Si_3$
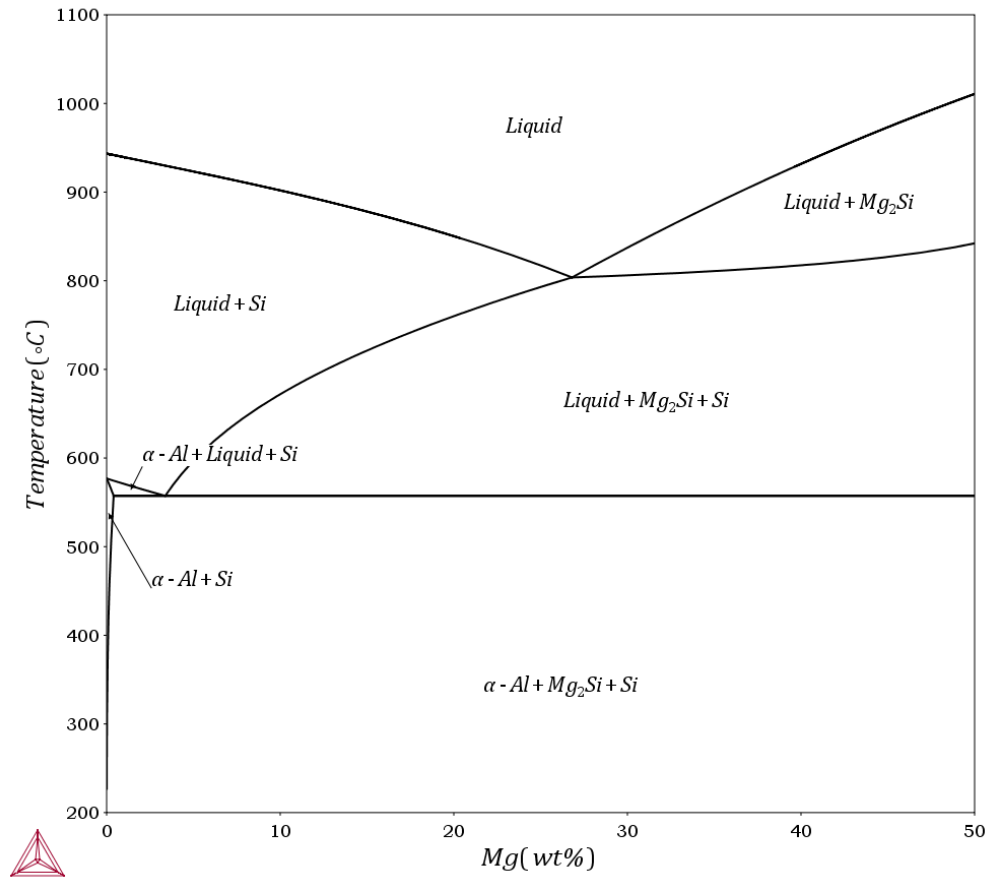
Figure 2.19: Al-40Si-Mg pseudobinary

+ Si or Al_3Mn + Si. A key composition to note in this system is 20wt%Mn. Higher Mn content produces a mix of Si, α-$Al_{16}Mn_4Si_3$, and Al_3Mn. Notably, no α-Al forms beyond this composition. The presence of α-Al in Al-Si alloys provides the alloy with ductility, and this behaviour is not known to be replicated by either α-$Al_{16}Mn_4Si_3$ or Al_3Mn. For this reason, the range of Mn content that best fits the purpose of alloying in this instance is 0-20wt%.

2.7.2.2 Intermetallic Properties

Intermetallic compounds are defined as phases made up of two or more metals that have a fixed composition. Intermetallics are commonly regarded as hard and brittle, but the properties of a specific compound are heavily dependent on its crystal structure [46]. This
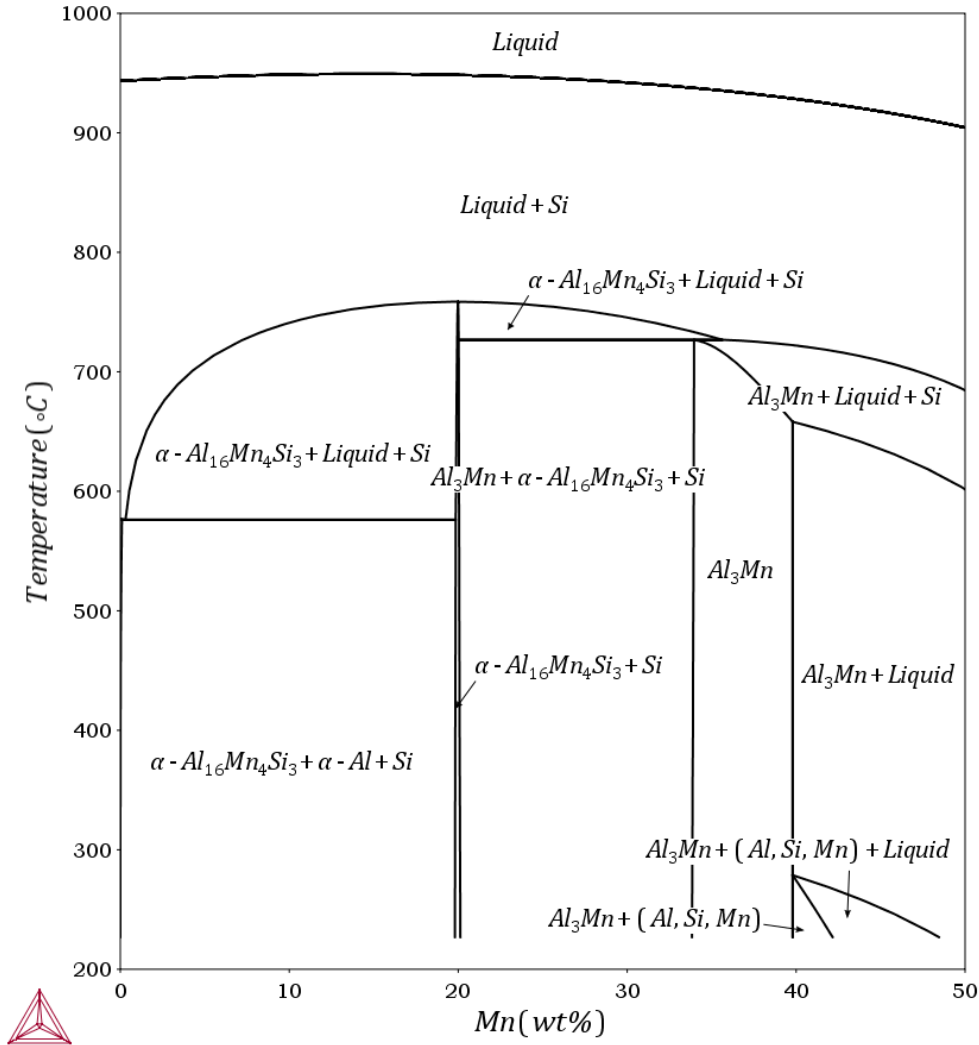
Figure 2.20: Al-Si-Mn pseudobinary

section discusses the intrinsic mechanical properties of Mg_2Si an α-MnAlSi and serves as a starting point for assessing the effect of intermetallics on the structural and mechanical properties of Al-40Si-X.

2.7.2.2.1 Mg_2Si

Mg_2Si solidifies in an FCC lattice of prototype CaF_2 [47]. The FCC crystal structure has 12 slip systems available for dislocation motion and is commonly ductile. Mg_2Si, however, is brittle at temperatures below 500K [48]. While the reason for this brittle behaviour has

not been experimentally determined, one account indicates this is possibly due to the strong tendency of Si to form covalent bonds [49]. Research focused on enhancing ductility and toughness of Mg_2Si through doping exists, with Al being one of the proposed dopants [49, 50]. One of these studies measured hardness as a function of Al addition, and tested each alloy under compression to determine their ductile-to-brittle transition temperature (DBTT) [49]. Hardness peaked at 4wt% Al, and the authors attribute the decrease in hardness at higher Al contents to the precipitation of α-Al. DBTT stabilizes at 420°C for Al >6wt%. These results are most applicable to the dissolution of Al atoms in the Mg_2Si crystal. However, the observed trends observed are promising when considering the composite-like behaviour expected of the intermetallic + α-Al structure, and the RS nature of the process for which the Mg_2Si-containing alloy is being considered.

2.7.2.2.2 α-MnAlSi

α-MnAlSi presents primitive cubic lattice of prototype $Mn_4Al_{14}(Al_{0.5}Si_{0.5})_4Si$ [51]. Since primitive cubic lattices are rather uncommon in metals, little information, either experimental or theoretical, exists on the properties associated with this structure. However, a basic understanding can be gained from identifying the slip systems present in this lattice structure and comparing the number of systems, as well as the planar packing factor of the planes present in these systems, to traditional understanding of slip deformation. Figure 2.21 presents the atomic layout of the closest-packed plane (<100>) present in a primitive cubic lattice. In this structure, the planes that bound the unit lattice have the highest packing factor, meaning there are six possible slip planes in the lattice. Each of these slip planes has two available slip directions. Thus, theoretically there exist twelve slip systems in a primitive cubic lattice. As dictated by traditional rules of slip deformation, a lattice with this number of slip systems should typically be ductile. The lack of experimental data to corroborate this requires cautious reliance on this understanding. More importantly, this preliminary assessment of slip systems should be coupled with existing information on the behaviour

of α-MnAlSi as pertains to ductility and toughness, especially when embedded in a ductile matrix. These notions will be discussed in Section 2.7.2.3.
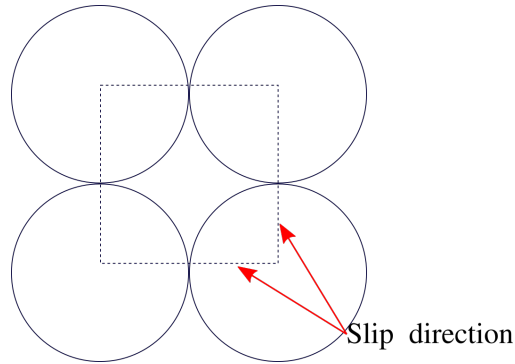
Figure 2.21: <100>plane in primitive cubic lattice

2.7.2.3 Intermetallic Morphology

The use of alloying elements that introduce intermetallic compounds poses the question of how these intermetallics will interact with the existing microstructure. In Al-40Si, the morphology of primary Si can significantly decrease the service life of a component due to premature crack initiation. Given the use of intermetallics to replace some of the primary Si formed in Al-40Si, the morphology of these compounds must be carefully considered. For this reason, this section delves into the morphology of Mg_2Si and α-MnAlSi, as well as their expected behaviour under RS processing.

2.7.2.3.1 Al-Si-Mg

Mg_2Si reportedly forms in one of two morphologies: blocky and Chinese-script [52, 53, 54, 55]. The presence of the blocky morphology can be correlated to the Al-Mg_2Si pseudobinary, which can be found in Figure 2.22. When an alloy falls on this plane, hypereutectic compositions (Mg>10 at%) tend to form blocky Mg_2Si followed by Chinese-script Mg_2Si [53, 54, 56]. The range of compositions encompassed by this pseudobinary are vastly different from the range suggested in Section 2.7.2.1, with the pseudobinary covering compositions that are richer in

Mg (and poorer in Si) than the suggested alloy. However, due in part to a combination of the low density of Mg, the simplicity of the pseudobinary as compared to a ternary, and existing trends in the field, most of the work done on Al-Si-Mg follows compositions dictated by the Al-Mg$_2$Si pseudobinary. This tendency leads to most Mg$_2$Si characterization efforts focusing on its blocky morphology. In contrast, reports on the Chinese-script morphology indicate regions far from the pseudobinary plane, such as that of the proposed range, form it exclusively [52, 57].
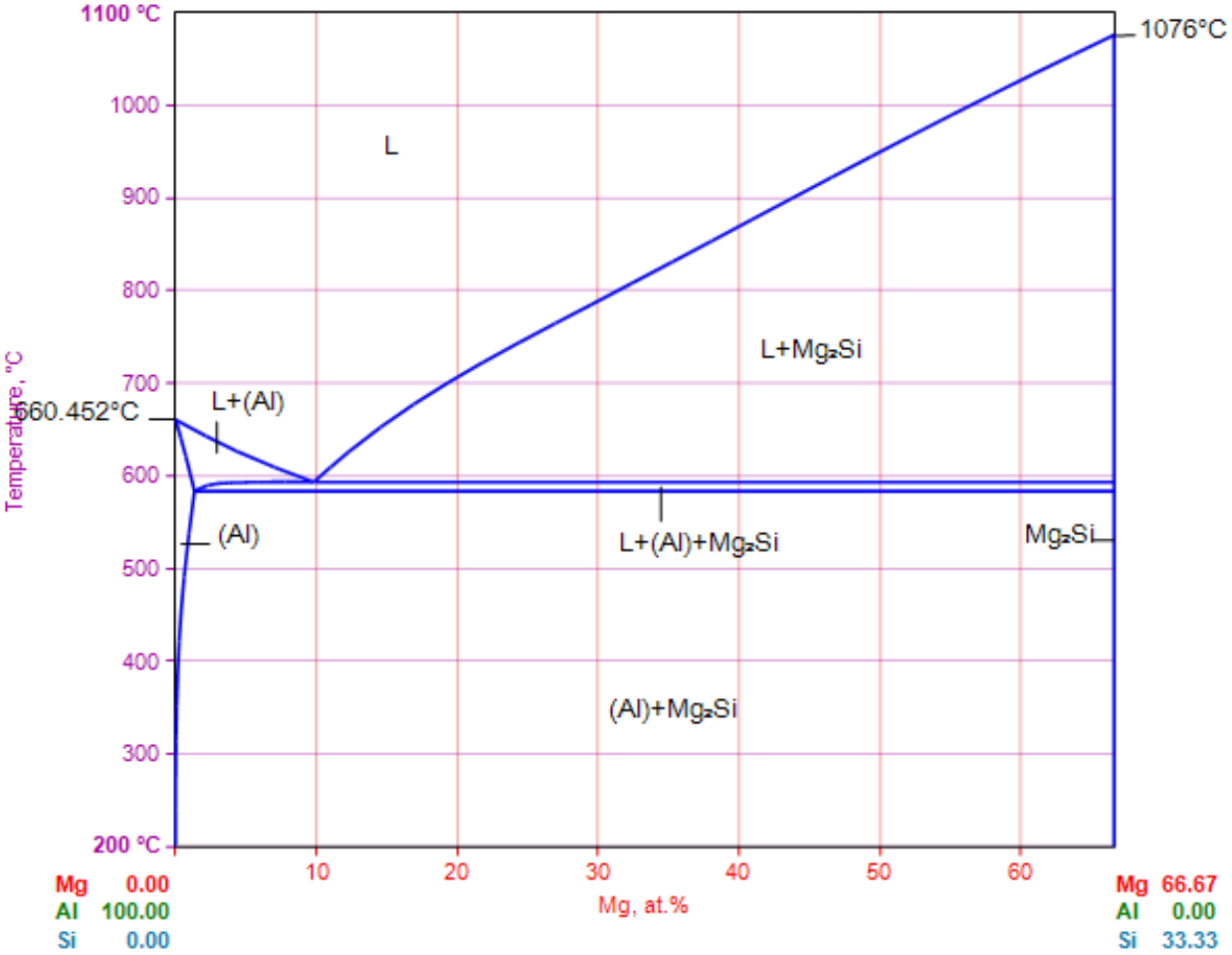
Figure 2.22: Al-Mg$_2$Si pseudobinary [58]

Refinement and modification of the Chinese-script morphology when increasing cooling rates have been reported in the literature [52, 59, 60]. These results are largely limited

to compositions on or near the Al-Mg$_2$Si pseudobinary, which may limit their applicability alloys containing large amounts of Si. However, these observations do support the feasibility of Mg$_2$Si modification by RS.

In contrast to the somewhat limited literature on Al-Si-Mg under RS, this alloy system continues to see substantial interest for use in casting. Within this context, the addition of a fourth element (to chemically modify the morphology of Mg$_2$Si) has been attempted in a few studies [52, 55, 61]. Due to their strong modifying ability and modification mechanism, Sr and Ca stand out among the proposed elements to modify the Chinese-script morphology of Mg$_2$Si. Both these elements are thought to modify Mg$_2$Si morphology by serving as nucleation points for Mg$_2$Si crystals. A well-accepted hypothesis regarding the use of Sr as a nucleation agent is based on the low misfit of the (100) planes in Al$_4$Sr and Mg$_2$Si [62]. For nucleation to be feasible, misfit between the two planes must be below 6% [63]. Misfit between (100)Al$_4$Sr and (100)Mg$_2$Si is estimated at 0.69% [62], making Al$_4$Sr a rather desirable location for nucleation. Modification of Mg$_2$Si morphology by Ca addition is thought to work similarly to Sr. Evidence of this has been shown through TEM imagining of Ca-rich particles present within modified Mg$_2$Si particles. These particles were identified as CaSi$_2$, and orientation relationships deduced to be [111]Mg$_2$Si//[001]CaSi$_2$ and ($\bar{1}$01)Mg$_2$Si//(110)CaSi$_2$ [55].

2.7.2.3.2   Al-Si-Mn

Much of the research dealing with the morphology of α-MnAlSi does so to use this intermetallic as an alternative to acicular β-Al$_5$FeSi in Fe-containing Al-Si alloys [64, 65]. This arises from the ability of the α-MnAlSi lattice to accept Fe and Mn atoms interchangeably. Within the context of β-AlFeSi modification, a Mn/Fe ratio of 0.5 is accepted as the minimum value to control β-AlFeSi particle size [66]. This measure allows for alloy ductility to be dictated by the main alloying components, rather than by the stress concentration caused around sharp β-AlFeSi particles. At the same time, observations of morphological transition as a function of varying Mn/Fe ratio indicate that the best performing morphology of the

α-Al(Fe,Mn)Si intermetallic contains a Mn/Fe ratio below 1 [64, 66, 67].

Gao et al tested the effect of varying Mn content (0 to 3wt%) on the morphology and properties of cast Al-6Si-2Fe-xMn [64]. They identified intermetallic morphology transitions to follow an acicular $\rightarrow$ Chinese script $\rightarrow$ flower-like $\rightarrow$ dendritic sequence (Figure 2.23). Of these morphologies, flower-like α-Al(Fe,Mn)Si, found in the alloy containing 1.5% Mn (Mn/Fe = 0.75), was associated with the best ductility and tensile strength. Conversely, the alloy containing mostly dendritic α-Al(Fe,Mn)Si (Mn/Fe=1.5) performed the worst on the same metrics.

(a) Acicular intermetallic (no Mn) (b) Chinese-script intermetallic (1wt%)

(c) Flower-like intermetallic (1.5wt% Mn) (d) Dendritic intermetallic (3wt% Mn)
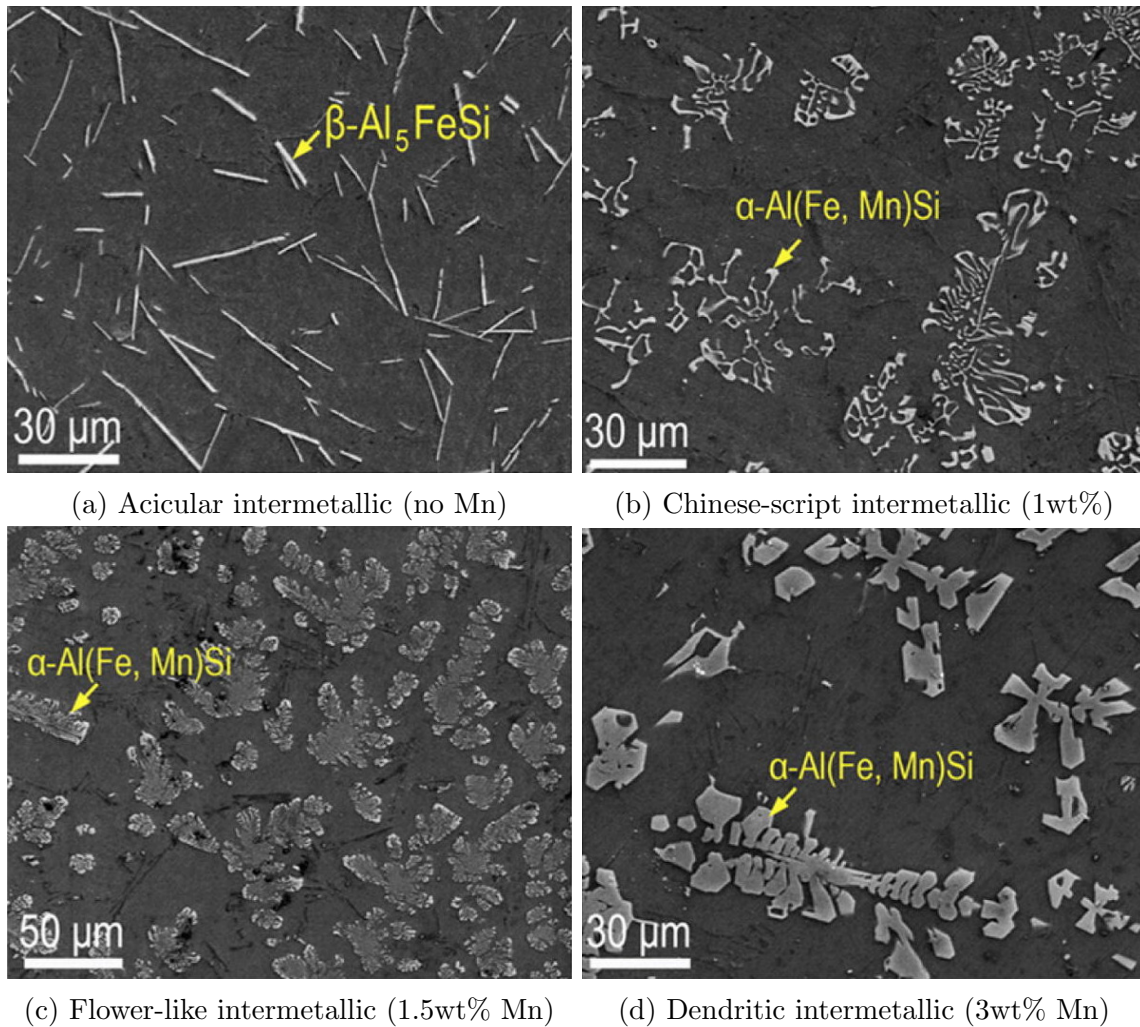
Figure 2.23: Intermetallic morphology of Al-6Si-2Fe-xMn [64]

Another important aspect in this discussion is the reported depression in primary and

eutectic Si nucleation temperature observed in Mn+Fe-modified alloys. Li et al studied the effect that using an Al-20Si-2.5Fe-2Mn master alloy to modify cast Al-20Si had on reaction temperatures [65]. Using Differential Scanning Calorimetry (DSC) observations, they identified a 5°C decrease in both primary and eutectic nucleation temperature when comparing the base alloy and one modified using 6% master alloy. The authors attribute this change to buildup of Mn and Fe atoms in the liquid, as observed in Electron-Probe Micro Analyzer (EPMA) results. This decrease in nucleation onset allows improved nucleation efficiency of primary and eutectic Si, as a higher driving force for growth exists upon nucleation due to increased undercooling. The microstructure of each alloy (Figure 2.24) show that the use of the master alloy caused a marked change in the size and morphology of primary Si. In the unmodified alloy, primary Si is large and irregular. In the modified alloy, primary Si is much smaller, better distributed, and there is a larger proportion of polygonal grains. These results thus provide further support to the use of Mn and Fe as new alloying elements for Al-Si, with their use introducing the possibility of multiple modification mechanisms targeting primary Si in order to decrease its particle size and homogenize its distribution throughout the alloy.

(a) Unmodified microstructure (b) Modified microstructure
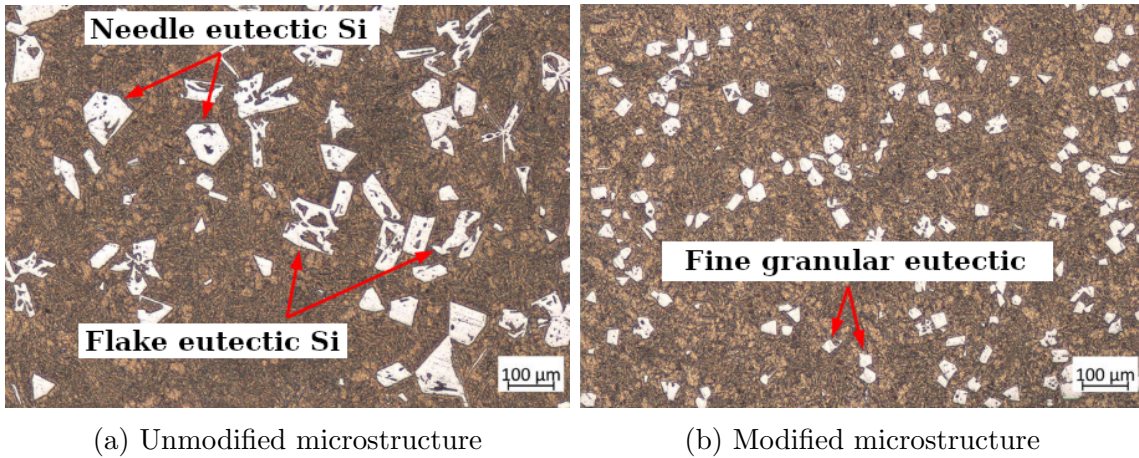
Figure 2.24: Effect of Al-20Si-2.5Fe-2Mn master alloy on microstructure of cast Al-20Si [65]

The Al-Si-Mn-Fe system has not been substantially studied under RS conditions. However, results that compare the effect of varying cooling rate on morphology and intermetallic particle size have been reported. Zhang et al reported on the effect of cooling rate on mi-

crostructure of cast A356 with excess Fe and Mn [67]. This work stands out within the present context due to its blending of two ideas relevant to the introduction of Mn and Fe to a rapidly solidified Al-Si alloy through the study microstructure resulting from varying cooling rates and Fe and Mn content. Two trends arise from these results (Figure 2.25). The first is the coarsening of α-Al(Fe,Mn)Si particles with increasing Fe and Mn content. The second entails the refinement of all microstructural features as cooling rate increases (up to 17.3 K/s).
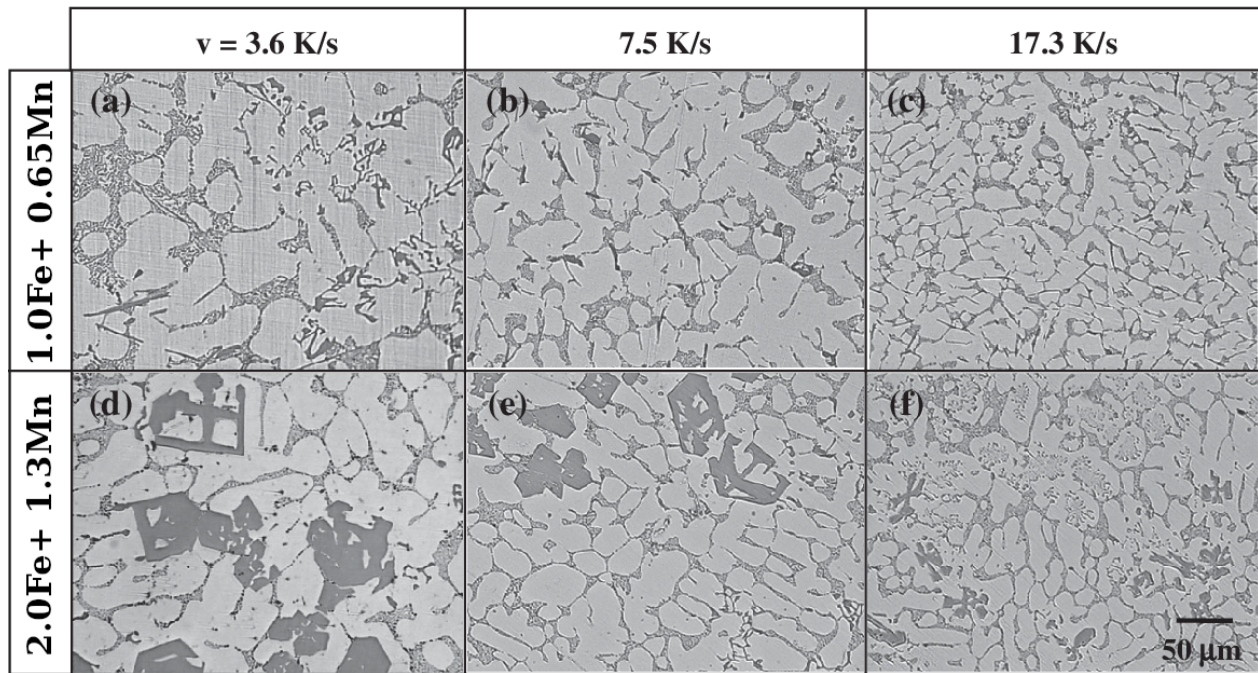
Figure 2.25: Effect of Fe, Mn content and cooling rate on microstrcutre of A356 [67]

2.8 Summary

This chapter discussed various notions relevant to the RS of Al-40Si and the selection of alloying elements useful in modifying the morphology of primary and eutectic Si that form in this alloy. These include:

- in-situ composite behaviour attributed to the interaction between Si and α-Al,

- growth mechanism of Si,

- common morphologies observed in primary and eutectic Si,

- halo formation in hypereutectic Al-Si alloys and the reported mechanism by which it occurs,

- Laser Powder-Bed Fusion as a Rapid Solidification process,

- limitations associated with using typical primary Si modifiers (P, Na, Sr) under RS conditions, and

- potential benefits of using macroalloying and rare-earth solute build-up as mechanisms for primary Si modification.

The hypereutectic Al-Si background presented in this chapter provides a basis to which the microstructures in this work can be compared to assess the effects of RS and alloying. This is particularly true for the Si morpholgies and the mechanism of halo formation reported in the literature. Understanding how the interaction between Si and α-Al affects the alloy's properties allows to examine microstructural variation across different degrees of RS and identify the benefits and detriments of varying cooling rate. Finally, the thorough review of potential alloying elements and their merits for use in RS outlines factors used in selecting alloy systems to be tested. This assesment led to the selection of three alloying systems (Al-Si-Ce, Al-Si-Mg, and Al-Si-Fe-Mn) to study in addition to the original Al-40Si alloy being used.

Chapter 3

Experimental

This chapter discusses sample generation and analysis methods relevant to four alloying systems: Al-40Si, Al-40Si-1.5Ce, Al-40Si-9.2Mg, and Al-40Si-2.75Fe-2.75Mn-1.5Sc (on a wt% basis). Section 3.1 details the process used in selecting these compositions. Experimental techniques used for powder production, metallographic preparation, and microstructural analysis of all alloys are described in detail.

3.1 Composition selection

This section outlines the selection criteria used to determine the composition of Al-Si-Fe-Mn-Sc, Al-Si-Mg, and Al-Si-Ce used for Impulse Atomization.

3.1.1 Macroalloying Mechanism: Al-Si-Mn-Fe and Al-Si-Mg

Figures 3.1 and 3.2 present the predicted phase distribution in Al-40Si-Mn and Al-40Si-Mg as a function of Mn or Mg content. These plots were produced using data obtained from Gulliver-Scheil (G-S) solidification paths for various Al-40Si-Mg and Al-40Si-Mn alloy compositions, which were determined by Thermo-Calc software using the TTAL7 database (version 7.1).
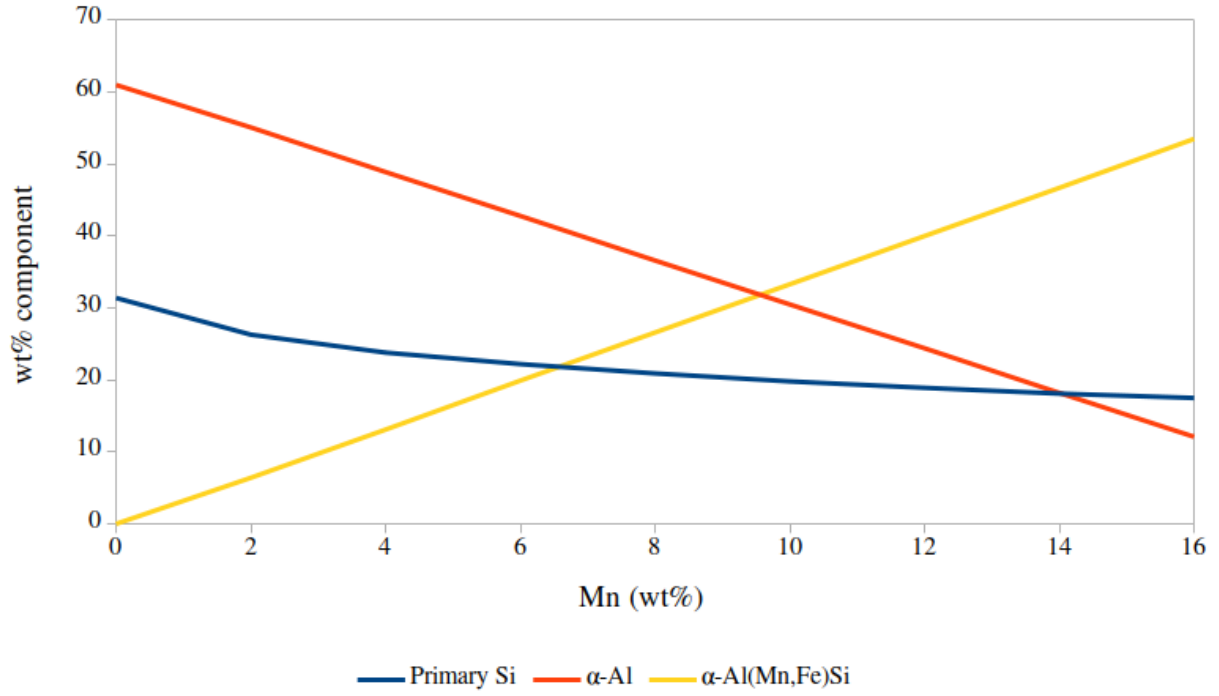
Figure 3.1: Predicted microstructure distribution in Al-Si-Mn system
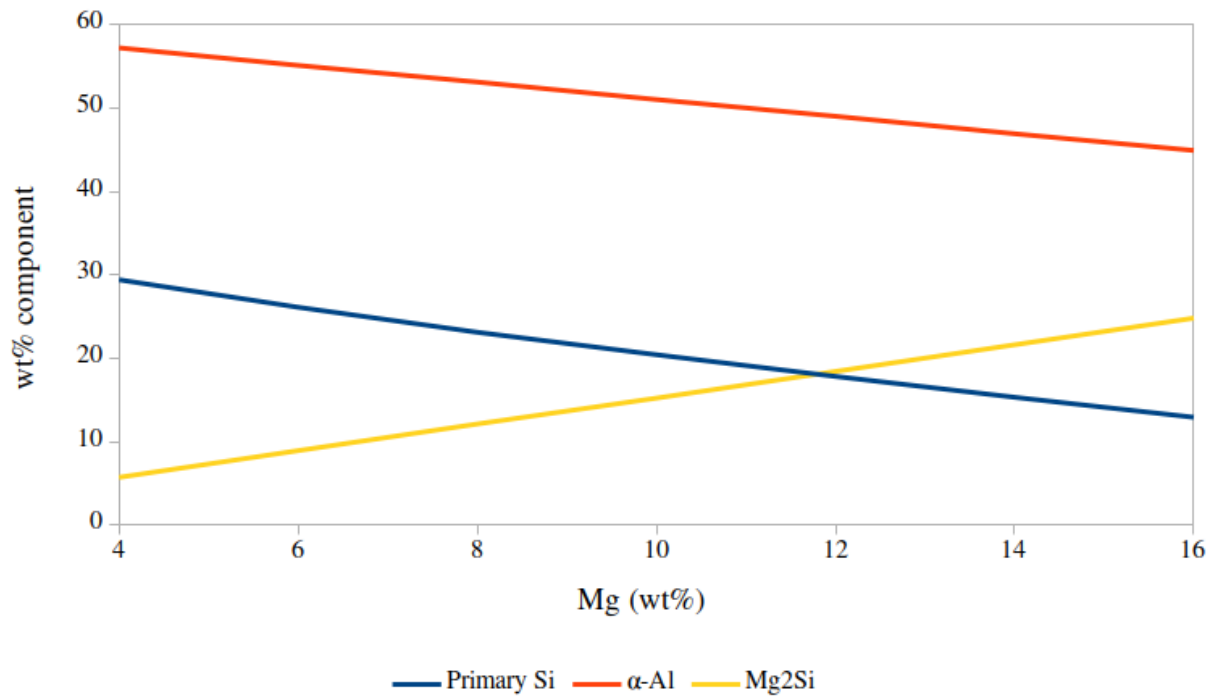
Figure 3.2: Predicted microstructure distribution in Al-Si-Mg system

In considering the primary Si phase fraction response to Mn wt% in Al-40Si-Mn (Figure 3.1), a clear cut-off can be found at the intercept where α-Al$_{16}$Mn$_4$Si$_3$ becomes the most prominent phase in the alloy. This selection is based on the goal of maintaining some ductility within the alloy as to not greatly compromise toughness. For this reason, α-Al should remain a major phase in the microstructure (Mn <9.5 wt%). Within this reduced range, a comparison between primary Si and α-Al$_{16}$Mn$_4$Si$_3$ stands as a secondary criterion for selecting a composition. As both phases are relatively brittle, having one be more prevalent than the other is not a concern. Thus, this decision was made by referring to the stated goal of producing this alloy: to reduce the volume fraction of primary Si. As the correlation between primary Si and Mn content is not linear, the Mn wt% at which the decrease in primary Si phase fraction slows down is a good compromise. Based on this rationale, 5.5wt% Mn was selected as a likely composition for this alloy.

The composition of Fe in Al-40Si-Mn-Fe was selected to balance out the Fe/Mn ratio, which is intended to optimize morphology of α-Al$_{16}$Mn$_4$Si$_3$. To avoid production of other intermetallics, the increase in Fe content will be accompanied with an equivalent decrease in Mn content from the 5.5 wt% selected previously. Phase fractions estimated previously should not be affected by this change, as Fe at this composition is mostly used up to form α-Al$_{16}$Mn$_4$Si$_3$ (now α-Al$_{16}$(Mn,Fe)$_4$Si$_3$). Based on reported trends that identify peak alloy properties when Mn/Fe ratio is between 0.5 and 1.5 [64], a Mn/Fe ratio of 1 was used. This ratio thus yields a composition of Al-40Si-2.75Fe-2.75Mn. The microstructure of Al-40Si-2.75Fe-2.75Mn is expected to contain 22 wt% primary Si. To further decrease the primary Si vol% in this alloy, a 1.5 wt% Sc addition was selected. Use of Sc has been shown to refine eutectic Si grains [68]. By using 1.5 wt% Sc in Al-40Si-2.75Fe-2.75Mn, primary Si is reduced to 5.1 wt% according to the Gulliver-Scheil (G-S) solidification model.

In Al-Si-Mg (Figure 3.2), phase fraction of all three phases varies linearly with Mg wt%. In contrast to Al-40Si-Mn, this alloy system does not present characteristics that make selection of a specific Mg wt% evident. Use of 9.2 wt% Mg is expected to produce a microstructure

containing 22 wt% primary Si. This respresents a 30% decrease in primary Si content from that in Al-40Si according to G-S.

3.1.2   Solute build-up mechanism: Al-Si-Ce

Unlike the Mn-Fe and Mg containing alloys, Al-Si-Ce is not intended to reduce the equilibrium amount of primary Si. Instead, the purpose of studying this alloy is to assess the feasibility of using solute buildup as a modification mechanism during RS. This goal, combined with the previously mentioned observations of REE content larger than 3% decreased modifying efficiency [41, 42, 43], narrows down the range of possible compositions.

Figure 3.3 presents a binary projection of the Al-Si-Ce system at a set 40% Si content and variable Ce ranging from 0 to 10%. This diagram was produced using the TCAL7 (version 7.1) database in Thermo-Calc 2021a. This diagram indicates some differences in the number of multi-phase solidification steps as Ce content increases from 0 to 0.5 wt%. Aside from this, increasing Ce content does not significantly affect the solidification path of the alloy. Given the lack of additional selection criteria, 1.5 wt% Ce was selected for use in Al-40Si-Ce. This composition is expected to produce 13.2 wt% primary Si according to G-S. This represents a 58% decrease in the amount of primary Si in the microstructure with respect to Al-40Si.

3.2   Powder Generation

Impulse Atomization (IA) was used in the generation of powders of each alloy described in this document. IA is a single fluid atomization technique that allows for limited convection within the solidifying droplets and fast heat extraction from the same [69]. IA is also a containerless process, which permits relatively high nucleation undercoolings. The atomizing tower is kept under a He-rich environment (<20 ppm O_2) aimed at limiting oxidation of the material and allowing fast heat extraction from the same. The nozzle plate used during this process contains 100 orifices, each of 100 μm diameter. During atomization, mechanical
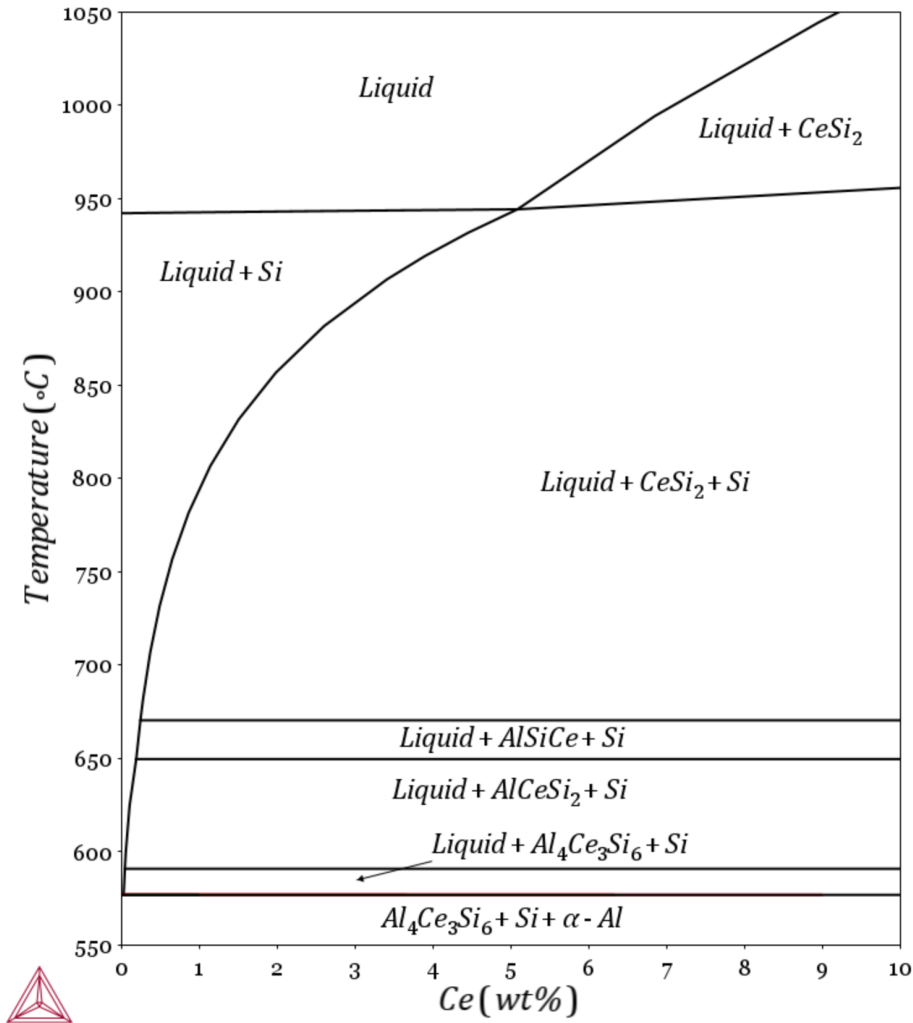
Figure 3.3: Al-40Si-Ce pseudobinary

impulses are applied to a melt and lead to the break up of the streams of molten metal that emanate from orifices in a nozzle plate. Figures 3.4 and 3.5 show schematics of the crucible and atomization tower used in IA. Details of the operating process are presented elsewhere [69].

Prior to atomization, melting of source materials and homogenization of the same was carried out in an induction furnace under inert gas. During this process, the source materials (Table 3.1) were held in a graphite crucible. Table 3.2 summarizes homogenization conditions for each alloy. Liquidus temperatures included in Tables 3.1 were obtained from the binary
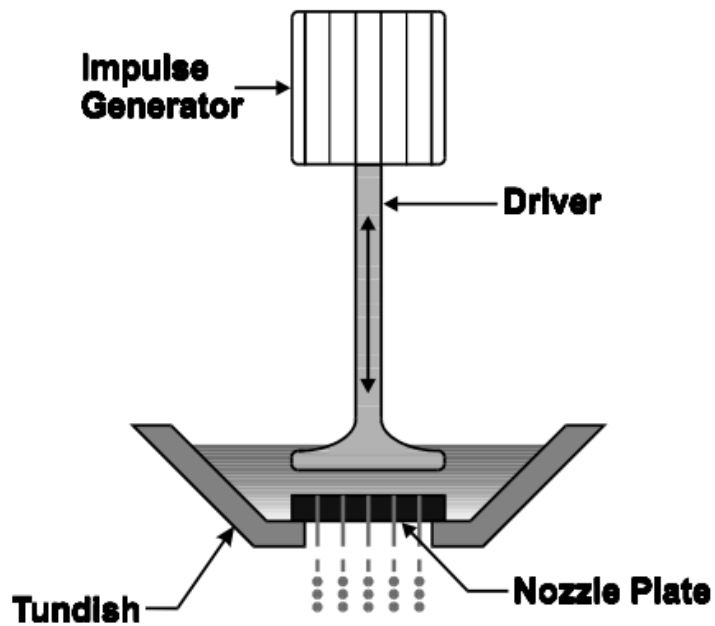
Figure 3.4: Schematic of Impulse Atomization setup [69]

1. Pulsator; 1a. Impulse Applicator
2. Furnace
3. Crucible
4. Metal droplets
5. Frame to hold and adjust the unit
6. Atomizing chamber
7. Powder collector
8. Gas and vacuum inlets and outlets
9. Video camera
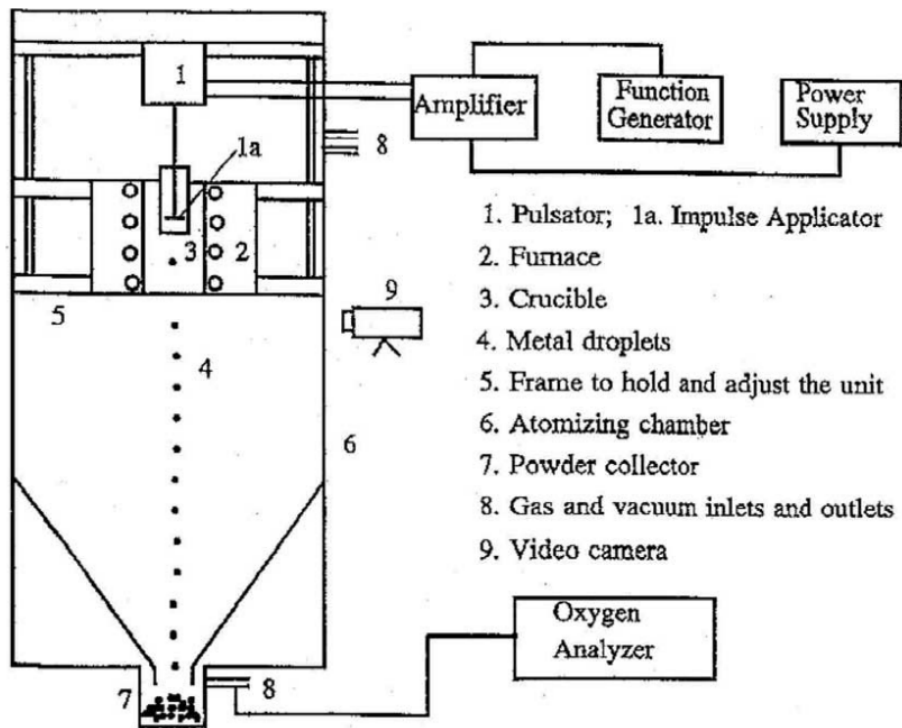
Figure 3.5: Atomization tower setup [69]

phase diagrams for Al-Si, Al-Ce, Al-Mg, Al-Mn, and Al-Fe [70]. The liquidus temperatures listed in Table 3.2 were obtained from the Gulliver-Scheil solidification paths produced in Thermo-Calc software for each alloy composition listed in this table. Thermo-Calc 2017a and databases TTAL7 (version 7.1) and SSOL4 (version 4.9g) were used for this purpose [45].

Table 3.1: Source Materials used in Alloy Production

Alloy (wt%)	Source Materials	Purity (wt%)	Liquidus Temperature (°C)
Al-40Si	Al	99.99	660.5
	Si	99.99	1414
Al-40Si-1.5Ce	Al-50Si master alloy	99.99	1040
	Al-20Ce master alloy	99.9	687
	Al	99.99	660.5
Al-40Si-9.2Mg	Al-50Si master alloy	99.99	1040
	Mg	99.99	650
	Al	99.99	660.5
Al-40Si-2.75Fe-2.75Mn-1.5Sc	Al-50Si master alloy	99.99	1040
	Mn	99.8	1245
	Fe	99	1538
	Al	99.99	660.5

Table 3.2: Melting and melt parameters used in alloy preparation

Alloy (wt%)	Liquidus T (°C)	Atomization T (°C)	Holding time (min)
Al-40Si	941	1125	30
Al-40Si-1.5Ce	953	1200	30
Al-40Si-9.2Mg	906	1050	60
Al-40Si-2.75Fe-2.75Mn-1.5Sc	950	1400	30

3.3   Cleaning and Sieving

After atomization, the powders atomized underwent a cleaning step involving draining of oil, as well as cleaning the powders with each toluene and subsequently with ethanol. Toluene was used to remove oil left on the surface of the powders, and ethanol served to remove any

toluene remaining from the previous mixing step. Both mixing steps involved multiple cycles (4-7) of contact and mixing (2-3 minutes) with the respective solvent followed by draining of the same. After draining ethanol in the final step, the clean powders were allowed to dry overnight.

Following the cleaning process, the powders were sieved to separate them into various size ranges. Powders within a size range share similar thermal history and thus powder size can be used to refer to the relative cooling rate experienced during solidification by multiple samples. Sieving was performed using a RO-TAP Sieve Shaker and sieves of sizes 63-1000 μm (mesh sizes: 230-18 [71]) for 10 minutes. At the end of this step, each sieve contained a single layer of powders, suggesting the sieves were not overly full and all powders could contact the sieve in which they were contained. This supports the sieving process as an appropriate approach to separate the powders into their respective size ranges.

3.4   Liquid Cooling Rate Model

A variation of the cooling rate model developed by Wiskel, Henein, and Maire [72, 73] was used to estimate the liquid cooling rates experienced by the droplets of different sizes. Liquid cooling rates determined can thus be used to describe the thermal history of each range of powder sizes. This approach uses a modified version of the Whitaker equation (shown in Equation 3.1) to estimate the effective heat transfer coefficient (h_{eff}) between a droplet and the surrounding gas.

$$Nu = \frac{h_{eff} \cdot d}{k_s} = 2\frac{B}{k_s(m+1)}\frac{(T_s^{m+1} - T_\infty^{m+1})}{(T_s - T_\infty)} + (0.4Re^{1/2} + 0.06Re^{2/3})(Pr)^{1/4}(\frac{\mu_\infty}{\mu_s})^{1/4} \quad (3.1)$$

In Equation 3.1, Nu is the Nusselt number, d is droplet diameter, and k_s is the thermal conductivity of the gas at the droplet's surface temperature. T_s and T_∞ are, respectively, the droplet's surface temperature and the free stream gas temperature. Re is Reynolds number,

Pr is the Prandlt number, and μ_∞ and μ_s are viscosity of the gas at the free stream gas temperature and droplet's surface temperature, respectively. B and m in this equation refer to the pre-exponential and exponent terms of the gas' thermal conductivity equation as a function of temperature.

An initial droplet velocity (v) of 0.5 m/s is assumed [74], and acceleration $(\frac{dv}{dt})$ is calculated using Equation 3.2, where ρ_m is droplet density, ρ_g is gas density, g is acceleration due to gravity (9.81 m^2/s), and C_d is drag coefficient. C_d is calculated using Equation 3.3.

$$\frac{dv}{dt} = \frac{\rho_m - \rho_g}{\rho_m}g - 0.75\frac{\rho_g}{\rho_m}(\frac{C_d}{d})v^2 \tag{3.2}$$

$$C_d = \frac{18.5}{Re^{0.6}} \tag{3.3}$$

Equation 3.4 describes heat transfer between the droplet and surrounding gas, where $\frac{dT_m}{dt}$ is cooling rate and c_{pm} is droplet specific heat. This equation is solver using the Fourth Order Runge-Kutta method, and Equation 3.2 is solved using simple Euler. Given the use of the alloy's physical properties in these equations, calculated liquid cooling rate varies slightly when comparing the same powder size across different alloys.

$$\frac{dT_m}{dt} = -\frac{6h_{eff}}{\rho_m \cdot c_{pm} \cdot d}(T_s - T_\infty) \tag{3.4}$$

3.5 Differential Scanning Calorimetry

Differential Scanning Calorimetry (DSC) was performed on as-atomized Al-40Si powders using a LABSYS evo DSC apparatus. This technique makes use of the differences in enthalpy released by the sample of interest and a reference sample to identify reactions occuring during heating and cooling.

Each sample underwent five heating and cooling cycles. These correspond to two 20 K/s cycles followed by one of each 10, 5, and 1 K/s cycles. The first heating cycle was used

to identify potential precipitation reactions arising from the supersaturation of the phases present in the as-atomized samples. Each of the subsequent cycles provided a data point to be used in determining the equilibrium liquidus and solidus temperatures of the samples. This is achieved by obtaining a trendline that describes the correlation between reaction temperature and cooling rate measured for these samples, and extrapolating it to 0 K/s. Appendix B provides more detail on this approach. The estimated temperatures can then be compared to the equilibrium temperatures provided by the alloy's phase diagram.

3.6 Metallographic Preparation

The powders were mounted in epoxy cylinders using a cold-mounting system (West System, 105 Epoxy Resin and 205 Fast Hardener). This process involves the use of liquid epoxy and hardener in a 5:1 ratio. A Ni filler (Buehler 20-8500) was added to produce conductive mounts for use in Scanning Electron Microscopy. The powders were deposited at the bottom of sample holders of 31.75 mm (1.25 inch) diameter, and the mixture of epoxy, hardener and Ni filler was used to fill the sample holder. The samples were then allowed to harden overnight.

Once hardened, the samples were ground and polished to reveal the cross-sections of individual droplets. This was done using a Buehler AutoMet 250 Grinder-Polisher. Grinding steps include the use of 400, 600, 800, and 1200 grit sandpaper. Polishing steps include the use of 9, 6, 3, and 1 μm diamond suspension, as well as 0.05 μm colloidal silica polishing suspension. After polishing, each sample was etched for 20 seconds at 20 °C using Kellers reagent (2.59 wt% HNO_3, 0.64% HCl, 0.55% HF, and H_2O balance).

3.7 Characterization

Optical Microscopy (OM) was performed using an Olympus BX61 Motorized Optical Microscope equipped with an Olympus DP73 digital camera. OM was used for a first look at

the microstructure of each alloy and images obtained by this means were used to quantify microstructural distribution. Scanning Electron Microscopy (SEM) was carried out using a Tescan Vega3 SEM with EDX instrument. SEM images were mainly used for analysis of the eutectic structure present in each of the alloys.

Phase identification was achieved through X-Ray Diffraction (XRD) and aided by Electon Dispersive X-Ray Spectroscopy (EDX). XRD was performed using a Rigaku Ultima IV instrument equipped with a Cobalt anode. Phase identification based on the patterns produced by XRD was performed using DIFFRAC.EVA software and the ICDD PDF4+ and PDF4+/Organics databases. EDX was carried out using a Tescan Vega3 SEM with EDX instrument.

3.8   Microstructure Quantification

Microstructure distribution was experimentally determined by the Systematic Manual Point Count method outlined in the ASTM 562-19 standard [75]. For each powder size, OM images of ten individual droplets were used. A grid was overlayed on each image using ImageJ software, with the intercepts of vertical and horizontal lines serving as the points to be counted (Figure 3.6). For each image, 250-350 points were counted.

Table 3.3 provides a break-down of the magnifications selected for images of each powder size. For powder sizes up to 355-425 μm, images were taken at the highest magnification for which the whole droplet was visible. For larger powder sizes, the magnifications used do not allow the full droplet to be in view, but instead provide a more detailed view of a section within the droplet.

3.9   Eutectic Spacing Measurements

Eutectic spacing in various powder sizes of Al-40Si was used to estimate the average solidification growth velocity, undercooling, thermal gradient, and cooling rate of the eutectic.
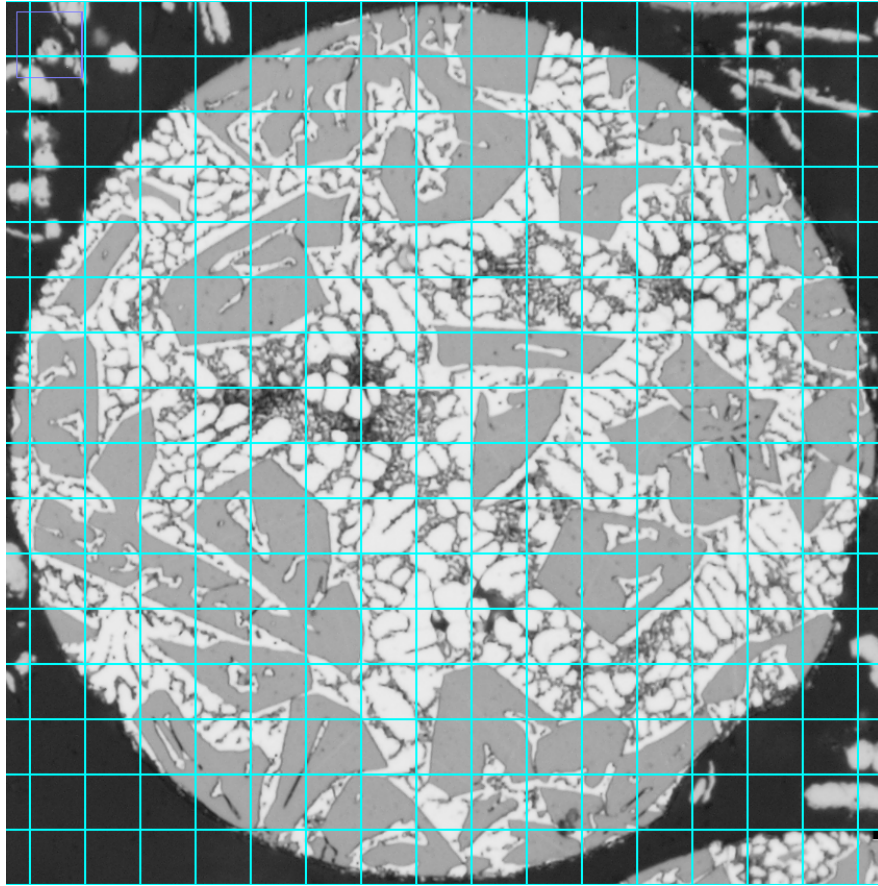
Figure 3.6: Example of image processed for Systematic Manual Point Count method. Al-40Si-1.5Ce, 90-106 μm droplet.

Measurements were obtained by using the Heyn Linear Intercept procedure (outlined in the ASTM E112-13 standard [76]) on SEM images. Figure 3.7 shows an example of how this methodology was applied to the samples used for this work. As shown in this Figure, care was taken to have individual start and end at the intersection between a Si grain and the surrounding matrix. For each powder size, eutectic spacing was measured for 5 droplets at 10-15 locations per droplet.

Eutectic growth velocity and undercooling were estimated using Gunduz' modification of the Jackson-Hunt eutectic growth theory [77]. Both treatments consider the effects of diffusion and surface tension on growth of eutectics. The Jackson-Hunt model [78] simplifies diffusion at the solid/liquid interface by assuming a planar interface and similar undercooling

Table 3.3: Magnification used for Systemic Manual Point Count method

Alloy	Powder Size (μm)	Magnification
Al-Si	90-106	100X
	125-150	100X
	355-425	50X
	500-600	50X
	710-850	50X
Al-Si-Ce	63-75	100X
	90-106	100X
	180-212	50X
	300-355	50X
	850-1000	20X
Al-Si-Mg	106-125	100X
	180-212	50X
	300-355	50X
	500-600	20X
	710-850	50X
Al-Si-Fe-Mn-Sc	106-125	100X
	180-212	100X
	300-355	50X
	500-600	20X
	710-850	50X

for both phases forming under eutectic growth. These assumptions work well for growth of regular eutectics, but they fail in systems with irregular eutectic growth, such as Al-Si. In contrast, Gunduz' approach was developed to be used on Al-Si and as such considers the interfacial non-equilibrium effects present in this system.

According to the Jackson-Hunt model, eutectic spacing, λ, growth velocity, V, and undercooling, ΔT are correlated using Equation 3.5. K_1 and K_2 in Equation 3.5 arise from properties of each of the phases in the eutectic, and can be calculated using Equations 3.6 and 3.7, respectively. Tables 3.4 and 3.5 define the parameters used in these equations and provide their values for the Al-Si eutectic.

$$\Delta T(\lambda, V) = K_1 \lambda V + \frac{K_2}{\lambda} \qquad (3.5)$$
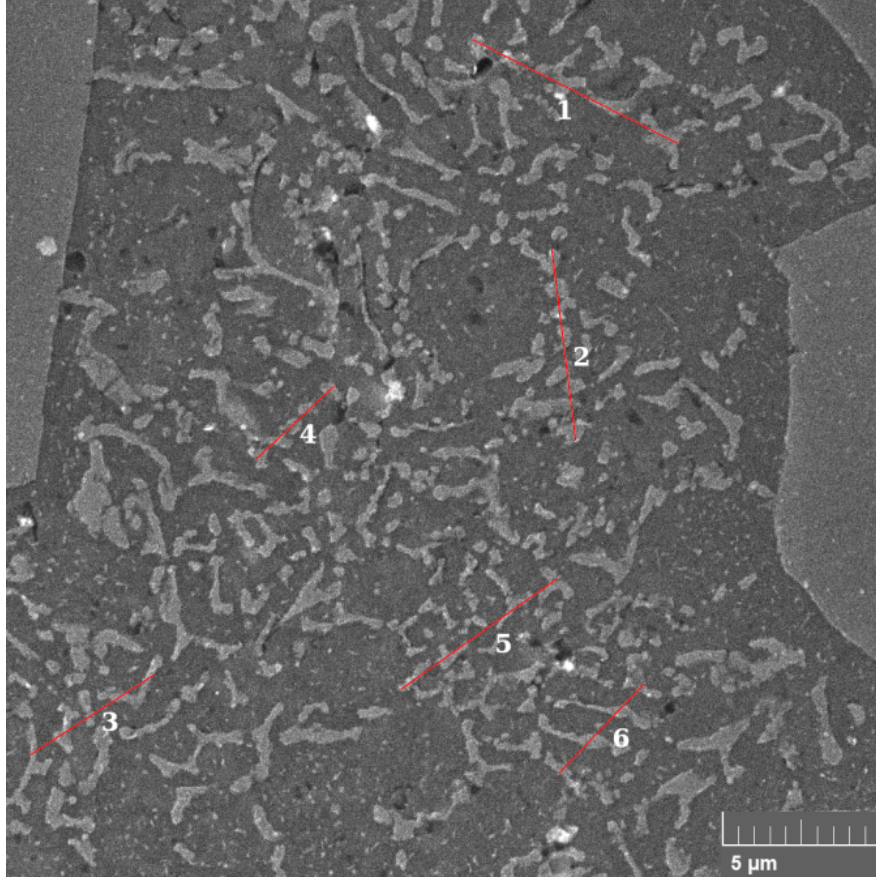
Figure 3.7: Example of image processed for Heyn Linear intercept method. Al-40Si, 355-425 μm droplet.

$$K_1 = \frac{\overline{m}C_0^*}{D}\frac{P}{f_\alpha f_\beta} \tag{3.6}$$

$$K_2 = 2\overline{m}\left(\frac{\Gamma_\alpha sin\theta_\alpha}{|m_\alpha|f_\alpha} + \frac{\Gamma_\beta sin\theta_\beta}{|m_\beta|f_\beta}\right) \tag{3.7}$$

The Al-Si eutectic consists of elongated Si grains embedded in an α-Al matrix [6]. During growth, the Si phase forms at significantly higher undercoolings than the α phase, leading to the formation of a non-planar solid/liquid interface. This non-planar interface causes Si grains to be misaligned with each other and thus eutectic spacing is variable. In a given system, spacing between two adjacent eutectic Si flakes ranges between a minimum, λ_m, and a maximum, λ_M, value. A third characteristic value, λ_e, represents the absolute minimum

Table 3.4: System-wide parameters used to determine eutectic growth velocity [77]

Parameter	Definition	Value
$\overline{m}$	weighted liquidus slope: $\overline{m} = \frac{\lvert m_\alpha\rvert m_\beta}{\lvert m_\alpha\rvert + m_\beta}$	5.25
C_0^*	weighted eutectic tie line (wt%)	87.7
D	diffusion coefficient $(\mu m^2/\text{s})$	4.3E3
P	function of volume fractions within eutectic; approximated as $P = 0.335(f_\alpha f_\beta)^{1.65}$	0.0089

Table 3.5: Phase-specific parameters used to determine eutectic growth velocity [77]

Parameter	Definition	Value for α-Al	Value for Si
f_α, f_β	volume fraction of phase within eutectic	0.873	0.127
Γ_α, Γ_β	Gibbs-Thomson coefficient (Km)	1.96E-7	1.70E-7
θ_α, θ_β	contact angle at three-phase junction	30°	65°
m_α, m_β	liquidus slope	-7.5	17.5

eutectic spacing possible for a system. Below λ_e, surface tension is too high for further growth, and grains that approach this value stop growing. Likewise, when λ becomes too large, branching occurs, decreasing its value. Eutectic spacing in any system is described by the dimensionless parameter ϕ (Equation 3.8), which is constant for a given system and independent of growth rate. For the Al-Si system, ϕ is 2.3 [79].

$$\phi = \frac{\lambda_a}{\lambda_e} = \frac{\lambda_m + \lambda_M}{2\lambda_e} \tag{3.8}$$

By integrating ϕ into Equation 3.5, Gunduz' treatment provides an alternative approach that correlates λ, V, and ΔT while considering the difference in undercooling of the phases in the eutectic and the non-planar solid liquid interface. This approach allows to replace

Equation 3.5 with 3.9 and 3.10 when considering irregular eutectics.

$$\Delta T = (1 + \phi^2)\frac{K_2}{\lambda} \tag{3.9}$$

$$V = \frac{K_2\phi^2}{K_1\lambda^2} \tag{3.10}$$

Solidification cooling rate and thermal gradient were estimated using a modification of the thermal analysis developed by Garcia et al [80], which considers unidirectional heat transfer at the solid/liquid interface during solidification of liquid metal in a mold. Spinelli et al [81] modified this analysis from a Cartesian to a radial coordinate system to describe heat transfer in a solidifying droplet produced by Impulse Atomization.

Figure 3.8 shows a schematic of a solidifying droplet and identifies the parameters used in this analysis. The energy balance between the newly formed solid and the existing solid is described by Equation 3.11, where k is the thermal conductivity of the solid, L is heat of fusion, and ρ_m is density of the liquid. Table 3.6 summarizes the values of k_m, L, and ρ_m used in this work.

$$k_m \cdot (\frac{dT}{dr}) = L \cdot \rho_m \cdot (\frac{dr_f}{dt}) \tag{3.11}$$

Table 3.6: Constants used to determine eutectic cooling rate and thermal gradient [45, 82, 83]

Parameter	Value	Units
k_m	397,300	J/kg
L	2400	kg/m^3
ρ_m	70	W/mK

$\frac{dT}{dr}$ and $\frac{dr_f}{dt}$ in Equation 3.11 can be understood as the thermal gradient throught the existing solid and the growth velocity of the solid/liquid interface. These can thus be replaced with G (thermal gradient) and V (growth velocity), and the energy balance can be described
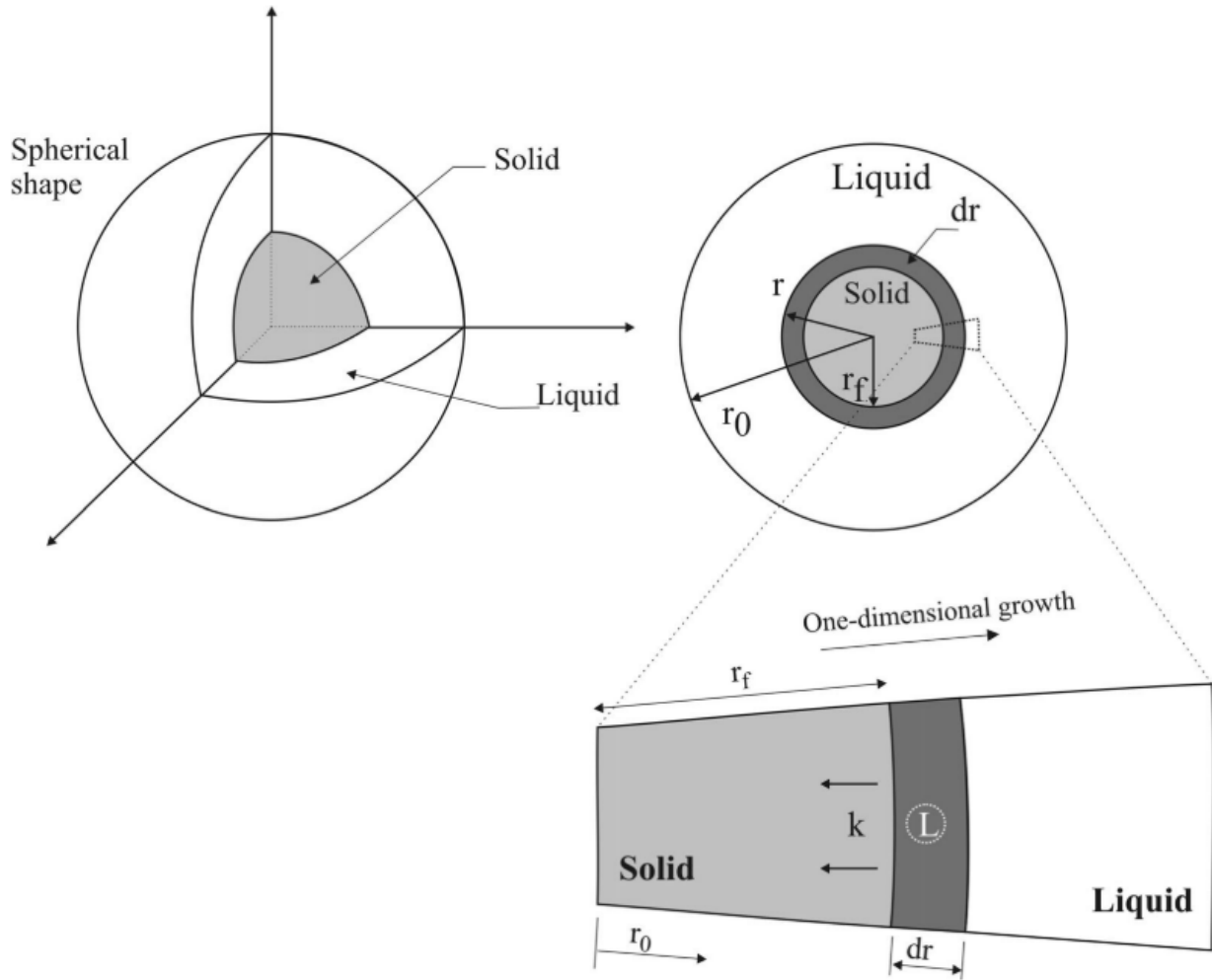
Figure 3.8: Schematic of solid/liquid interface in droplet produced by Impulse Atomization [81]

by Equation 3.12.

$$k_m \cdot G = L \cdot \rho_m \cdot V \tag{3.12}$$

Equation 3.12 can be further simplified as shown in Equation 3.13, where $C_1 = \frac{L \cdot \rho_m}{k_m}$.

$$G = C_1 \cdot V \tag{3.13}$$

The eutectic cooling rate (CR) can be defined by Equation 3.14.

$$CR = (\frac{dT}{dt}) = (\frac{dT}{dr}) \cdot (\frac{dr}{dt}) = G \cdot V \tag{3.14}$$

Equation 3.15 combines Equations 3.13 and 3.14 to define cooling rate solely as a function of growth velocity.

$$CR = C_1 \cdot V \tag{3.15}$$

Since growth velocity is determined using the modified Jackson-Hunt model described earlier in this chapter, G and CR can be obtained by solving Equations 3.15 and 3.13 using the eutectic spacing measurements obtained for Al-40Si.

3.10   Summary

This chapter discussed the experimental methods used to study rapidly solidified Al-40Si and variations of this alloy using Ce, Mg, and mixed Fe/Mn/Sc additions as modification agents. Samples of all four alloys were produced by Impulse Atomization to yield a wide range of powder sizes that allow to assess the effect that varying liquid cooling rate between 2,000 and 70,000 K/s has on their microstructure. The produced samples were sieved to separate the powders into different size ranges. To prepare the samples for analysis, powders of select sizes were mounted, ground, polished, and etched. Characterization efforts included Optical and Scanning Electron Microscopy to analyze the features present in each microstructure, and Electron Dispersive X-Ray Spectroscopy and X-Ray Diffraction to identify the phases present. Optical Microscopy images were used to quantify the distribution of various phases and components in the microstructure. Additionally, Differential Scanning Calorimetry was performed on as-atomized Al-40Si powders and eutectic spacing measurements were obtained from mounted Al-40Si samples.

Chapter 4

Rapidly-Solidified Al-40Si

This chapter explores the effects of rapid solidification on Al-40wt%Si alloy produced by Impulse Atomization. The Gulliver-Scheil solidification path of this alloy is presented as a baseline to understand the expected microstructure of this alloy when solidfied under local equilibrium conditions. The microstructure of Al-40Si is compared across a wide range of rapid solidification cooling rates. Microstructure quantification allows to compare microstructure distribution as a function of cooling rate and assess the deviation from local equilibrium during solidification.

4.1 Gulliver-Scheil solidification path

Figure 4.1 presents the solidification path of Al-40Si as predicted by the Gulliver Scheil (G-S) solidification model, which is based on local equilibrium conditions. This solidification path was produced using the TTAL7 database in ThermoCalc software. Table 4.1 lists the reactions that correspond to this solidification path, as well as the wt% produced, phases formed, and start temperature of each reaction.
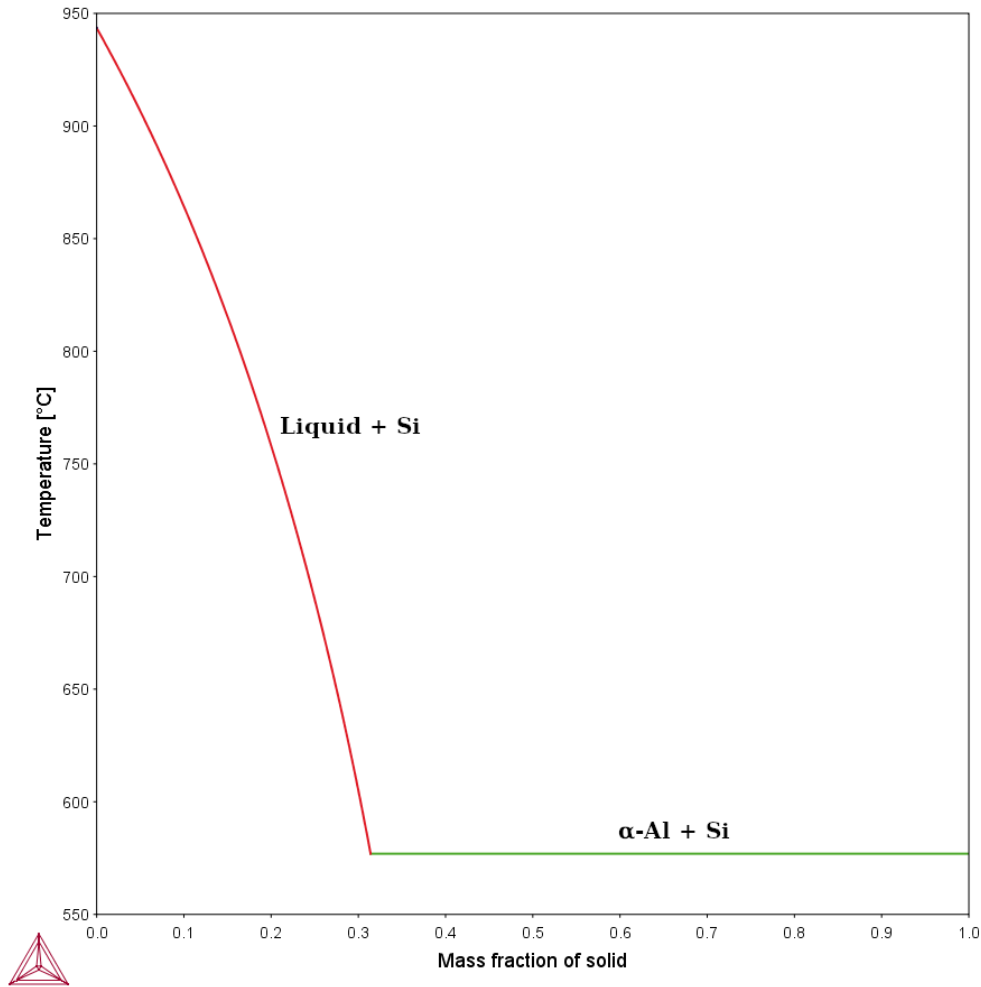
Figure 4.1: G-S solidification diagram for Al-40Si

Table 4.1: G-S Microstructural Distribution for Al-40Si

Component	wt%	Phases	Start T (C°)
Primary Si	31.4	Si	944
Binary eutectic	68.6	α-Al, Si	577

4.2 Phase transformations under DSC

DSC results obtained during heating of re-melted Al-40Si powders show two reactions peaks. As shown in Figure 4.2, these reaction peaks occured at 580-600 °C and 980-1100 °C, respectively. The linear correlation of the reaction temperatures as a function of scanning

rate provides estimated reaction temperature of 576.6 °C and 1076.2 °C under equilibrium conditions. Thus, the experimentally-determined eutectic reaction occurs 0.4°C below its equilibrium temperature, while primary Si melting occurs 139.2 °C above its equilibrium temperature.
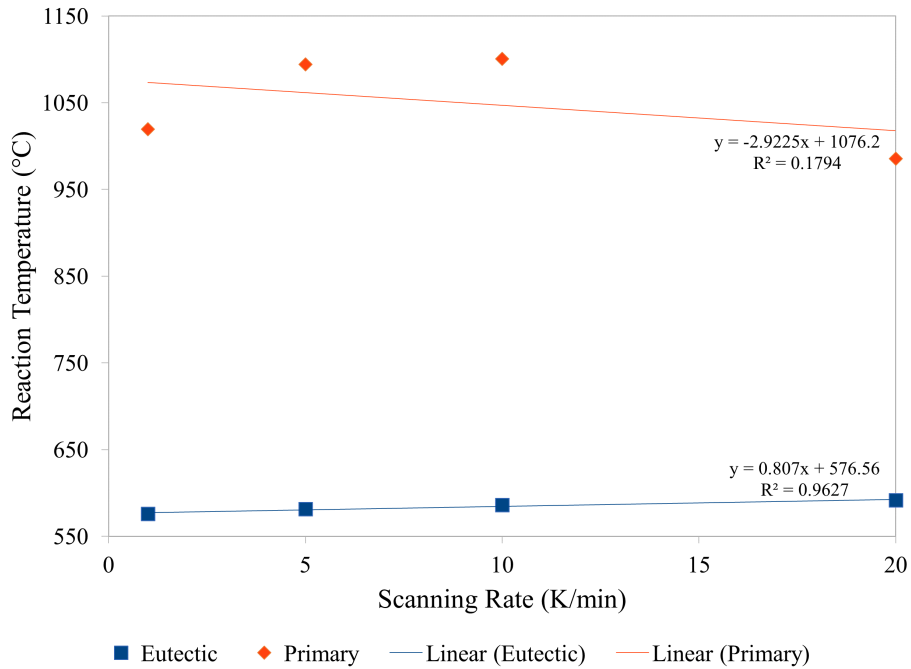
Figure 4.2: Reaction temperatures of Al-40Si determined by DSC

The R-squared value for curve that describes changes in eutectic temperature as a function of cooling rate indicates this curve is a good fit for the data obtained. In contrast, the low R-squared value of the primary Si curve corroborates this curve does not fit the primary Si data well. Considering the position of the data points, this arises from the lack of linearity in the correlation observed between cooling rate and primary Si melting temperature. It is unclear whether this non-linearity is a true representation of the correlation between cooling rate and primary Si melting temperature, or if it is a result of experimental errors. Regardless of the reason, the non-linearity of this correlation as observed means that the primary Si equilibrium melting temperature estimated from these results is unreliable.

4.3   Microstructure

Figure 4.3 shows the microstructure of Al-40Si from two powder sizes (90-106 and 710-850 μm diameter). With liquid cooling rates of 2,330 K/s (710-850 μm powders) and 69,900 K/s (90-106 μm powders), both microstructures were produced under rapid solidification (RS) conditions. These images thus allow a comparison of the effects of different extents of RS on the microstructure of the alloy. Qualitatively, the increase in cooling rate represented by decreasing powder size produces a finer microstructure, slightly modifies the morphology of primary Si, and introduces primary Si clustering within the droplets.

(a) 90-106 μm powder   (b) 710-850 μm powder
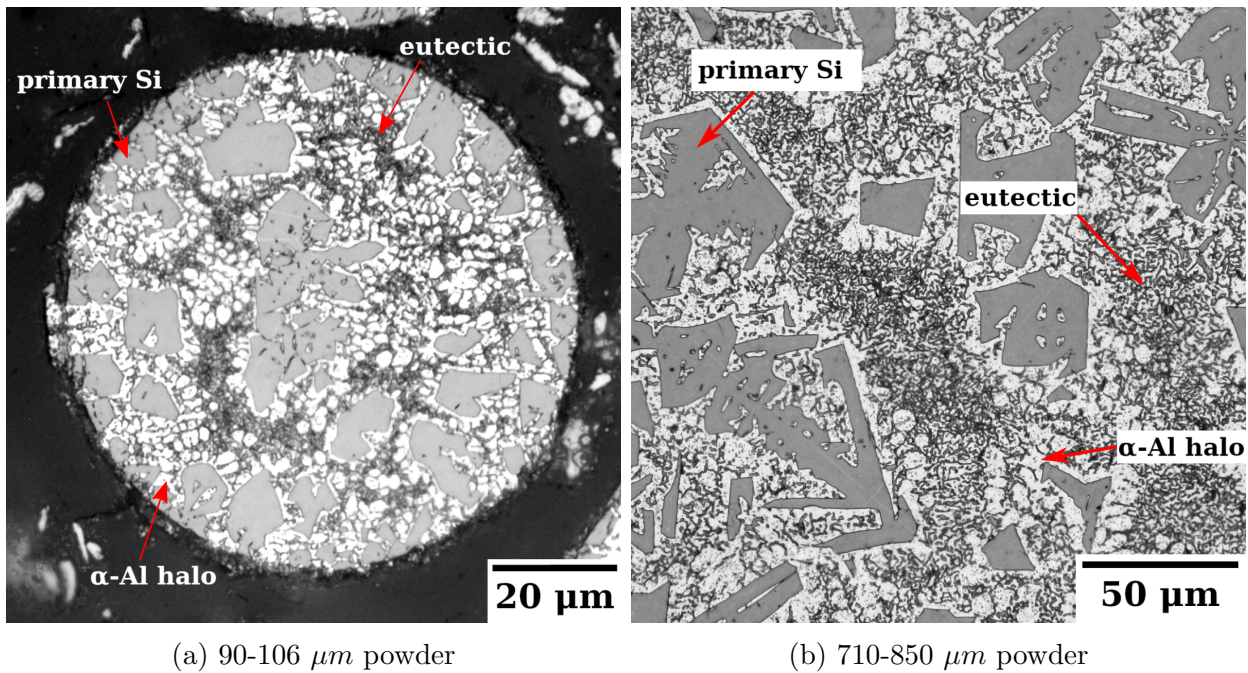
Figure 4.3: Microstructure of IA Al-40Si cooled in He

One of the most important similarities between these microstructures is the presence of an α-Al halo surrounding primary Si. The halo, which is not predicted by G-S, indicates the solidification conditions of these powders vary significantly from both global and local equilibrium conditions. Based on its positioning with respect to primary Si and the eutectic, the halo most likely formed after solidification of the primary Si phase and prior to eutectic solidification.

As shown in Figure 4.3a, solidification of Al-40Si at high a cooling rate produces a fine microstructure which contains primary Si grains with a lightly rounded surface. By contrast, Figure 4.3b shows the surface of primary Si formed at a much slower cooling rate is more angular. This angular nature is consistent with the faceting behaviour for which Si is known.

The high cooling rate associated with the small droplets shown in Figure 4.3a also introduced clustering of primary Si. This is most evident from the high density of primary Si at the centre and edges of the droplet. A secondary effect of this tendency is the formation of a ring of eutectic and halo that separates the two regions where clustering occurs. The presence of clustering heterogenizes the microstructure, which is likely to reduce the effectiveness of the composite-like nature of the interaction between α-Al and Si.

Figure 4.4 provides a magnified view of the eutectic structure present in Al-40Si under different extents of RS. As with the rest of the microstructure, the scale of the structure is the most evident difference between the eutectic of both powder sizes. These micrographs also show a significant change in the eutectic morphology. In both cases, eutectic Si morphology can be described as fibrous. However, there is a large difference in the eutectic Si aspect ratio visible in both droplets. In the larger droplet, eutectic Si is present as a mix of elongated and equiaxed structures. In contrast, the eutectic Si visible in the smaller droplet have a narrower distribution of aspect ratios. When put in the context of the reported morphology evolution as a function of cooling rate, the eutectic Si in the larger droplet can be clasified as fibrous with some flaky features, while that in the smaller droplet presents a mix of fibrous and globular features. These morphologies are consistent with the categories outlined in [18], where flaky eutectic Si is common at slower cooling rates and globular eutectic is predominant at high cooling rates.
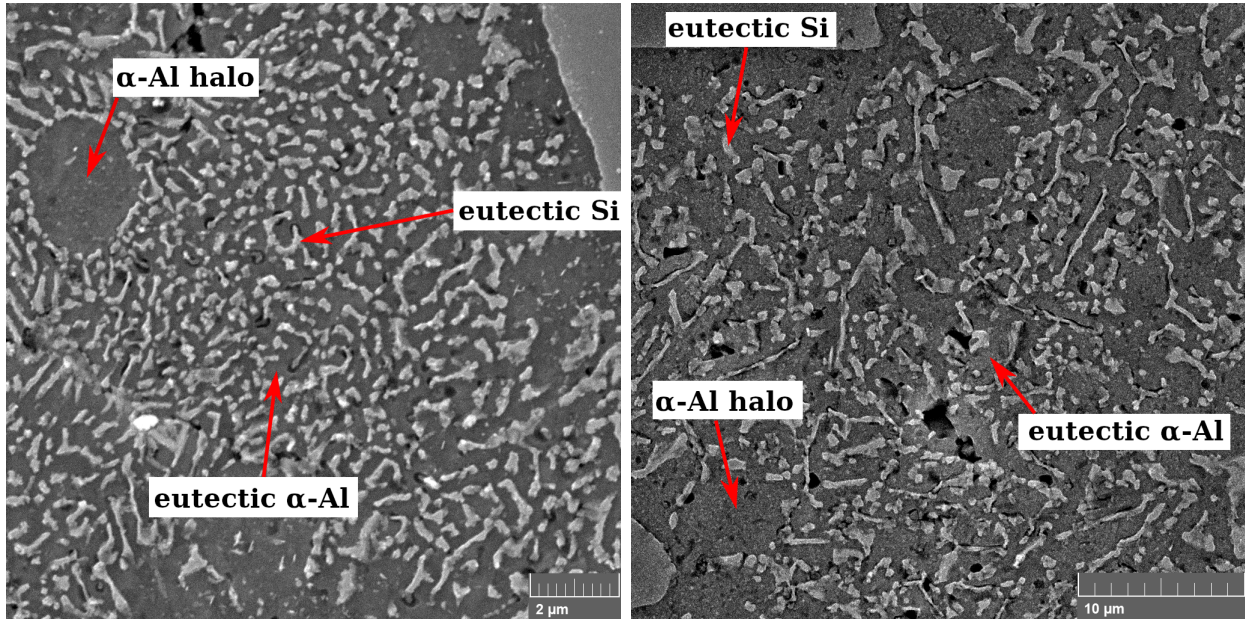
(a) 90-106 μm powder   (b) 710-850 μm powder

Figure 4.4: Eutectic structure of IA Al-40Si cooled in He

4.4 Effect of RS on microstructure distribution

Figure 4.5 presents the measured distribution of each microstructural feature present in Al-40Si as a function of liquid cooling rate. This diagram also provides the values of each component as predicted by G-S solidification. In discussing these results, it is important to consider that they were obtained by using 2D imaging to describe a 3D microstructure. This approach assumes any one cross-section of a given droplet is representative of the phase distribution in the whole droplet. In reality, due to the heterogeneous nature of the microstructure, this may not be the case.

Of the three measured curves shown in Figure 4.5, primary Si vol% shows the smallest variation as a function of cooling rate. Average values for this curve range from 32 to 37 vol%, but error bars of as much as 5 vol% mean there is significant overlap between adjacent data points. Two-sample t-tests (using a 95% confidence level) done to compare the data points on this curve indicate that the values at 8,540, 36,000, and 69,900 K/s are sufficiently different from that at 2,330 K/s to indicate primary Si vol% increases with cooling rate.
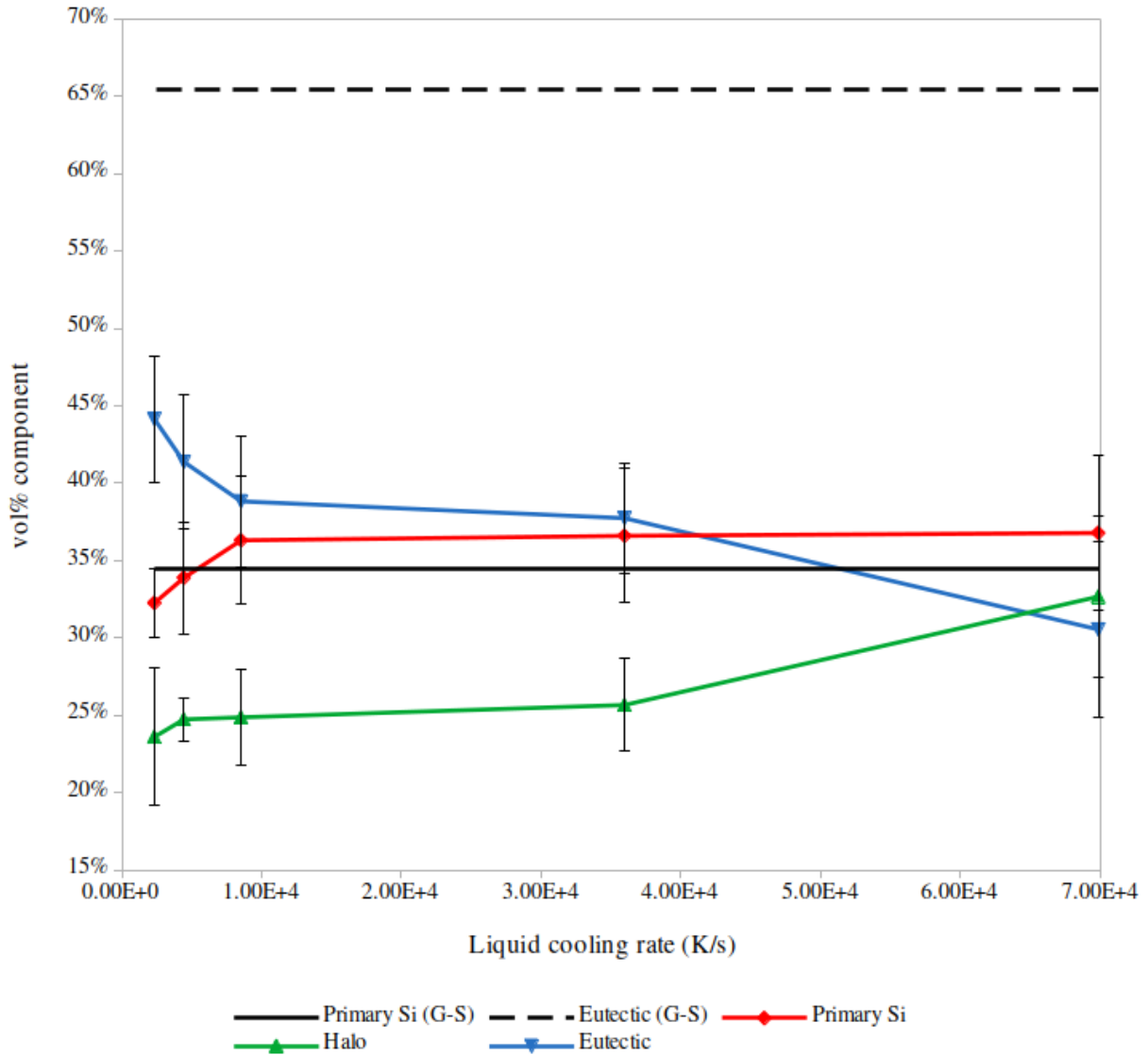
Figure 4.5: Measured microstructural distribution of IA Al-40Si cooled in He

Appendix C outlines the approach used in performing these t-tests.

Qualitatively, the halo and eutectic vol% curves show clearer correlations with cooling rate. Two-sample t-tests were done to compare the values of each curve at 2,330 and 69,900 K/s. In both cases, based on a 95% confidence level, the results indicate each halo and eutectic vol% have a non-zero correlation with liquid cooling rate. For the halo, this is a positive correlation. For the eutectic, there is a negative correlation between liquid cooling rate and measured vol%.

The observed increase in primary Si vol% and α-Al halo with cooling rate suggests an increase in the undercooling of each of their solidification reactions. This is consistent with a traditional understanding of nucleation in containerless atomization. Additionally, the assumption that a reaction takes place only in the time between its nucleation and nucleation of the next reaction leads to the conclusion that the undercooling of the eutectic reaction also increases with cooling rate.

Close to the left side of the diagram in Figure 4.5, the G-S and measured primary Si curves cross. To the left side of this point, the G-S values are larger than the measured ones. To the right of this point, the measured values are larger than the G-S ones. Given the understanding that nucleation undercooling increases with cooling rate, the measured primary Si curve should always be above the G-S curve.

In contrast to primary Si, the relative position of the G-S and measured eutectic curves is consistent with nucleation behaviour under RS. Measured eutectic vol% is lower than the G-S value for this structure across the range of tested cooling rates, and the gap between these two values increases with cooling rate. One reason behind this difference is the formation of a non-G-S product (halo). Arithmetically, the larger the vol% of this non-G-S structure, the less liquid will be available at the time of eutectic solidification.

4.5   Eutectic composition

Table 4.2 presents the compositions (in Si at%)of primary Si, halo, and eutectic measured in Al-40 using EDX. These values were calculated from 10-15 individual scans obtained for each structure in droplets of 90-106 and 500-600 μm diameter. Point scans were used to measure the composition of primary Si and the halo, and area scans were used to measure the composition of the eutectic. Table 4.3 contains the compositions of these phases at the eutectic temperature as determined from the phase diagram and G-S. Comparing the compositions shown in Tables 4.2 and 4.3 indicates a large deviation between the accepted

compositions of primary Si and α-Al and those measured in IA Al-40Si. The differences between these compositions are likely a result of multiple structures contributing to the EDX measurements due to the fine scale of the microstructure. This is supported by the large standard deviations observed in the primary Si and halo composition measurements shown in Table 4.2. The lower standard deviation of the measured eutectic composition suggests this value is more reliable than the measured primary Si and halo compositions. When compared to the phase diagram and G-S eutectic compositions, the measured eutectic composition is richer in Si.

Table 4.2: Primary Si, halo, and eutectic compositions measured in Al-40Si

Powder size (μm)	Primary Si (at% Si)	Halo (at% Si)	Eutectic (at% Si)
90-106	88.1 $\pm$ 7.0	12.4 $\pm$ 4.2	16.0 $\pm$ 1.0
500-600	95.1 $\pm$ 5.5	11.5 $\pm$ 7.0	16.8 $\pm$ 1.0

Table 4.3: Equilibrium and G-S compositions of Si and α-Al at the eutectic temperature

Phase	Equilibrium		G-S	
	wt% Al	wt% Si	wt% Al	wt% Si
Si	0.015	99.985	0	100
α-Al	98.4	1.6	97.62	2.38

The microstructure quantification presented in Figure 4.5 can be used to estimate the eutectic composition that results from assuming the measured primary Si, halo, and eutectic vol% to be reflective of the overall microstructure in a specific powder size. This approach provides an additional way to compare the degree of solute redistribution in IA Al-40Si to the perfect mixing assumption of the phase diagram and the G-S solidification model. Additionally, the estimated eutectic composition can be directly compared to the eutectic compositon measured by EDX. Estimating eutectic composition from primary Si and halo vol% requires to assume values of Si and Al solubility in α-Al and Si, respectively, to complete a mass balance of the alloy. Given the unreliability of the EDX measurements obtained for primary Si and the α-Al halo in these samples, equilibrium and G-S phase composition values are used

in this assessment. Specifically, these values correspond to the phase composition of each Si and α-Al in the eutectic structure (Table 4.3). The values in this table suggest that, while there are differences in the solubilities of Si and α-Al as a result of using equilibrium or G-S assumptions, these differences are minimal. The eutectic composition estimates that result from using these solubilities are indistinguishable when comparing the use of equilibrium and G-S assumptions.

Figure 4.6 provides estimated eutectic composition for all tested samples. The eutectic compositions plotted in this diagram were calculated using Equations 4.1, 4.2, and 4.3, where $x_{Si,eut}$ is the estimated fraction of Si in the eutectic by mass, $x_{Si,p}$ and $x_{Si,h}$ correspond to the fraction of Si in each primary Si and α-Al, respectively, and $wt\%_{eut}$, $wt\%_p$, and $wt\%_h$ are the measured mass percentage of each eutectic, primary Si, and halo in the microstructure. Figure 4.6 reflects the difference between G-S and EDX-measured eutectic composition previously identified. More importantly, this plot shows that both eutectic compositions resulting from measurements made on these samples (EDX and derived from vol%) are consistently higher than the eutectic's G-S composition. These combined observations strongly suggest a significant deviation between IA Al-40Si and G-S.

$$x_{Si,eut} = \frac{40\% - (wt\%_{Si,p} + wt\%_{Si,h})}{wt\%_{eut}} \tag{4.1}$$

$$wt\%_{Si,p} = x_{Si,p} \cdot wt\%_p \tag{4.2}$$

$$wt\%_{Si,h} = x_{Si,h} \cdot wt\%_h \tag{4.3}$$

4.6   Effect of RS on eutectic growth

Figure 4.7 shows how eutectic spacing varies as a function of powder size. This plot suggests a strong positive correlation powder diameter and and eutectic spacing. This is consistent
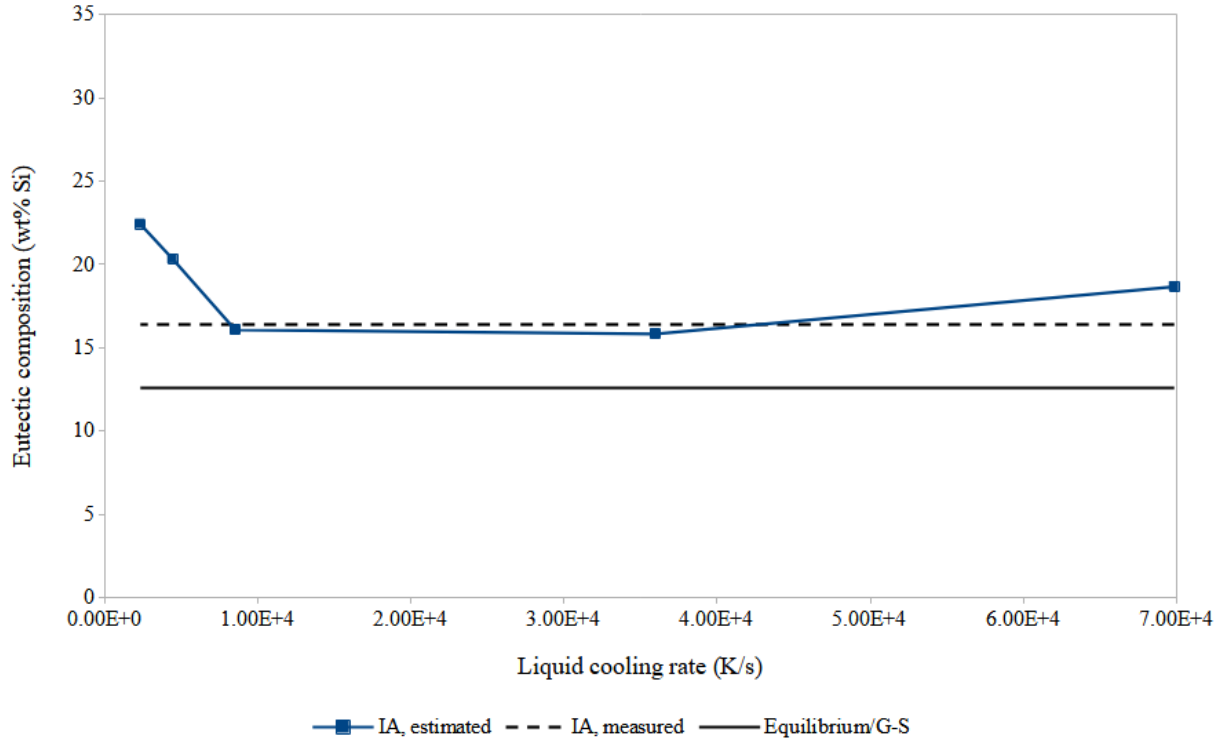
Figure 4.6: Estimated eutectic composition as a function of liquid cooling rate

with a traditional understanding of heat and mass transfer, where smaller droplets tend to experience faster heat extraction, which results in finer microstructures. The eutectic spacings shown in Figure 4.7 can be used to estimate the average growth velocity, and undercooling during eutectic growth.

Figures 4.8 presents the eutectic spacing measured in Al-40Si as a function of eutectic growth velocity. Eutectic growth velocity was estimated using the modified Jackson-Hunt model proposed by Gunduz et al [77]. These results indicate a negative correlation between eutectic growth velocity and spacing. Growth velocity was used to calculate the average solidification cooling rate and thermal gradient during eutectic growth. This was achieved using Spinelli et al's modification of the thermal analysis developed by Garcia et al [81, 80]. Detailed descriptions of this thermal analysis and Gunduz' model can be found in Chapter 3.

Figure 4.9 provides a eutectic growth map describing the relationship between eutectic
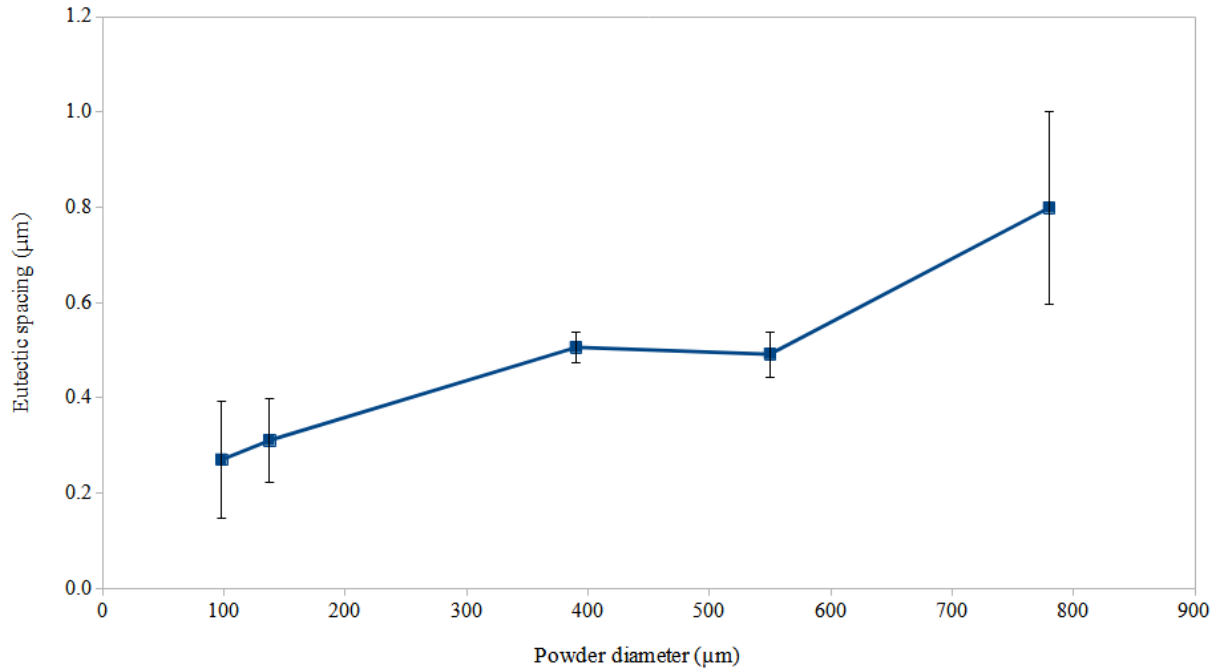
Figure 4.7: Eutectic spacing as function of powder size for Al-40Si
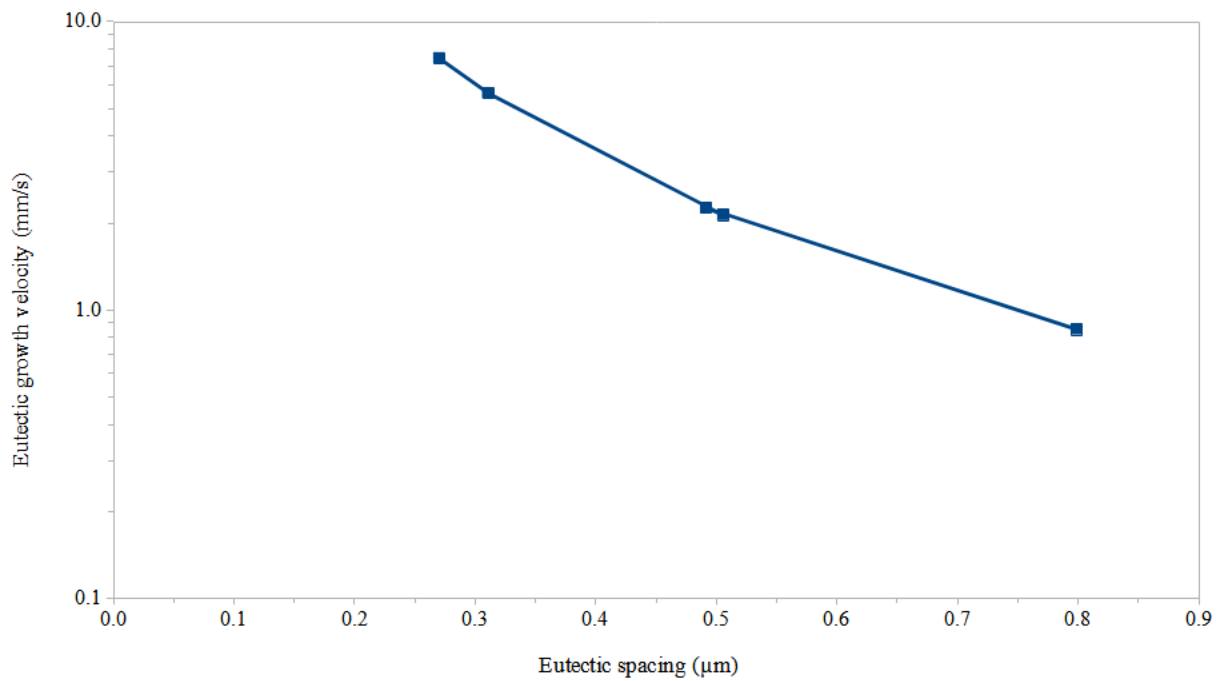
Figure 4.8: Eutectic growth rate as function of eutectic spacing for Al-40Si

68

growth velocity, thermal gradient (G), solidification cooling rate, and morphology. Use of growth velocity and the inverse of the thermal gradient as axes results in cooling rate varying diagonally across the plot. This allows to consider the relationship between cooling rate and morphology. As described in Section 4.3, flaky, fibrous, and globular + fibrous morphologies were observed in these powders. Morphology classification was based on the predominant eutectic Si morphology observed in 10 droplets when viewed in SEM. Based on these classifications and the average eutectic solidification cooling rate for each powder size analyzed, eutectic Si morphology changes from flaky to fibrous at approximately 70 K/s and from fibrous to fibrous + globular at around 800 K/s.
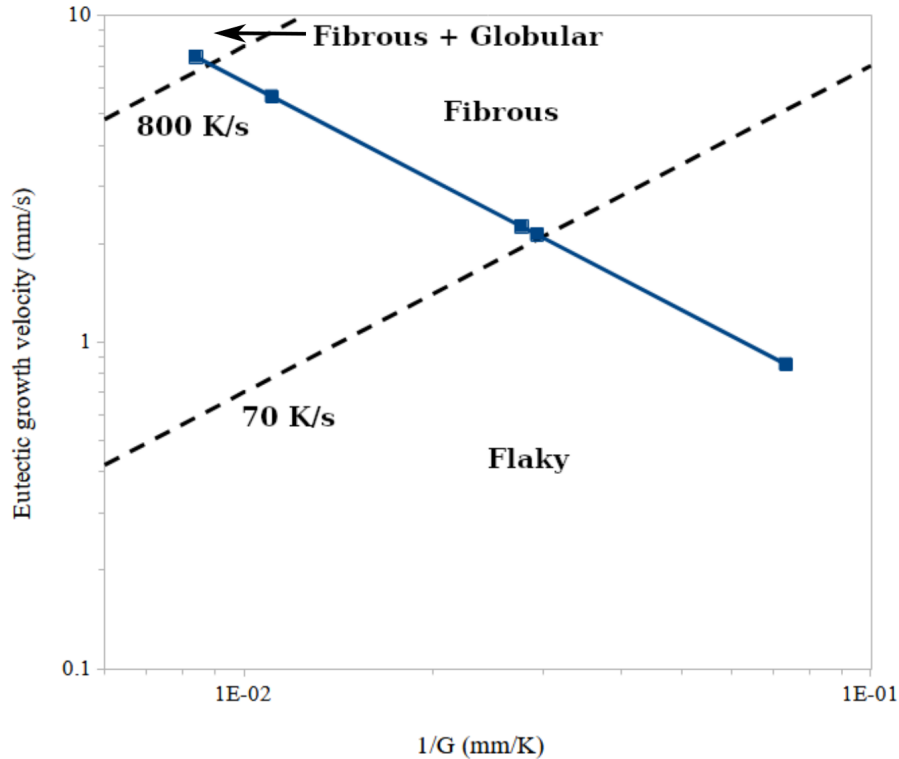
Figure 4.9: Eutectic growth map for Al-40Si

4.7 Summary

The microstructure of IA Al-40Si contains primary Si, an α-Al halo, and a binary Al-Si eutectic. The presence of a halo identifies a significant deviation in the solidification path of this alloy from that described by the phase diagram and the Gulliver-Scheil solidification model. Increasing cooling rate was associated with a refinement of the microstructure, clustering of primary Si, a decrease in primary Si surface faceting, increasing primary Si and halo vol%, and a decrease in eutectic vol%. Eutectic composition was determined to be more Si-rich in the IA samples used here than their equilibrium and G-S compositions. Eutectic spacing showed a positive correlation with powder size, and eutectic growth velocity displayed a negative correlation with eutectic spacing and powder size. Eutectic growth velocity and thermal gradient were used to determine morphology transition temperatures for eutectic Si. Predominant eutectic morphology changes from flaky to fibrous at 70 K/s, and from fibrous to globular + fibrous at 800 K/s.

Chapter 5

Chemically-modified Al-40Si

This chapter discusses the effects of three chemically-modified alloys derived from the initial Al-40Si composition introduced in Chapter 4. Each Ce, Mg, and a combined Fe, Mn, and Sc additions were used to modify the morphology of primary Si. The resulting primary Si morphology, as well as other changes in microstructure that were affected by chemical modification are outlined. A quantitative assessment of the primary Si content in each alloy is also presented.

5.1 Al-40Si-1.5Ce

Cerium has been used in the literature to modify primary and eutectic Si. The modification mechanism used by Ce is thought to be based on limiting Si growth through rejection of Ce from this phase and buildup of the same around Si grains. The existing body of work largely focuses on use of this element as a modifier under casting conditions (cooling rates up to 130 K/s). In this section, the use of Ce to modify Si in a rapidly solidified Al-40Si alloy is discussed.

5.1.1 Gulliver-Scheil solidification path

Figure 5.1 outlines the solidification path of Al-40Si-1.5Ce (composition in wt%) as predicted by the Gulliver-Scheil (GS) solidification model. This solidification path was determined using the TCAL7 database (version 7.1) in Thermo-Calc 2021a software. According to G-S, solidification under local equilibrium conditions should take place in six distinct reactions. Table 5.1 summarizes the phases produced by each reaction, starting reaction temperature, and quantitative contribution of each reaction to the final microstructure.

Table 5.1: G-S Microstructural Distribution for Al-40Si-1.5Ce

Reaction	wt%	Phases	Start T (°C)
Primary Si	13.2	Si	942.8
First two-phase reaction	14.6	Si, $CeSi_2$	830.9
Second two-phase reaction	1.3	Si, AlCeSi	670.5
Third two-phase reaction	3.4	Si, $AlCeSi_2$	650.5
Fourth two-phase reaction	0.7	Si, $Al_4Ce_3Si_6$	591.7
Ternary eutectic	66.8	α-Al, Si, $Al_4Ce_3Si_6$	577.0

5.1.2 Microstructure

Figure 5.2 shows the microstructures present in two Al-40Si-1.5Ce powders of different sizes. The microstructure shown in Figure 5.2a corresponds to a 90-106 μm droplet, and experienced a liquid cooling rate of 69,800 K/s. The microstructure in Figure 5.2b is of a 710-850 μm droplet, and was cooled at 2,370 K/s. In both microstructures, three features, namely primary Si, α-Al halo, and eutectic, are visible. As in Al-40Si, the α-Al halo is not part of the G-S solidification path for this alloy, and its presence in the microstructure indicates a significant deviation from equilibrium conditions.

Figure 5.3 shows the microstructures of Al-40Si in powders of 90-106 μm and 710-850 μm diameters. These were originally presented in Chapter 4 and are replicated here to allow a comparison between the microstructures of Al-40Si and Al-40Si-1.5Ce. Estimated liquid cooling rates prior to the solidification of these droplets are 69,900 K/s (90-106 μm powders)
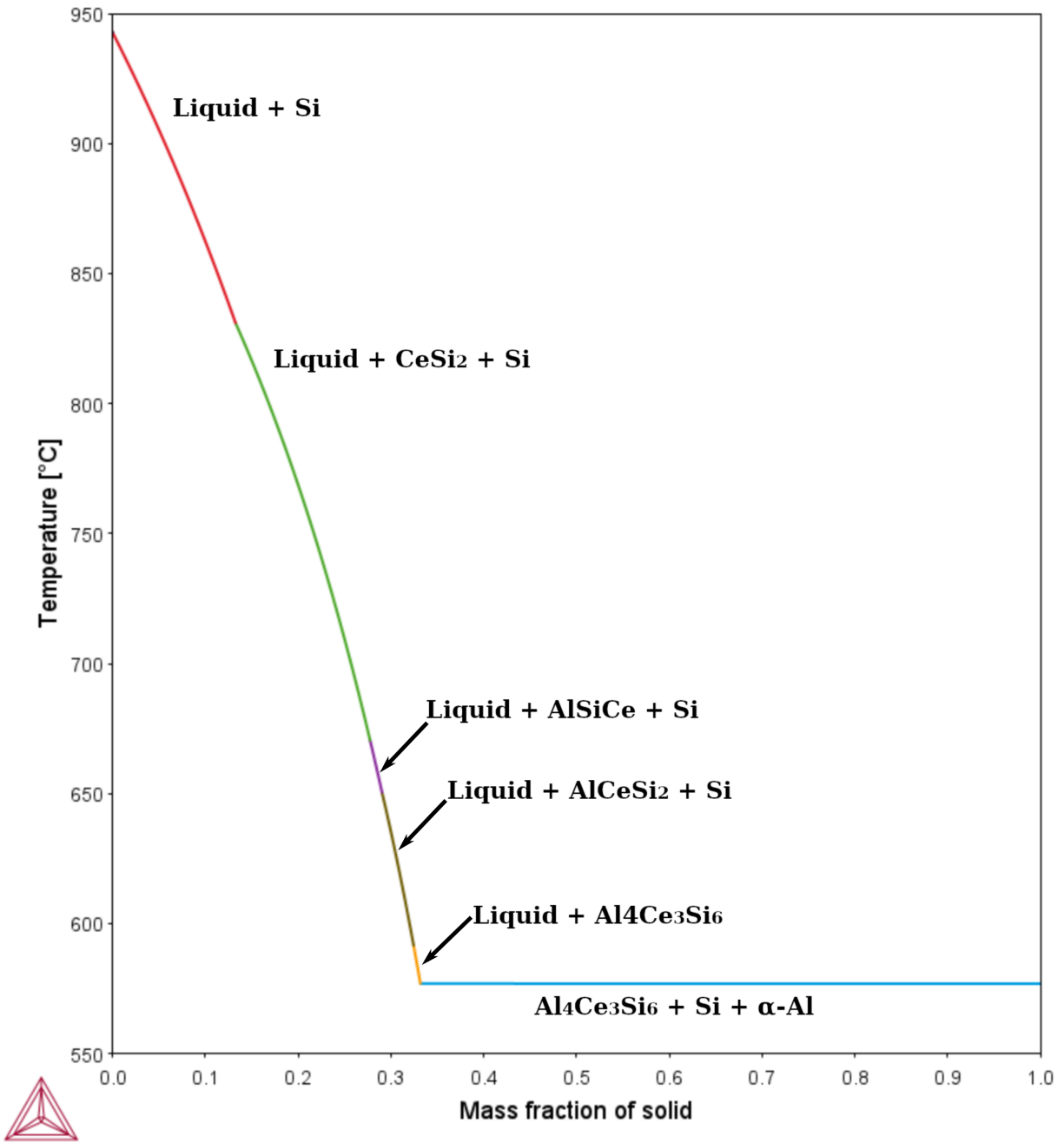
Figure 5.1: GS solidification diagram for Al-40Si-1.5Ce

and 2,330 K/s (710-850 μm powders). Comparing both sets of droplets allows to qualitatively assess the effect of Ce modification on rapidly solidified powders and the effect of RS on a Ce-modified alloy.
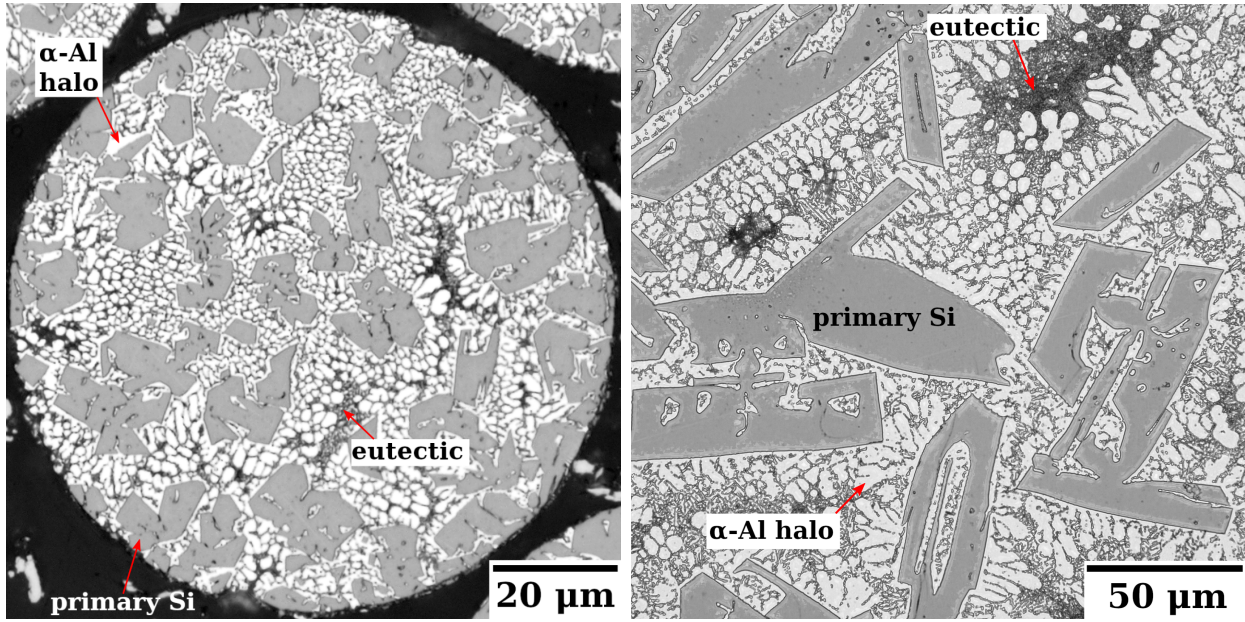
(a) 90-106 μm powder

(b) 710-850 μm powder

Figure 5.2: Microstructure of IA Al-40Si-1.5Ce cooled in He
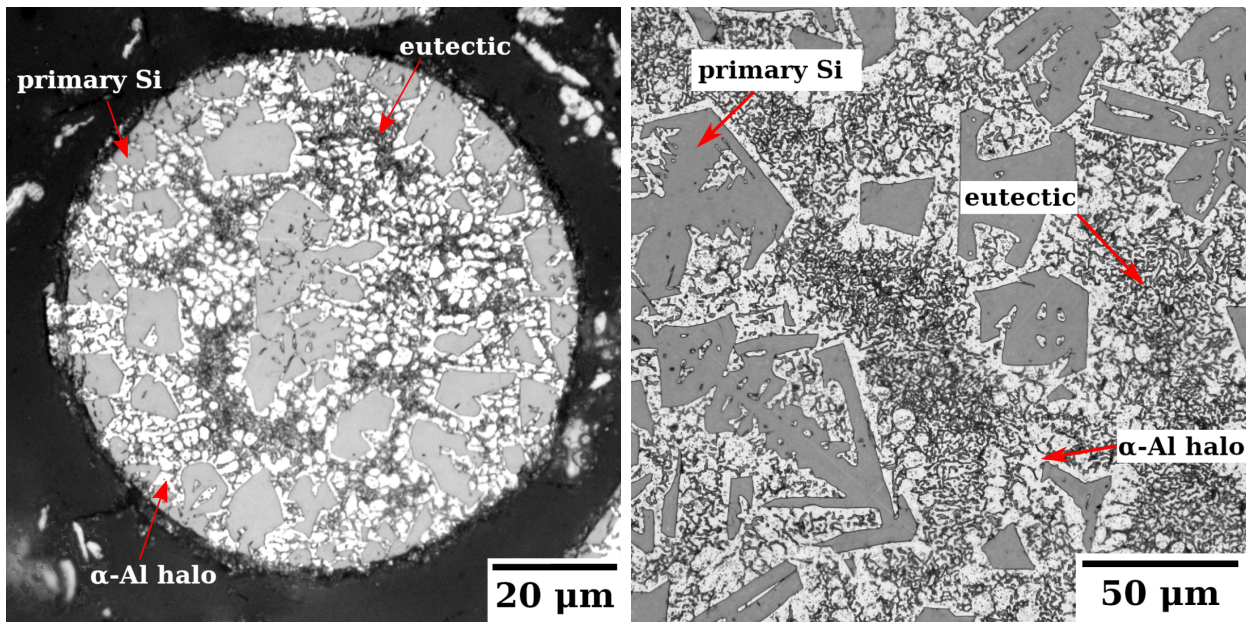
(a) 90-106 μm powder

(b) 710-850 μm powder

Figure 5.3: Microstructure of IA Al-40Si cooled in He

As in Al-40Si, primary Si faceting decreases with increasing cooling rate in Al-40Si-1.5Ce. Figures 5.2a and 5.3a show similar extents of rounding at the primary Si surface. These instances can be contrasted to the sharp primary Si surfaces shown in Figures 5.2b and 5.3b.

These differences suggest that the use of Ce does not affect the effect that RS has on primary Si surface faceting for liquid cooling rates between 2,000 and 70,000 K/s.

In contrast to Al-40Si, however, Ce does appear to have palpable effect on the clustering of primary Si grains. In Al-40Si, the smallest powder sizes (90,106 μm, Figure 5.3a) present significant primary Si clustering at the centre and towards the edges of the droplets. In Al-40Si-1.5Ce, no such behaviour is observed (Figure 5.2a). This difference suggests the use of Ce lead to a more homogeneous primary Si distribution in Al-40Si-1.5Ce. More importantly, this improvement in the microstructure's distribution is likely to enhance its composite-like nature.

Figure 5.4 shows the phase distribution within the eutectic structure for powder sizes 90-106 μm and 850-1000 μm. These powders experienced estimated liquid cooling rates of 69,800 K/s and 1,750 K/s, respectively. In the eutectic of both powder sizes, three phases can be distinguished: α-Al, Si, and an intermetallic compound. The eutectic is of an irregular nature where α-Al serves as the matrix within which Si and intermetallic grains are embedded. Comparing this structure with the binary Al-Si eutectic, α-Al and Si maintain similar roles, while intermetallic grains interact with the rest of the structure in a manner akin to that of Si.

While primary Si morphology is not significantly affected by the addition of Ce, the morphology of eutectic Si is. In Figures 5.4a and 5.4b, eutectic Si presents a mostly fibrous morphology. The smaller and faster cooled droplet (Figure 5.4a) contains some globular eutectic Si grains, while in the larger and slower cooled droplet (Figure 5.4b) eutectic Si is purely fibrous. These observations can be contrasted with Al-40Si, which had fibrous eutectic Si in its 90-106 μm droplets and fibrous + flaky eutectic Si in its 710-850 μm droplets. For both powder sizes, the eutectic Si morphology present in the Al-40Si-1.5Ce is associated with faster eutectic solidification rates than the eutectic Si morphology found in the Al-40Si samples. This suggests that the use of Ce led to an increase in eutectic growth rates for liquid cooling rates between 2,000 and 70,000 K/s.

(a) 90-106 μm powder (b) 850-1000 μm powder
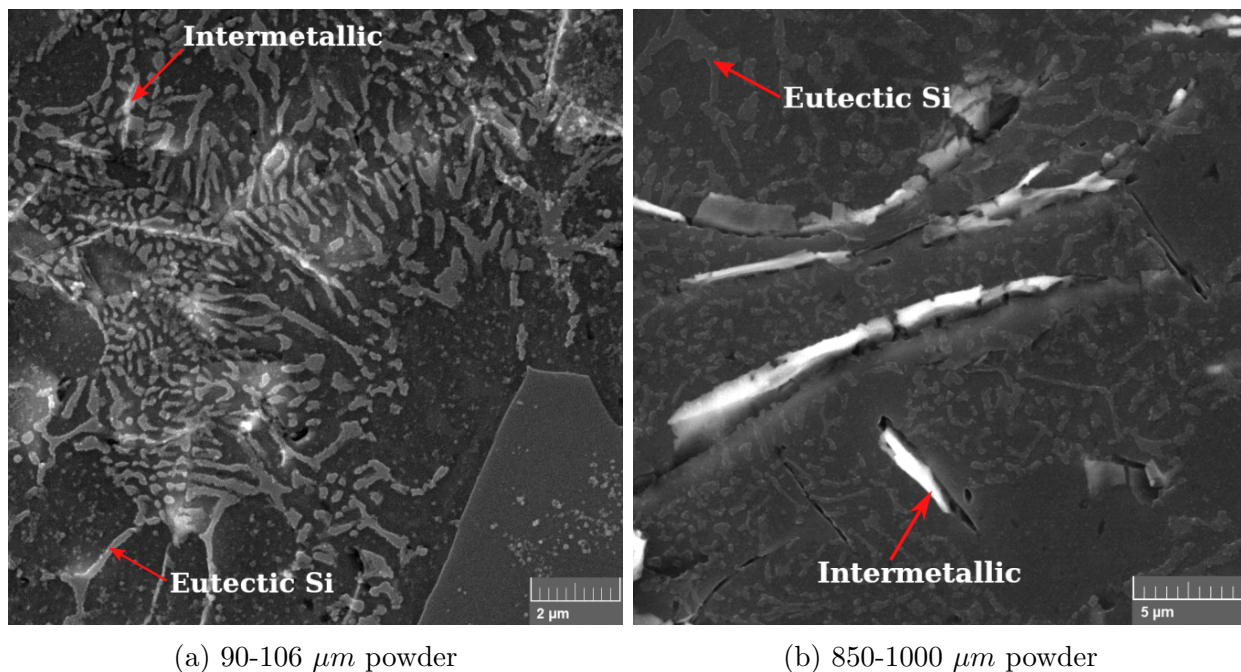
Figure 5.4: Eutectic structure of IA Al-40Si-1.5Ce cooled in He

Tables 5.2, 5.3, and 5.4 provide the average composition of primary Si, the α-Al halo, and the eutectic in Al-40Si-1.5Ce as determined from EDX. These tables also contain the measured composition of these components in Al-40Si to allow a comparison between the two alloys. Similarly to Al-40Si, measured primary Si and halo composition has a large standard deviation and differs significantly from the G-S values for Si and α-Al. This suggests the measured composition of these components is not reliable. The measured eutectic compositions are similar for both alloys and their average values range from 16.0 to 17.0 wt% Si. As with Al-40Si, the eutectic in Al-40Si-1.5Ce appears to be richer in Si than G-S. Based on Table 5.2, Ce does not seem to be soluble in Si for these samples, and according to Table 5.3, the solubility of Ce in α-Al is inconclusive. These observations suggest the Ce content measured in the eutectic of Al-40Si-1.5Ce results from the Ce-containing intermetallic present in the eutectic rather than Ce solute within Si or α-Al.

Table 5.2: Measured primary Si composition in IA Al-40Si-1.5Ce

Alloy	Powder diameter (μm)	at% Si	at% Al
Al-40Si	90-106	88.1 ± 7.0	11.9 ± 7.0
	500-600	95.1 ± 5.5	4.9 ± 5.5
Al-40Si-1.5Ce	90-106	87.9 ± 6.1	12.1 ± 6.1
	500-600	94.6 ± 5.6	5.4 ± 5.6

Table 5.3: Measured halo composition in IA Al-40Si-1.5Ce

Alloy	Powder diameter (μm)	at% Si	at% Al	at% Ce
Al-40Si	90-106	12.4 ± 4.2	87.6 ± 4.2	-
	500-600	11.5 ± 7.0	88.5 ± 7.0	-
Al-40Si-1.5Ce	90-106	10.5 ± 2.8	89.1 ± 2.8	0.4 ± 0.2
	500-600	10.6 ± 6.5	89.2 ± 6.7	0.3 ± 0.5

Table 5.4: Measured eutectic composition in IA Al-40Si-1.5Ce

Alloy	Powder diameter (μm)	at% Si	at% Al	at% Ce
Al-40Si	90-106	16.0 ± 1.0	84.0 ± 1.0	-
	500-600	16.8 ± 1.0	83.2 ± 1.0	-
Al-40Si-1.5Ce	90-106	17.0 ± 4.1	82.4 ± 4.1	0.5 ± 0.2
	500-600	16.0 ± 4.2	83.7 ± 4.4	0.4 ± 0.4

5.1.3 Effect of RS on microstructure distribution

Figure 5.5 shows the quantification of primary Si, halo, and eutectic (in vol%) in Al-40Si-1.5Ce as a function of liquid cooling rate. The trends observed for this alloy are consistent with those seen in Al-40Si. Average primary Si and halo vol% increase, while eutectic content in the microstructure decreases, as cooling rate increases. As with Al-40Si, these trends are largely explained by an increasingly larger difference in nucleation temperature of consecutive reactions, which results from an unequal variation in the undercoolings of primary Si, halo, and eutectic solidfication as cooling rate increases.

Figure 5.6 provides a comparison of the region-of-confidence for the halo content in each Al-40Si and Al-40Si-1.5Ce as a function of liquid cooling rate. The regions of confidence presented are a result of the sum of the average halo content and halo error bars for each
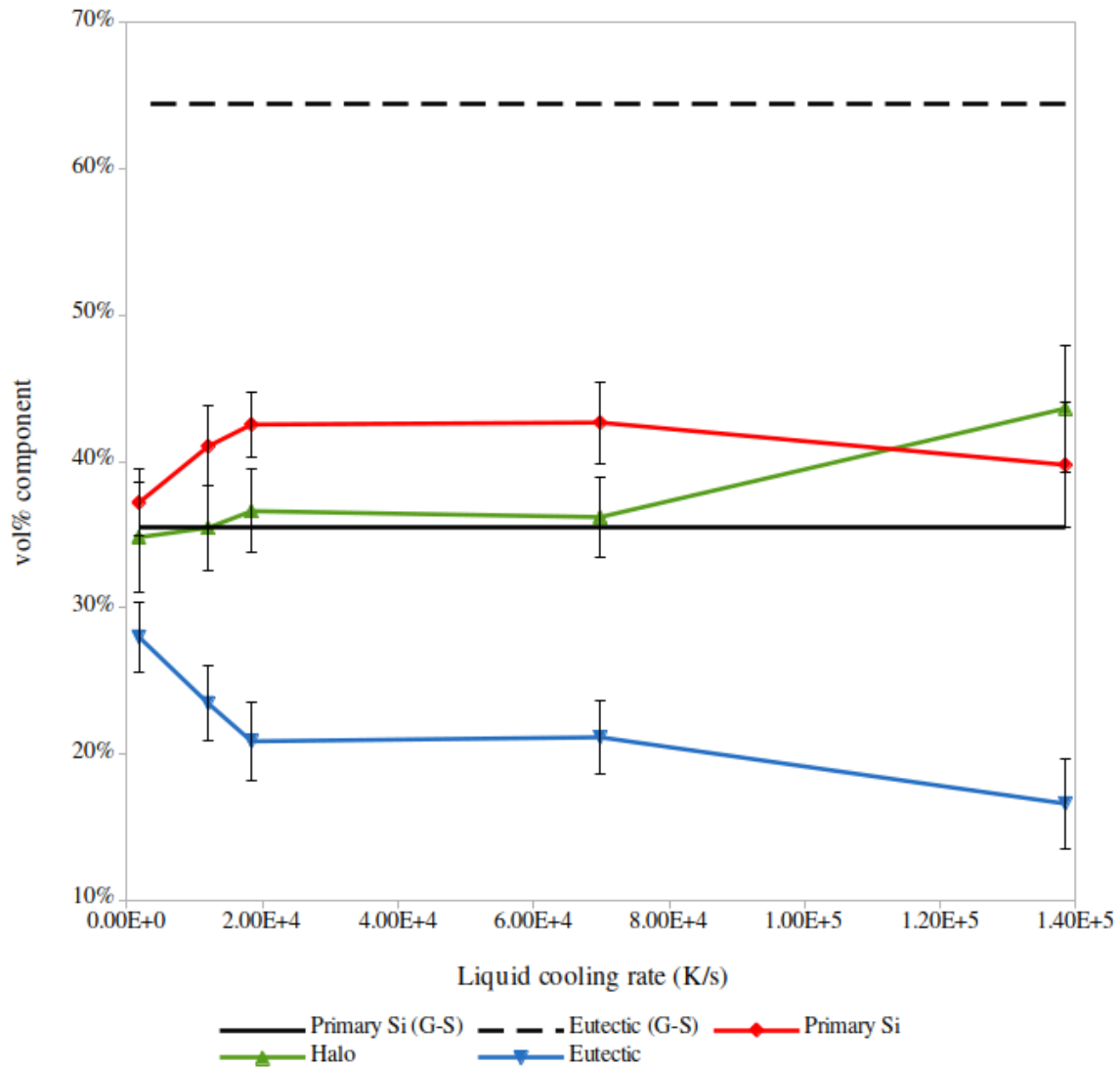
Figure 5.5: Measured microstructural distribution of IA Al-40Si-1.5Ce

alloy. This comparison shows that for most of the range of cooling rates for which halo content of both alloys was measured, no overlap exists between the regions-of-confidence of the two alloys. Specifically, the halo region of confidence for Al-40Si-1.5Ce is consistenly higher than that of Al-40Si. The two regions-of-confidence only overlap for the highest cooling rates tested (close to 70,000 K/s). This evidence suggests that the addition of Ce led to a significant increase in the amount of α-Al halo present in the microstructure under intermediate cooling rates (2,000 to 18,000 K/s).
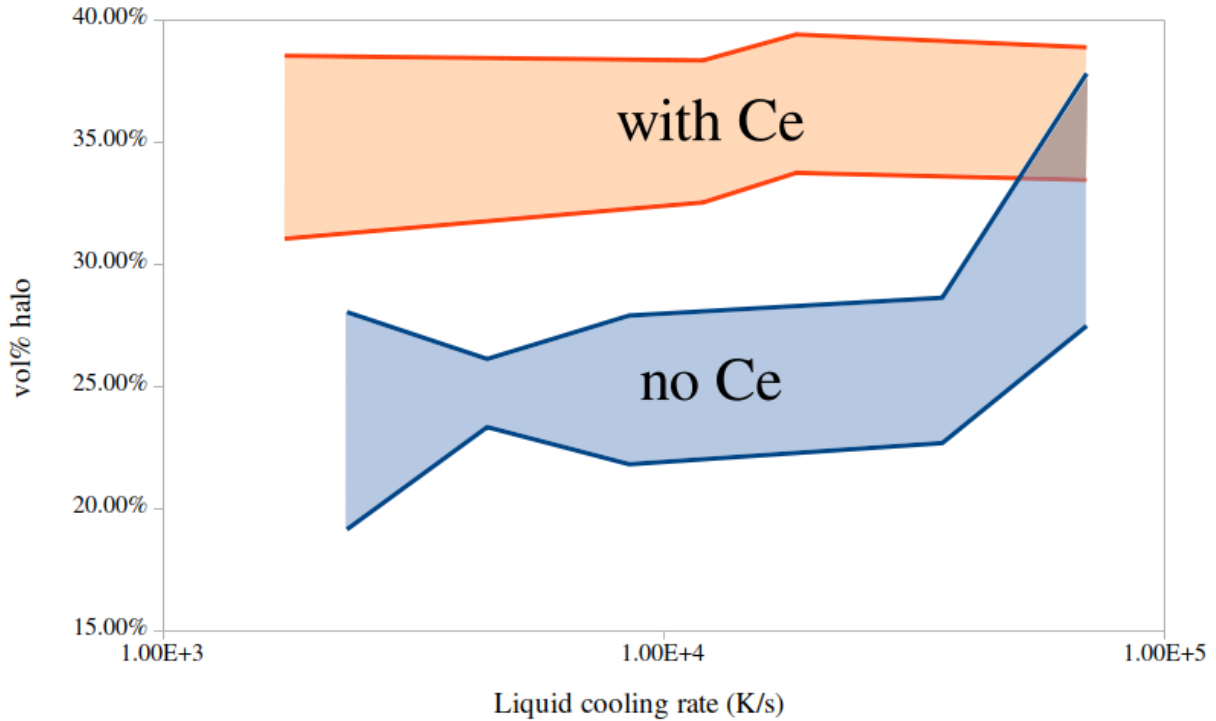
Figure 5.6: Halo region-of-confidence comparison for Al-40Si and Al-40Si-1.5Ce

The primary Si vol% curve shown in Figure 5.5 sees a slight decrease for the highest cooling rate tested for this alloy (138,000 K/s). Both the primary Si curve in Al-40Si and the rest of the primary Si curve in this alloy (between 1,750 and 69,800 K/s) show either an increase or no change in primary Si as cooling rate increases, rendering this change unexpected. Primary Si vol% measurements taken on Al-40Si do not provide a viable comparison for this data point, as no powders below 90-106 μm diameter were available for Al-40Si. However, the regions-of-confidence for the data points at 69,800 K/s and 138,000 K/s in Figure 5.5 support the possibility of a plateauing primary Si vol% curve. The lower end of each region-of-confidence is 39.9% and 35.5%, while the upper limit is 45.5% and 44.0%. According to a two-sample t-test done on these data points, there is not enough evidence to indicate their respective true primary Si vol% are statistically different (when using a 95% confidence level). As such, the primary Si vol% decrease measured between 69,800 K/s and 138,000 K/s could be attributed to sampling rather than an underlying metallurgical phenomenon.

79

5.1.4 Summary

The microstructure of IA Al-40Si-1.5Ce contains primary Si, an α-Al halo, and a eutectic structure. The formation of an α-Al halo in this alloy is part of this alloy's phase diagram of Gulliver-Scheil solidification paths. This suggests solidification of this alloy significantly deviated from global and local equilibrium conditions. Increasing cooling rate led to a similar decrease in primary Si surface faceting as that observed in Al-40Si. In contrast to Al-40Si, Al-40Si-1.5Ce did not present significant primary Si clustering in small powders. Primary Si and halo vol% increased as a function of increasing cooling rate, while eutectic vol% decreased. Phase fractions thus evolved similarly in this alloy as they did in Al-40Si. However, the use of Ce in this alloy led to an increase the halo vol% in the microstructure for intermediate cooling rates with respect to that in Al-40Si.

5.2 Al-40Si-9.2Mg

This section describes the effects of using Magnesium as a chemical modifier in an Al-40Si alloy solidified under rapid solidification conditions. The microstructure of IA Al-40Si-9.2Mg is used to identify deviations between the IA and Gulliver-Scheil solidification paths of this alloy.

5.2.1 Gulliver-Scheil solidification path

Figure 5.7 presents the solidification path of Al-40Si-9.2Mg as pedicted by the Gulliver-Scheil (G-S) solidification model. This solidification path was calculated using the TTAL7 database (version 7.1) in Thermo-Calc 2017a software. According to G-S, solidification of this alloy under local equilibrium conditions should take place in three reactions. Table 5.5 summarizes the phases expected to form in each reaction, starting reaction temperature, and quantitative distribution in the microstructure.
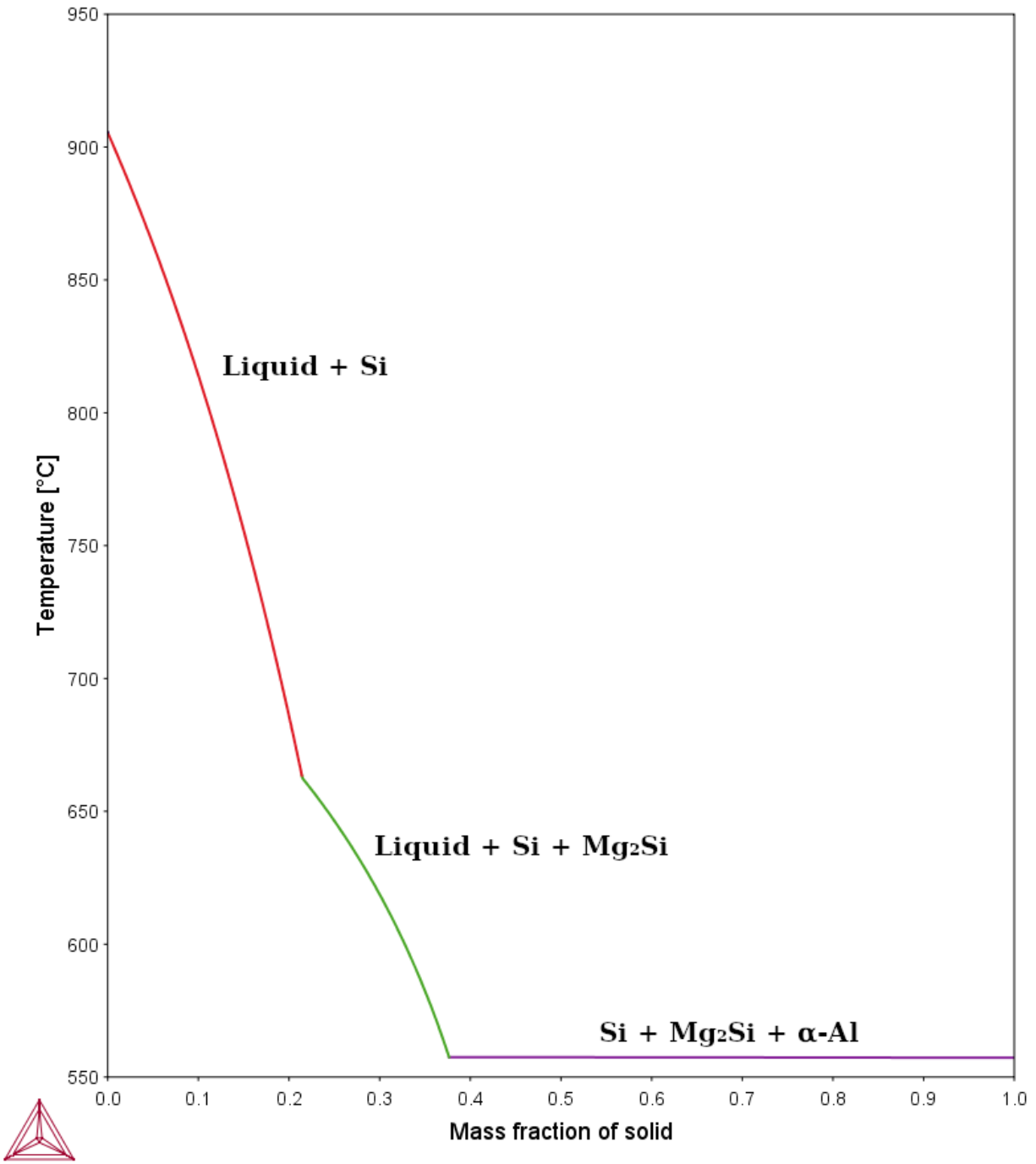
Figure 5.7: G-S solidification diagram for Al-40Si-9.2Mg

Table 5.5: G-S Microstructural Distribution for Al-40Si-9.2Mg

Reaction	wt%	Phases	Start T °C
Primary Si	21.4	Si	905.5
Two-phase reaction	16.2	Si, Mg_2Si	662.5
Ternary eutectic	62.4	α-Al, Si, Mg_2Si	557.3

5.2.2 Microstructure

Figure 5.8 shows the microstructure of Al-40Si-9.2Mg solidified under a high and a low liquid cooling rate. The microstructure in Figure 5.8b experienced a cooling rate of 2,220 K/s, and that in Figure 5.8a was cooled at 49,000 K/s. The same features can be observed in both microstructures. Primary Si is characteristically large in comparison to the rest of the microstructure and can best be described as a grey faceted plate. The α-Al halo is distributed throughout the microstructure and generally surrounds primary Si. As with Al-40Si, presence of the halo indicates deviation from local equilibrium conditions during solidification of this alloy. The dark grey single-arm dendrites scattered throughout the microstructure are Mg_2Si. The remaining solid, which has the finest structure in each image is the ternary eutectic. The microstructures shown in Figure 5.8 differ from Al-40Si in the extent of primary Si clustering, interfacial rounding, and aspect ratio.

Figure 5.9 shows the microstructure of an Al-40Si droplet of 106-125 μm diameter. With a liquid cooling rate of 50,300 K/s, this is the best Al-40Si size to which Figure 5.8a can be compared. In the Al-40Si microstructure, primary Si present a somewhat rough surface, which is consistent with the decrease in faceting behaviour as a function of increasing cooling rate previously reported (Chapter 4). In Al-40Si-9.2Mg, the surface of primary Si remains mostly faceted, suggesting a weaker correlation between faceting and cooling rate in this alloy. Additionally, primary Si clustering, previously observed in Al-40Si 90-106 μm droplets, is still observable in the 106-125 μm droplets of the same alloy. In contrast, Figure 5.8a shows little clustering in Al-40Si-9.2Mg 106-125 μm droplets. This indicates that chemical modification of Al-40Si using Mg has a positive impact on the microstructure by homogenizing
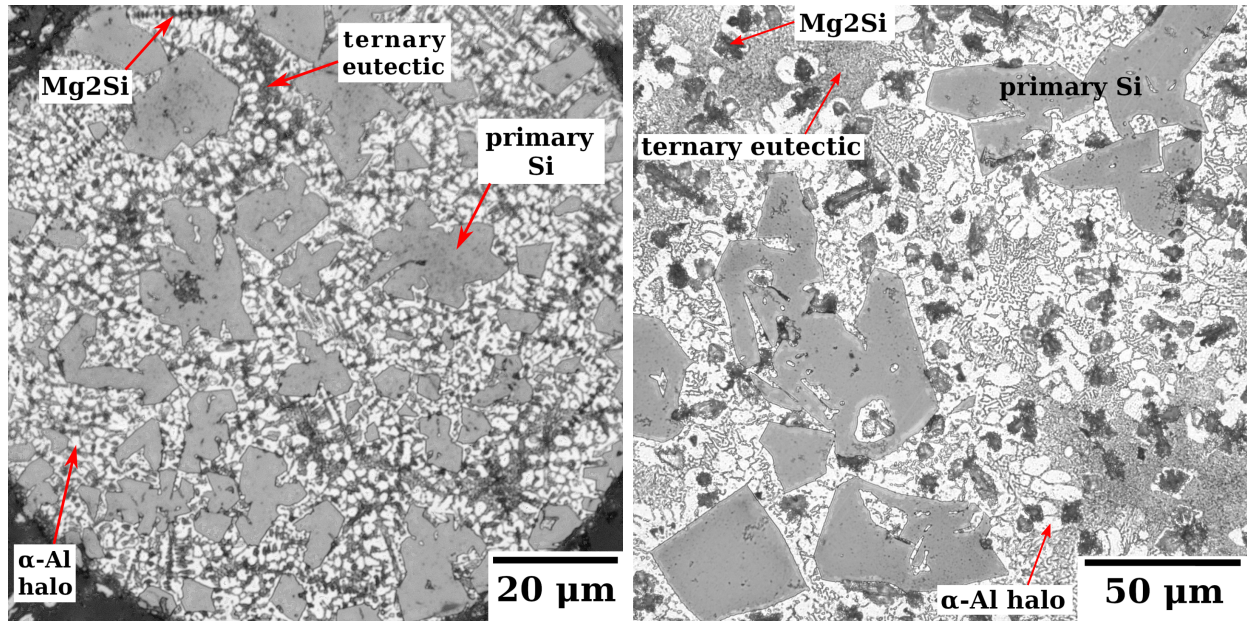
(a) 106-125 μm powder   (b) 710-850 μm powder

Figure 5.8: Microstructure of IA Al-40Si-9.2Mg cooled in He

the distribution of primary Si.

The use of Mg as a modifier in this alloy also appears to introduce a reduction in the aspect ratio of primary Si as compared to the baseline Al-40Si and Ce-modified alloys. This is most evident in large powders (such as the 710-850 μm droplet shown in Figure 5.8b). For comparison, the microstructures of 710-850 μm Al-40Si and Al-40Si-1.5Ce are reproduced in Figure 5.10. In Al-40Si and Al-40Si-1.5Ce, primary Si grains are generally elongated, while those in Al-40Si-9.2Mg are more equiaxed. This difference in aspect ratio results in a more homogeneous microstructure through a better distribution of primary Si.

When observed under higher magnifications, two forms of Mg_2Si are present in this alloy. As shown in Figure 5.11, Mg_2Si is present both in large dendrites and smaller elongated grains. From this image, it is also clear that the regions labelled Mg_2Si are really holes left by the removal of Mg_2Si during etching. The larger grains identified in Figure 5.11 as binary Mg_2Si are the same set of features identified in Figure 5.8 as Mg_2Si. Based on their size and location with respect to the rest of the microstructure, these features most likely formed during two-phase reaction that G-S identifies as forming Mg_2Si and Si. Likewise, the smaller
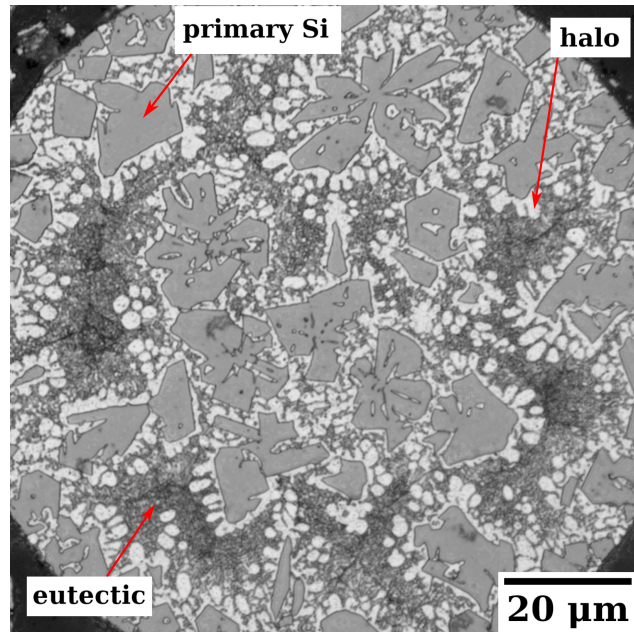
Figure 5.9: Microstructure of Al-40Si 106-125 μm droplet
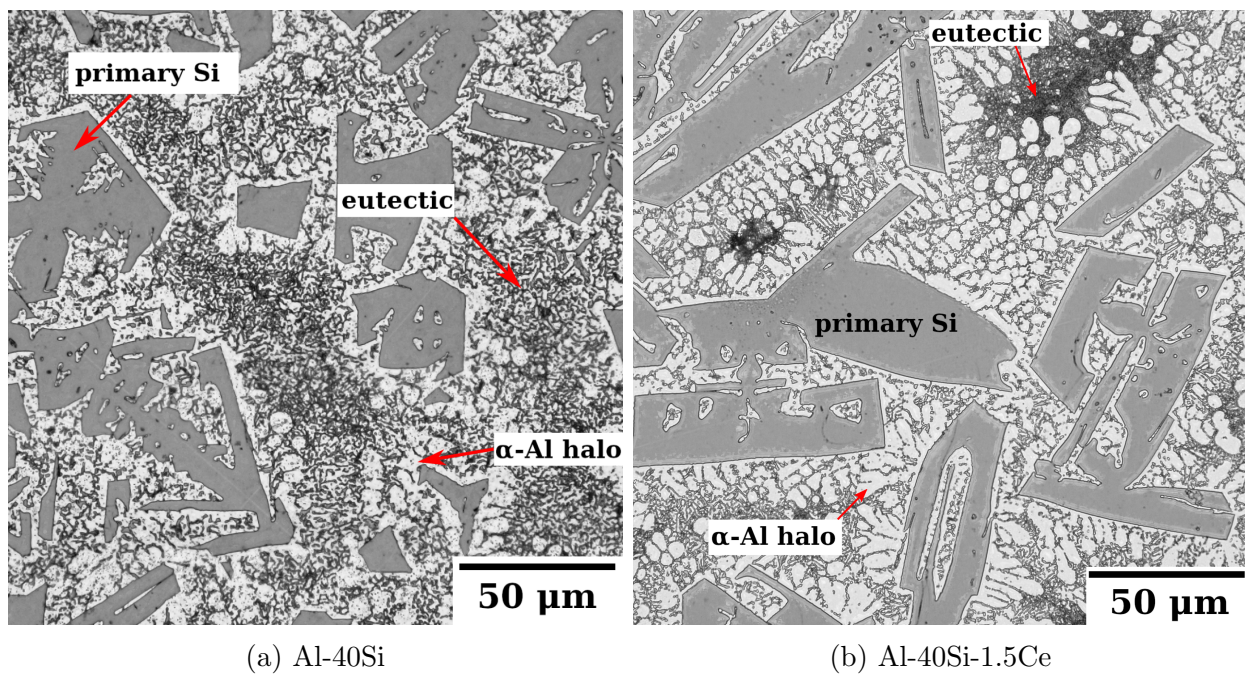
(a) Al-40Si

(b) Al-40Si-1.5Ce

Figure 5.10: Microstructure of 710-850 μm IA Al-40Si and Al-40Si-1.5Ce cooled in He

Mg$_2$Si grains seen in Figure 5.11 are most likely a product of ternary eutectic solidification.

Binary Mg$_2$Si is clasified as such due to its interaction with the rest of the microstructure. The most important characteristic of this interaction is the location of α-Al halo with respect
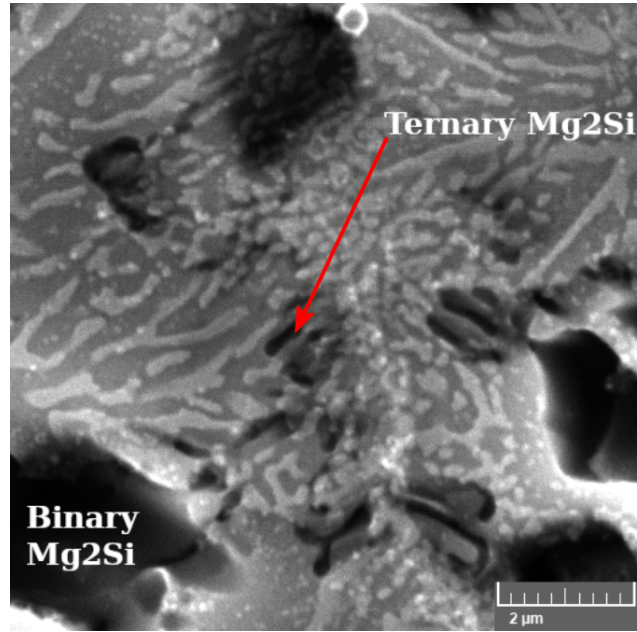
Figure 5.11: Comparison of Mg$_2$Si morphologies. 300-355 μm droplet.

to binary Mg$_2$Si. This is most evident in Figure 5.8b. In this image, a large portion of binary Mg$_2$Si are surrounded by α-Al haloes. This behaviour suggests that binary Mg$_2$Si solidified prior to the formation of the halo around it. Since, according to G-S, the two-phase reaction should form Si and Mg$_2$Si, formation of the halo as part of the two-phase reaction is unlikely. Instead, this halo most likely formed after the two-phase reaction and prior to the ternary eutectic. This sequence in solidification steps thus places the formation of the halo between the solidification of binary Mg$_2$Si and the finer ternary eutectic.

Figure 5.12 shows SEM images of the ternary eutectic in Al-40Si-9.2Mg in two powder sizes (106-125 and 810-1000 μm diameter). In contrast to Al-40Si and Al-40Si-1.5Ce, the eutectic Si morphology in this alloy does not strongly respond to changes in liquid cooling rate. In both powder sizes, the eutectic Si is fibrous + globular, suggesting this is the case for other powder sizes with average diameters between 125 and 850 μm. Additionally, eutectic Si in Figure 5.11, which shows a 300-355 μm diameter droplet, is also fibrous + globular, which further supports the limited morphology variation within the range of powder sizes analyzed.

(a) 106-125 μm powder
(b) 850-1000 μm powder
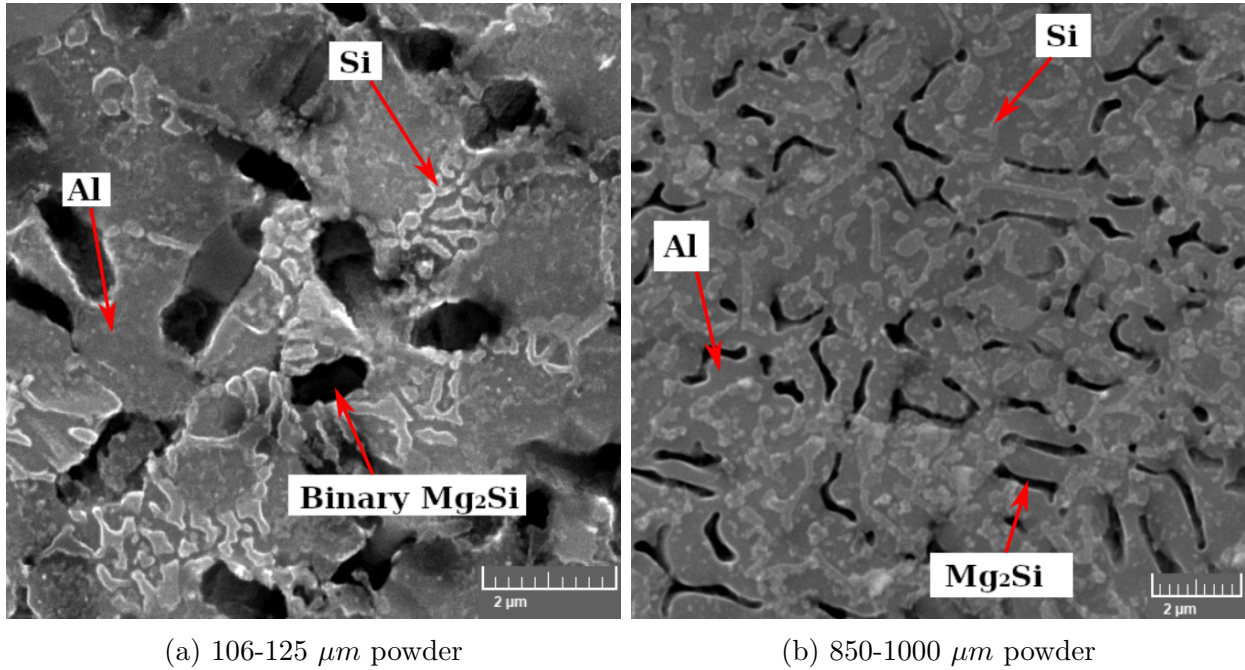
Figure 5.12: Ternary eutectic in IA Al-40Si-9.2Mg

5.2.3 Effect of RS on phase fractions

Figure 5.13 presents the experimentally determined distribution of primary Si and binary Mg$_2$Si in Al-40Si-9.2Mg as a function of cooling rate. In contrast to the measured distribution for the previous alloys, this Mg-modified alloy presents primary Si and binary Mg$_2$Si vol% that are nearly constant for all measured cooling rates. For both phases, the measured vol% is higher than that expected from G-S solidification. Measured primary Si vol% being higher than G-S suggests an undercooling of the two-phase reaction. Similarly, the larger than G-S binary Mg$_2$Si suggests an undercooling of the halo and ternary eutectic reactions.

The stable primary Si and binary Mg$_2$Si vol% mark another distinction between Al-40Si-9.2Mg and each Al-40Si and Al-40Si-1.5Ce. In each of the previous alloys, vol% of each component measured changed as a function of cooling rate. This difference indicates that phase distribution Al-40Si-9.2Mg is not very sensitive to cooling rate between 2,000 and 50,000 K/s. The reason for this change in behaviour is unclear.

The binary Mg$_2$Si curve in Figure 5.13 contains a single data point that deviates from
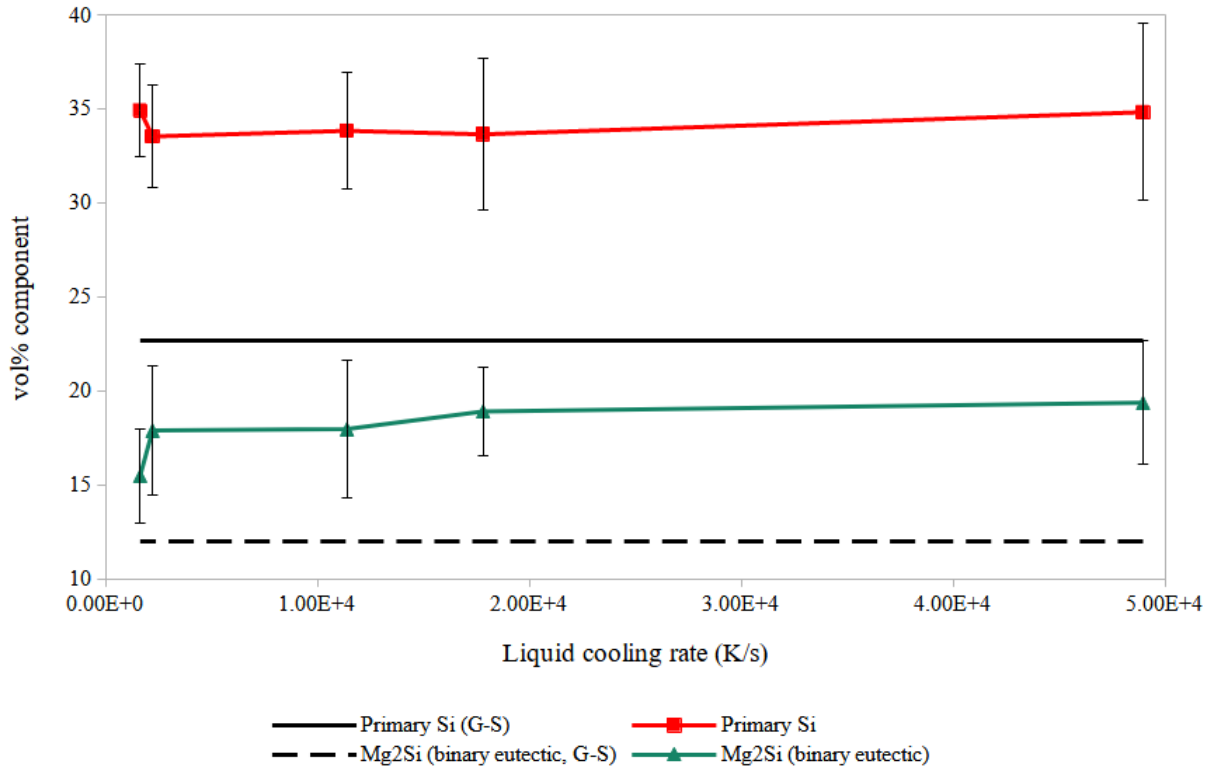
Figure 5.13: Measured microstructural distribution in IA Al-40Si-9.2Mg

the rest at 1,630 K/s. According to two-sample t-tests done to compare this value to the rest of the curve, the deviation of this point from those at 17,800 and 49,000 K/s is most likely not a product of sampling statistics. This suggests that there may be a slight increase in the binary Mg_2Si vol% in Al-40Si-9.2Mg as cooling rate increases.

Primary Si vol% measured in this alloy (33.5-35.0 vol%) is comparable to that found in Al-40Si (32.2-36.8 vol%). When combined with the homogenization of primary Si in this alloy that results from a smaller aspect ratio and decreased clustering, Al-40Si-9.2Mg can be reasonably expected to present better wear resistance than Al-40Si.

In contrast to Al-40Si and Al-40Si-1.5Ce, halo and ternary eutectic vol% were not measured for Al-40Si-9.2Mg. This is due to the difficulty of distinguishing halo and eutectic features in OM images of this alloy. In this alloy, halo dendrites are of a smaller scale than those observed in Al-40Si and Al-40Si-1.5Ce and are thus more difficult to differentiate from α-Al belonging to the eutectic structure than in the previous two alloys.

87

5.2.4 Summary

The microstructure of IA Al-40Si-9.2 Mg contains primary Si, α-Al halo, dendritic Mg$_2$Si, and a ternary eutectic comprised of fine Si and Mg$_2$Si grains embedded in an α-Al matrix. As in Al-40Si and Al-40Si-1.5Ce, the Al-rich halo in Al-40Si-9.2Mg is not an equilibrium or Gulliver-Scheil structure and indicates the metastability of this alloy. In comparison to Al-40Si, use of Mg in this alloy decreased primary Si clustering in small powders, reduced primary Si aspect ratio in large powders, and led to a weaker correlation between cooling rate and primary Si surface faceting. The observed changes associated with the Mg in this alloy indicate that Al-40Si-9.2Mg is likely to present better wear resistance than Al-40Si due to the more homogeneous distribution of primary Si while maintaining a similar primary Si vol%.

5.3 Al-40Si-2.75Fe-2.75Mn-1.5Sc

This section presents the microstructure and primary Si distribution in an IA Al-40Si-2.75Fe-2.75Mn-1.5Sc alloy. The observed microstructure is used to identify some of the phases formed during solidification. The measured distribution of primary Si is compared to the Gulliver-Scheil solidification path for this alloy and used as a baseline to assess the deviation of the IA solidification path from local equilibrium conditions.

5.3.1 Gulliver-Scheil solidification path

Figure 5.14 shows the Gulliver-Scheil (G-S) solidification path of Al-40Si-2.75Fe-2.75Mn-1.5Sc, which is based on local equilibrium conditions. This diagram was produced in Thermo-Calc 2017a software using the TTAL7 database (version 7.1). Table 5.6 contains a breakdown of the reactions shown in Figure 5.14, including phase distribution, wt% formed by each reaction, and start temperature. The last two reactions, both producing the same quaternary eutectic, are treated differently by G-S due to the contribution of the first of them in enrich-

ing the remaining liquid with solute. In contrast, the second reaction only produces solid components. Given the subtle difference, which is unlikely to be identifiable when observing the resulting microstructure, these reactions are treated as a single one in this document.
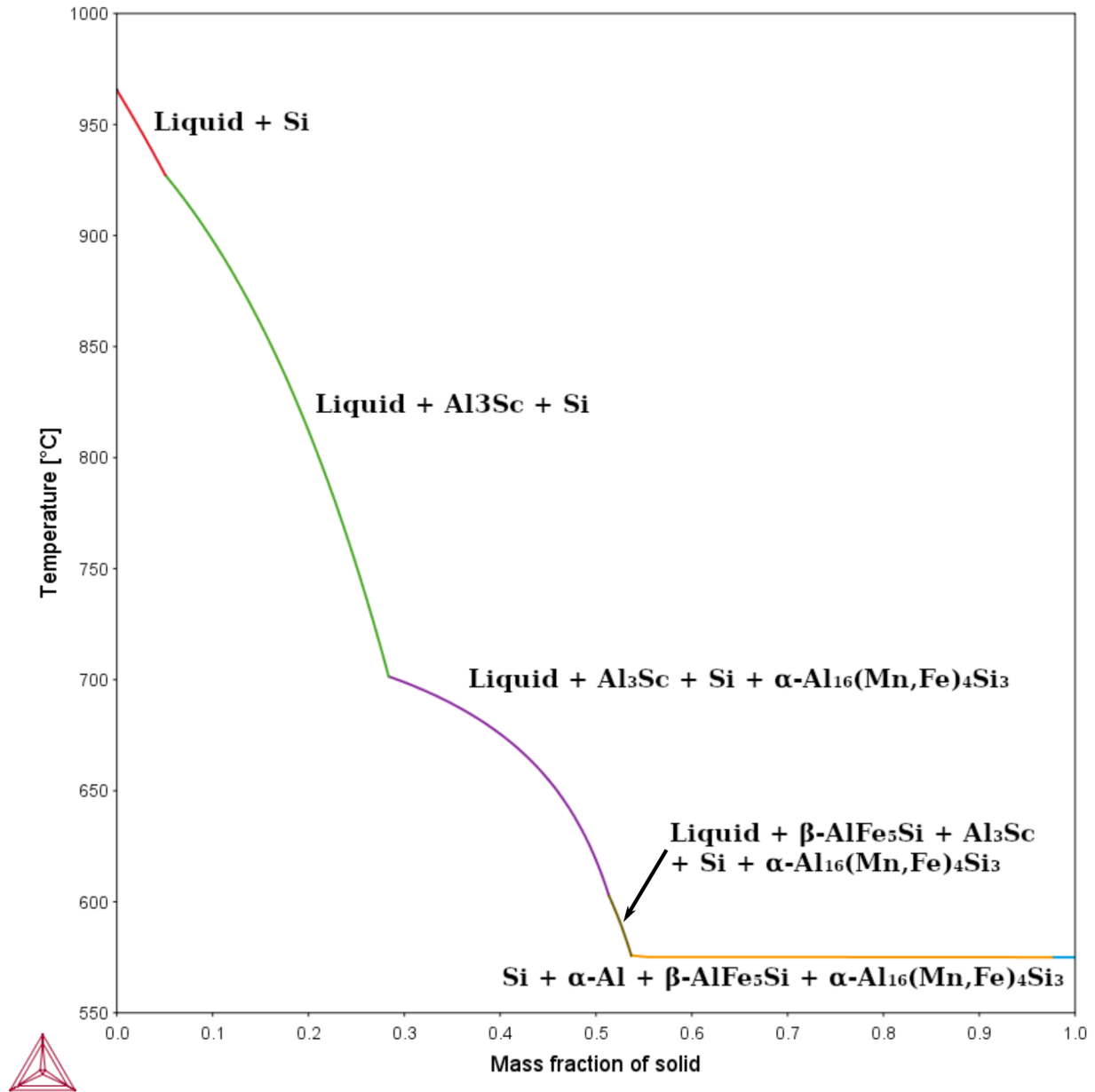
Figure 5.14: G-S solidification diagram for Al-40Si-2.75Fe-2.75Mn-1.5Sc

Table 5.6: G-S Microstructural Distribution for Al-40Si-2.75Fe-2.75Mn-1.5Sc

Reaction	wt%	Phases	Start T °
Primary Si	5.1	Si	965.5
Two-phase reaction	23.3	Si, Al$_3$Sc	927.2
Three-phase reaction	2.5	Si, Al$_3$Sc, α-Al$_{16}$(Fe,Mn)$_4$Si$_3$	701.5
Four-phase reaction	2.5	Si, Al$_3$Sc, α-Al$_{16}$(Fe,Mn)$_4$Si$_3$ β-Al$_5$FeSi	602.8
Quaternary eutectics	46.3	Si, α-Al$_{16}$(Fe,Mn)$_4$Si$_3$, β-Al$_5$FeSi, α-Al	575.1

5.3.2 Microstructure

Figure 5.15 presents the microstructure of Al-40Si-2.75Fe-2.75Mn-1.5Sc as solidified under a high and a low cooling rate. Figure 5.15a shows the microstructure of a 106-126 μm droplet, which experienced an average liquid cooling rate of 46,400 K/s. Figure 5.15b shows the microstructure of a 710-850μm droplet, which experienced an average liquid cooling rate of 2,250 K/s. In both microstructures, primary Si, an α-Al halo, and a eutectic are visible. Additionally, the coarser microstructure (Figure 5.15b) also shows intermetallic grains.

(a) 106-125 μm powder (b) 710-850 μm powder
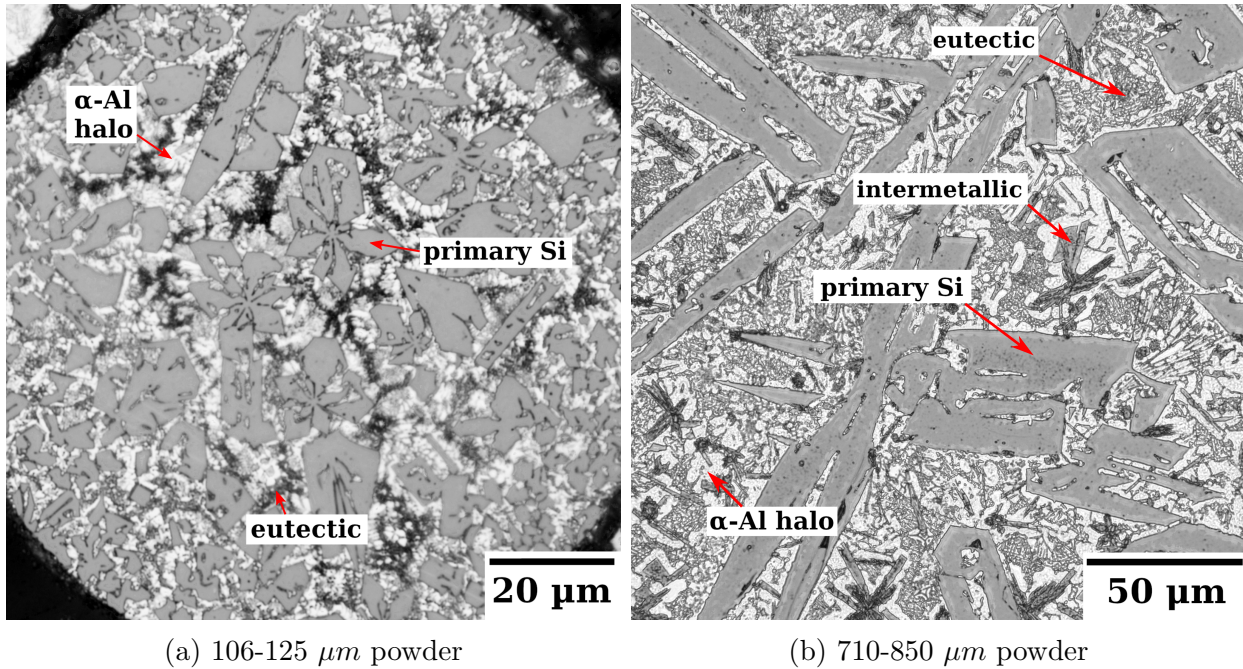
Figure 5.15: Microstructure of IA Al-40Si-2.75Fe-2.75Mn-1.5Sc

Comparing these microstructures side-by-side reveals the effect of cooling rate on this alloy. Just as with Al-40Si, significant refinement can be attributed to increasing cooling rate. Additionally, the larger powder contains more elongated primary Si, while in the smaller one primary Si has a smaller aspect ratio and mostly takes on a star-like morphology. As observed in Al-40Si-9.2Mg, Al-40Si-2.75Fe-2.75Mn-1.5Sc shows a weaker correlation between liquid cooling rate and primary Si surface faceting. This is evident from the sharp primary Si/matrix interfaces present in both 106-125 μm and 710-850 μm powders. As with the rest of the chemically-modified alloys, Al-40Si-2.75Fe-2.75Mn-1.5Sc shows significantly less primary Si clustering than Al-40Si in the smallest powders tested.

Phase distribution within the eutectic of this alloy is significantly more complex than for the other alloys presented in this work. A breakdown of the XRD results, SEM images, and EDX scans obtained for this alloy is presented in Appendix D.

5.3.3 Effect of RS on primary Si phase fraction

Figure 5.16 shows the evolution of primary Si vol% as a function of cooling rate. In contrast to Al-40Si, for which the α-Al halo and eutectic were quantified, the microstructure of this alloy is too complex to be appropriately quantified via OM imaging. Likewise, due to a slight clustering tendency observed in Figure 5.15a, SEM imaging and higher magnifications were not used, as this approach was likely to produce inaccurate results. For these reasons, only primary Si vol% was quantified for this alloy.

Figure 5.16 shows a slight increase in primary Si vol% as cooling rate increases, although this trend appears to break down toward the right side of the diagram. Two-sample t-tests were performed to assess the statistical significance of the variation between individual data points. Based on a confidence level of 95%, the primary Si vol% values obtained for 2,250 K/s and 4,200 K/s were found to deviate sufficiently from the value obtained at 17,000 K/s for the vol% of these samples to be considered different from each other. Additionally, the deviation in primary Si vol% values obtained for 11,100 K/s, 17,000 K/s, and 46,400 K/s is
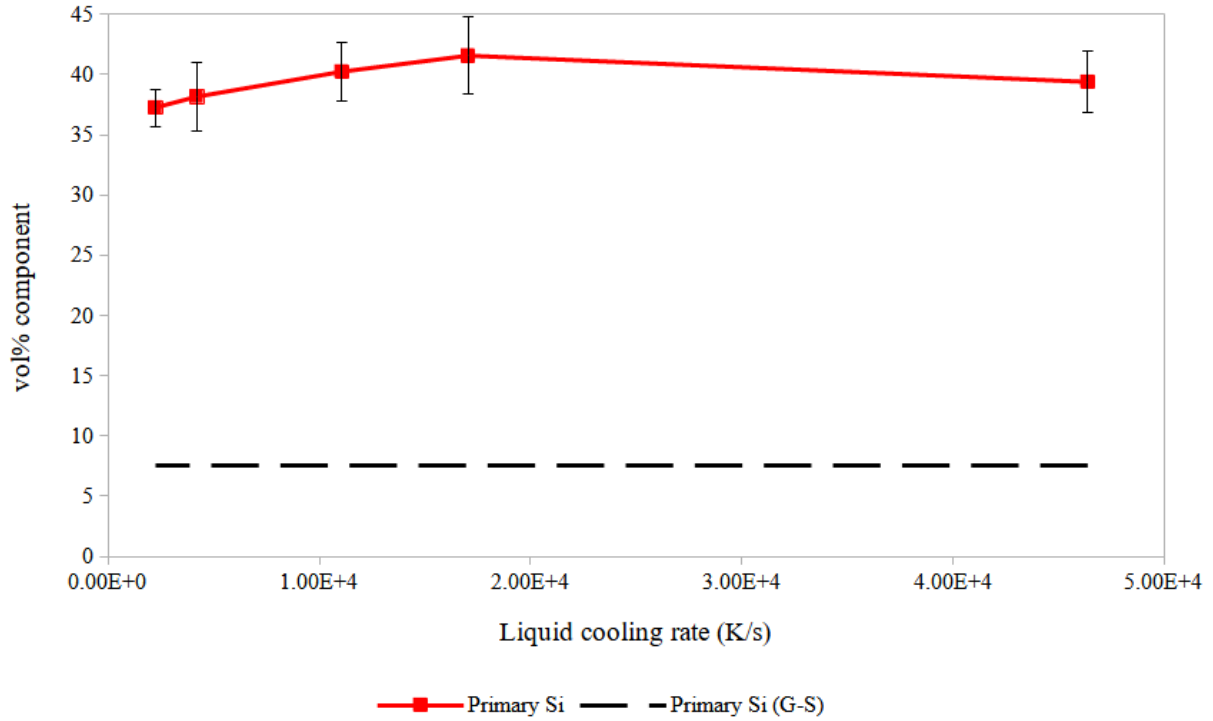
Figure 5.16: Measured primary Si in IA Al-40Si-2.75Fe-2.75Mn-1.5Sc

not large enough to be considered statistically significant. These results suggest the change in primary Si vol% as a function of cooling rate in this alloy follows a similar trend to that seen in Al-40Si and Al-40Si-1.5Ce, where primary Si vol% increases with increasing cooling rate in large powders and plateaus in small ones.

The difference between the G-S and measured primary Si vol% is particularly large in this alloy. Measured primary Si vol% is consistently higher than the value expected from the G-S solidification model. This difference ranges between 31 and 35.5 vol% across the range of tested cooling rates. Of the other alloys explored in this work, Al-40Si-9.2Mg showed the next highest difference between these measures (10 to 12 vol%). In the binary Al-40Si on which this alloy is based, this difference ranges between 0 and 2.5 vol%. This large deviation from G-S suggests the solidification path of this alloy occured further away from equilibrium than any of the other alloys tested.

92

5.3.4 Summary

The microstructure of Al-40Si-2.75Fe-2.75Mn-1.5Sc contains primary Si, α-Al halo, and a eutectic structure that contains non-equilibrium phases. As with the alloys previously discussed, the presence of an α-Al halo in this alloy is not expected based on the phase diagram and Gulliver-Scheil solidification paths, suggesting a large deviation from equilibrium conditions. In comparison to Al-40Si, the use of Fe/Mn/Sc as chemical modifiers reduce primary Si clustering in small powders. This alloy also presents a weaker correlation between cooling rate and primary Si surface faceting than Al-40Si. The deviation of primary Si vol% from Gulliver-Scheil values was higher for Al-40Si-2.75Fe-2.75Mn-1.5Sc than any other alloy in this work.

5.4   Summary of chemically modified alloys

The microstructure of all studied alloys contains primary Si, an Al-rich halo, and a eutectic structure. Primary Si clustering was observed in the smallest Al-40Si powders analyzed. Alloying with each Ce, Mg, and Fe/Mn/Sc reduced primary Si clustering even for the smallest powders observed. Al-40Si-1.5Ce presents a strong correlation between liquid cooling rate and primary Si surface faceting (similar to that in Al-40Si). In Al-40Si-9.2Mg and Al-40Si-2.75Fe-2.75Mn-1.5Sc, primary Si grains remain faceted at all cooling rates tested. The degree of faceting observed is comparable to that in the largest Al-40Si and Al-40Si-1.5Ce powders. Primary Si in Al-40Si-1.5Ce and Al-40Si-2.75Fe-2.75Mn-1.5Sc becomes less elongated as cooling rate increases; this behaviour is consistent with that observed in Al-40Si. In Al-40Si-9.2Mg, primary Si aspect ratio does not change as a function of cooling rate. In all alloys, measured primary Si vol% is larger than G-S. This indicates an undercooling of the reactions that take place after primary Si solidification. Similarly to Al-40Si, primary Si vol% is a weak function of liquid cooling rate in Al-40Si-1.5Ce and Al-40Si-2.75Fe-2.75Mn-1.5Sc. In Al-40Si-9.2Mg, primary Si vol% is not significantly influenced by liquid cooling rate.

Chapter 6

Conclusions and Future Work

This work explored the use of three sets of alloying elements (Ce, Mg, and a mixed Fe/Mn/Sc) as modification agents for the morphology of primary and eutectic Si in a rapidly solidified (RS) Al-40Si alloy. These modifiers were used both to assess the effects of chemical modification on the microstructure of RS Al-40Si produced under a wide range of liquid cooling rates (2,000 to 70,000 K/s), and to observe the effect of RS on Al-40Si-1.5Ce, Al-40Si-9.2Mg, and Al-40Si-2.75Fe-2.75Mn-1.5Sc. The effects of the interaction between RS and chemical modification presented can be summarized in two categories: changes to primary Si distribution and changes to primary Si morphology.

Changes to the distribution of primary Si result from variations in the extent of primary Si clustering and the aspect ratio of primary Si. No primary Si clustering is observed in large powder sizes, but this behaviour is increasingly more prevalent as powder size decreases, especially in Al-40Si. In Al-40Si-9.2Mg and Al-40Si-2.75Fe-2.75Mn-1.5Sc, the increase in clustering as powder size decreases is still observed, but the smallest powders produced for these alloys do not show clustering as severe as that in Al-40Si powders of the same size. In Al-40Si-1.5Ce, no clustering behaviour is observed. These results suggest that the use of any of the chemical modifiers tested in this work reduce the primary Si clustering tendency introduced by increasing cooling rate as observed in Al-40Si. Primary Si aspect

ratio is affected both by varying cooling rate and by the use of Mg in the alloy. In Al-40Si, Al-40Si-1.5Ce, and Al-40Si-2.75-2.75Mn-1.5Sc, primary Si grains shift from being mostly elongated (usually presenting some plate-like features) to a more equiaxed shape (star-like and octahedral morphologies) as cooling rate increases. Al-40Si-9.2Mg is distinct from the other alloys in that the primary Si grains seen in this alloy consistently present a small aspect ratio, akin to that seen in the smallest powder sizes of the other alloys, and which does not appear to be affected by cooling rate. The reduction in primary Si clustering and aspect ratio result in a more homogeneous distribution of the microstructure. This effect is likely to improve the composite effect that Si and α-Al have on the alloy's properties, particularly in the case of wear resistance.

Al-40Si and Al-40Si-1.5Ce present a strong correlation between increasing cooling rate and a decrease in the faceting of the primary Si surface. The changes in the shape of the primary Si surface introduced by this effect are likely to reduce stress concentration at this location and have the potential to enhance the alloy's toughness for small powder sizes. In contrast, Al-40Si-9.2Mg and Al-40Si-2.75Fe-2.75Mn-1.5Sc do not show a strong correlation between cooling rate and primary Si faceting. In these alloys, primary Si grains remain faceted for all cooling rates tested, suggesting these alloys do not benefit from an improvement in toughness when processed at higher cooling rates.

Of the alloys presented in this work, Al-40Si-1.5Ce and Al-40Si-9.2Mg stand out as good candidates for further research. In particular, testing these alloys in a Laser Powder-Bed Fusion apparatus is recommended.

The qualities of Al-40Si-1.5Ce make it desirable for use in applications where similar wear resistance to that of Al-40Si and improved toughness are required. The limited primary Si clustering observed in this alloy suggests it will present better wear resistance than the binary Al-40Si alloy originally explored. Additionally, the limited primary Si surface faceting observed in small powders is likely to reduce crack initiation at the primary Si/matrix interface, thereby enhancing toughness. Finally, the presence of large amounts of α-Al halo

homogenize the microstructure (making it mostly a mix of primary Si and halo) and allows the potential of slowing crack growth (due to the ductility of α-Al).

Al-40Si-9.2Mg is promising for applications where wear resistance similar to that of Al-40Si is required. As with Al-40Si-1.5Ce, this alloy presents significantly less clustering than Al-40Si, which improves the distribution of primary Si and is likely to lead to an improvement in wear resistance when compared to Al-40Si. The formation of Mg_2Si as a non-faceted phase suggests this phase may not significantly impact ductility of the alloy. However, with the Al content in Al-40Si-9.2Mg being lower than in Al-40Si, the former alloy contains less of its most ductile phase (α-Al). The resulting decrease in ductility is unclear, but should be considered when studying Al-4Si-9.2Mg in Laser Powder-Bed Fusion.

Bibliography

[1] M. Warmuzek, "Introduction to Aluminum-Silicon Casting Alloys," in *Aluminum-Silicon Casting Alloys Atlas of Micrographs*, ch. 1, pp. 1–9, Materials Park, OH: ASM International, 2004.

[2] "Al (Aluminum) Binary Alloy Phase Diagrams," in *Alloy Phase Diagrams ASM Handbooks* (H. Okamoto, M. E. Schlesinger, and E. M. Mueller, eds.), vol. 3, pp. 113–139, ASM International, 10 ed., apr 2016.

[3] V. Prabhu and V. Narayan, "Review of Microstructure Evolution in Hypereutectic Al – Si Alloys and its Effect on Wear Properties," *Transactions of the Indian Institute of Metals*, vol. 67, no. 1, pp. 1–18, 2014.

[4] B. K. Prasad, K. Venkateswarlu, O. P. Modi, A. K. Jha, S. Das, R. Dasgupta, and A. H. Yegneswaran, "Sliding wear behavior of some Al-Si alloys: Role of shape and size of si particles and test conditions," *Metallurgical and Materials Transactions A: Physical Metallurgy and Materials Science*, vol. 29, no. 11, pp. 2747–2752, 1998.

[5] C. L. Xu, A. Y. F. Yang, A. H. Y. Wang, and A. Q. C. Jiang, "Effects of modification and heat-treatment on the abrasive wear behavior of hypereutectic Al-Si alloys," *Journal of Materials Science*, vol. 42, no. 15, pp. 6331–6338, 2007.

[6] A. Mazahery and M. O. Shabani, "Modification mechanism and microstructural characteristics of eutectic si in casting Al-Si Alloys: A review on experimental and numerical studies," *JOM*, vol. 66, no. 5, pp. 726–738, 2014.

[7] K. Fujiwara, H. Fukuda, N. Usami, K. Nakajima, and S. Uda, "Growth mechanism of the Si <110>faceted dendrite," *Physical Review B*, vol. 81, no. 22, 2010.

[8] D. R. Hamilton and R. G. Seidensticker, "Growth Mechanisms of Germanium Dendrites: Kinetics and the Nonisothermal Interface," *Journal of Applied Physics*, vol. 34, no. 5, pp. 1450–1460, 1963.

[9] Y. Pei and J. De Hosson, "Five-fold branched Si particles in laser clad AlSi functionally graded materials," *Acta Materialia*, vol. 49, pp. 561–571, feb 2001.

[10] K. Kobayashi and L. Hogan, "Fivefold twinned silicon crystals grown in an Al-16 wt% Si melt," *Philosophical Magazine A*, vol. 40, no. 3, pp. 399–407, 1979.

[11] S. Ino, "Stability of Multiply-Twinned Particles," *Journal of the Physical Society of Japan*, vol. 27, no. 4, pp. 941–953, 1969.

[12] J. D. Bernal, "A geometrical approach to the structure of liquids," *Nature*, vol. 183, no. 3, pp. 141–147, 1959.

[13] K. Kobayashi, P. Shingu, and R. Ozaki, "Crystal growth of the primary silicon in an Al-16wt% Si alloy," *Journal of Materials Science*, vol. 10, no. 2, pp. 290–299, 1975.

[14] R. P. Liu, D. M. Herlach, M. Vandyoussefi, and A. L. Greer, "Undercooling and solidification of Al-50 at. pct Si alloy by electromagnetic levitation," *Metallurgical and Materials Transactions A: Physical Metallurgy and Materials Science*, vol. 35 A, no. 2, pp. 607–612, 2004.

[15] L. L. Ge, R. P. Liu, G. Li, M. Z. Ma, and W. K. Wang, "Solidification of Al-50 at.%Si alloy in a drop tube," *Materials Science and Engineering A*, vol. 385, no. 1-2, pp. 128–132, 2004.

[16] R.-Y. Wang, W.-H. Lu, and L. M. Hogan, "Growth morphology of primary silicon in cast Al-Si alloys and the mechanism of concentric growth," *Journal of Crystal Growth*, vol. 207, pp. 43–54, 1999.

[17] C. Xu, H. Wang, C. Liu, and Q. Jiang, "Growth of octahedral primary silicon in cast hypereutectic Al–Si alloys," *Journal of Crystal Growth*, vol. 291, pp. 540–547, jun 2006.

[18] W. Hearn, A. A. Bogno, J. Spinelli, J. Valloton, and H. Henein, "Microstructure Solidification Maps for Al-10 Wt Pct Si Alloys," *Metallurgical and Materials Transactions A: Physical Metallurgy and Materials Science*, vol. 50, pp. 1333–1345, mar 2019.

[19] B. Sundquist, R. Bruscato, and L. Mondolfo, "Structure of Eutectics," *Journal of the Institute of Metals*, vol. 91, pp. 204–208, 1963.

[20] A. Kofler, "Precipitation anomalies during isothermal crystallization from undercooled, binary organic melts," *Journal of the Australian Institute of Metals*, vol. 10, pp. 132–139, 1965.

[21] M. F. X. Gigliotti, G. A. Colligan, and G. L. F. Powell, "Halo Formation in Eutectic Alloy Systems," *Metallurgical Transactions*, vol. 1, no. 4, pp. 891–897, 1970.

[22] E. J. Lavernia and T. S. Srivatsan, "The rapid solidification processing of materials: Science, principles, technology, advances, and applications," *Journal of Materials Science*, vol. 45, no. 2, pp. 287–325, 2010.

[23] A. Aversa, G. Marchese, A. Saboori, E. Bassini, D. Manfredi, S. Biamino, D. Ugues, P. Fino, and M. Lombardi, "New Aluminum Alloys Specifically Designed for Laser Powder Bed Fusion: A Review," *Materials*, vol. 12, no. 7, p. 1007, 2019.

[24] N. Kang and M. El Mansori, "A new insight on induced-tribological behaviour of hypereutectic Al-Si alloys manufactured by selective laser melting," *Tribology International*, 2019.

[25] D. D. Gu, W. Meiners, K. Wissenbach, . R. Poprawe, and R. Poprawe, "Laser additive manufacturing of metallic components: materials, processes and mechanisms," *International Materials Reviews*, vol. 57, no. 3, pp. 133–164, 2012.

[26] W. E. Frazier, "Metal Additive Manufacturing: A Review," *Journal of Materials Engineering and Performance*, vol. 23, no. 6, pp. 1917–1928, 2014.

[27] D. M. Stefanescu, *Science and Engineering of Casting Solidification*. New York: Springer, 2nd ed., 2008.

[28] C. R. Ho and B. Cantor, "Heterogeneous nucleation of solidification of Si in Al-Si and Al-Si-P alloys," *Acta Metallurgica Et Materialia*, vol. 43, no. 8, pp. 3231–3246, 1995.

[29] Y. Wu, S. Wang, H. Li, and X. Liu, "A new technique to modify hypereutectic Al-24%Si alloys by a Si-P master alloy," *Journal of Alloys and Compounds*, vol. 477, pp. 139–144, may 2009.

[30] P. Crosley and L. Mondolfo, "The modification of Aluminum-Silicon alloys," *Modern Castings*, vol. 89, 1966.

[31] R. Pohanish and S. Greene, *Wiley Guide to Chemical Incompatibilities*. John Wiley Sons, 3rd ed., 2009.

[32] R. Lewis, *Sax's Dangerous Properties of Industrial Materials*. John Wiley Sons, 12th ed., 2012.

[33] S.-Z. Lu and A. Hellawell, "The Mechanism of Silicon Modification in Aluminum-Silicon Alloys: Impurity Induced Twinning," *Metallurgical Transactions A*, vol. 18, pp. 1721–1733, 1987.

[34] M. G. Day, "Primary Silicon Spherulites in Aluminum-Silicon Alloys," *Nature*, vol. 219, pp. 1357–1358, sep 1968.

[35] J. H. Li, M. Albu, F. Hofer, and P. Schumacher, "Solute adsorption and entrapment during eutectic Si growth in Al-Si-based alloys," *Acta Materialia*, vol. 83, pp. 187–202, 2015.

[36] S.-Z. Lu and A. Hellawell, "Growth mechanisms of silicon in Al-Si alloys," *Journal of Crystal Growth*, vol. 73, pp. 316–328, nov 1985.

[37] K. Nogita, S. D. Mcdonald, and A. K. Dahle, "Eutectic Modification of Al-Si Alloys with Rare Earth Metals," *Materials Transactions*, vol. 45, no. 2, pp. 323–326, 2004.

[38] J. Chang, I. Moon, and C. Choi, "Refinement of cast microstructure of hypereutectic Al-Si alloys through the addition of rare earth metals," *Journal of Materials Science*, vol. 33, no. 20, pp. 5015–5023, 1998.

[39] K. Nogita, J. Drennan, and A. K. Dahle, "Evaluation of Silicon Twinning in Hypo-Eutectic Al-Si Alloys," *Materials Transactions*, vol. 44, no. 4, pp. 625–628, 2003.

[40] J. Y. Chang and H. S. Ko, "Twin probability of eutectic Si in rare earth modified Al-7wt%Si alloy," *Journal of Materials Science Letters*, vol. 19, pp. 197–199, 2000.

[41] Q. Li, B. Li, J. Li, Y. Zhu, and T. Xia, "Effect of yttrium addition on the microstructures and mechanical properties of hypereutectic Al-20Si alloy," *Materials Science and Engineering A*, vol. 722, pp. 47–57, 2018.

[42] Q. Li, J. Li, B. Li, Y. Zhu, D. Liu, Y. Lan, and S. Wang, "Mechanical Properties and Microstructural Evolution of Yb-Modified Al-20%Si Alloy," *Journal of Materials Engineering and Performance*, vol. 27, pp. 3498–3507, 2018.

[43] S. Kores, M. Voncina, B. Kosec, P. Mrvar, and J. Medved, "Effect of cerium additions on the AlSi17 casting alloys," *Materials and Technology*, vol. 44, no. 3, pp. 137–140, 2010.

[44] J. Y. Chang, G. H. Kim, I. G. Moon, and C. S. Choi, "Rare earth concentration in the primary Si crystal in rare earth added Al-21wt.%Si alloy," *Scripta Materialia*, vol. 39, no. 3, pp. 307–314, 1998.

[45] J. Andersson, T. Helander, L. Hoglund, P. Shi, and B. Sundman, "Thermo-Calc Dictra, Computational Tools for Materials Science," *Calphad*, vol. 26, pp. 273–312, 2002.

[46] R. Mitra, "Phase equilibria and structure," in *Structural intermetallics and intermetallic matrix composites*, ch. 1, pp. 1–24, Boca Raton: CRC Press, 2015.

[47] H. Okamoto, M. E. Schlesinger, and E. M. Mueller, eds., *Mg (Magnesium) Binary Alloy Phase Diagrams*, vol. 3. ASM International, apr 2016.

[48] S. Takeuchi, T. Hashimoto, and K. Suzuki, "Plastic deformation of Mg 2Si with the Cl structure," *Intermetallics*, vol. 4, pp. S147–S150, 1996.

[49] A. Li, X.-P. Zhao, H.-Y. Huang, Y. Ma, L. Gao, Y.-J. Su, and P. Qian, "Fine-tuning the ductile-brittle transition temperature of Mg2Si intermetallic compound via Al doping," *International Journal of Minerals, Metallurgy and Materials*, vol. 26, no. 4, p. 507, 2019.

[50] G. H. Li, H. S. Gill, and R. A. Varin, "Magnesium Silicide Intermetallic Alloys," *Metallurgical Transactions A*, vol. 24, no. 11, pp. 2383–2391, 1993.

[51] "Mn3Si2Al15 (Mn4Al16Si3) Crystal Structure: Datasheet from "PAULING FILE Multinaries Edition – 2012" in SpringerMaterials (https://materials.springer.com/isp/crystallographic/docs/sd$_0$302718)."

[52] A. Mandal and M. M. Makhlouf, "Chemical modification of morphology of Mg2Si phase in hypereutectic aluminium-silicon-magnesium alloys," *International Journal of Cast Metals Research*, vol. 23, no. 5, pp. 303–309, 2010.

[53] D. Wang, H. Zhang, C. Guo, H. Wu, and J. Cui, "Effect of cooling rate on growth and transformation of primary Mg 2 Si in Al-Mg 2 Si in situ composites," *Journal of Materials Research*, vol. 33, no. 20, pp. 3458–3460, 2018.

[54] C. Li, Y. Y. Wu, H. Li, and X. F. Liu, "Morphological evolution and growth mechanism of primary Mg 2 Si phase in Al-Mg 2 Si alloys," *Acta Materialia*, vol. 59, pp. 1058–1067, 2011.

[55] J. J. Kim, D. H. Kim, K. S. Shin, and N. J. Kim, "Modification of Mg2Si morphology in squeze cast Mg-Al-Zn-Si alloys by Ca or P addition," *Scripta Materialia*, vol. 41, no. 3, pp. 333–340, 1999.

[56] T. Liu, Y. Li, Y. Ren, and W. Wang, "The microstructure and mechanical characterization of Al-30%Mg 2 Si composite with Y inoculation addition," *Materials Research Express*, vol. 5, 2018.

[57] Y.-Z. Lü, Q.-D. Wang, X.-Q. Zeng, W.-J. Ding, and Y.-P. Zhu, "Effects of silicon on microstructure, fluidity, mechanical properties, and fracture behaviour of Mg–6Al alloy," *Materials Science and Technology*, vol. 17, no. 2, pp. 207–214, 2001.

[58] K. H. Kumar, N. Chakraborti, H. Lukas, O. Bodak, and L. Rokhlin, "Al-Mg-Si Ternary Phase Diagram Evaluation," in *MSI Eureka* (G. Effenberg, ed.), Stuttgart: MSI, Materials Science International Services GmbH, 2004.

[59] D. Shimosaka, S. Kumai, F. Casarotto, and S. Watanabe, "Effect of Cooling Rates during Solidification of Al-5.5%Mg-2.3%Si-0.6%Mn and Al-13%Mg 2 Si Pseudo-Binary Alloys on Their Secondary-Particle Morphology and Tear Toughness," *Materials Transactions*, vol. 52, no. 5, pp. 920–927, 2011.

[60] X. Zhu, H. Yang, X. Dong, and S. Ji, "The effects of varying Mg and Si levels on the microstructural inhomogeneity and eutectic Mg 2 Si morphology in die-cast Al-Mg-Si alloys," *Journal of Materials Science*, vol. 54, pp. 5773–5787, 2019.

[61] A. Mandal and M. Acharya, "Effect of Strontium and Misch Metal on Al–14Si–3Mg Alloy," *Transactions of the Indian Institute of Metals*, vol. 68, pp. 1181–1185, dec 2015.

[62] M.-b. Yang, F.-s. Pan, J. Shen, and L. Bai, "Comparison of Sb and Sr on modification and refinement of Mg2Si phase in AZ61-0.7Si magnesium alloy," *Transactions of Nonferrous Metals Society of China (English Edition)*, vol. 19, pp. 287–292, apr 2009.

[63] G. Y. Yuan, Z. L. Liu, Q. D. Wang, and W. J. Ding, "Microstructure refinement of Mg-Al-Zn-Si alloys," *Materials Letters*, vol. 56, no. 1-2, pp. 53–58, 2002.

[64] T. Gao, K. Hu, L. Wang, B. Zhang, and X. Liu, "Morphological evolution and strengthening behavior of α-Al(Fe,Mn)Si in Al–6Si–2Fe–xMn alloys," *Results in Physics*, vol. 7, pp. 1051–1054, 2017.

[65] Q. Li, Y. Zhu, B. Li, S. Zhao, C. Wang, Y. Lan, and Y. Zhang, "Influences of Al–20Si–2.5Fe–2Mn Master Alloy Additions on the Microstructure and Mechanical Properties of Hypereutectic Al–20Si Alloys," *International Journal of Metalcasting*, vol. 14, pp. 409–422, aug 2019.

[66] R. Podprocká, D. Bolibruchová, and M. Chalupová, "Reducing the negative of the iron in the alloy based on Al-Si-Mg by manganese," *Archives of Foundry Engineering*, vol. 17, pp. 212–216, jun 2017.

[67] Z. Zhang, H. Tezuka, E. Kobayashi, and T. Sato, "Effects of the Mn/Fe Ratio and Cooling Rate on the Modification of Fe Intermetallic Compounds in Cast A356 Based Alloy with Different Fe Contents," *Materials Transactions*, vol. 54, no. 8, pp. 1484–1490, 2013.

[68] W. Zhang, Y. Liu, J. Yang, J. Dang, H. Xu, and Z. Du, "Effects of Sc content on the microstructure of As-Cast Al-7 wt.% Si alloys," *Materials Characterization*, vol. 66, pp. 104–110, 2012.

[69] H. Henein, "Single fluid atomization through the application of impulses to a melt," *Materials Science and Engineering A*, vol. 326, no. 1, pp. 92–100, 2002.

[70] ASM International, *Alloy Phase Diagrams ASM Handbooks.* ASM International, apr 2016.

[71] ASTM International, "Designation: E11-20 Standard Specification for Woven Wire Test Sieve Cloth and Test Sieves," tech. rep., ASTM International, West Conshohocken, PA, 2020.

[72] J. Wiskel, H. Henein, and E. Maire, "Solidification Study of Aluminum Alloys using Impulse Atomization: Part I: Heat Transfer Analysis of an Atomized Droplet," *Canadian Metallurgical Quarterly*, vol. 41, no. 1, pp. 97–110, 2002.

[73] J. Wiskel, H. Henein, and E. Maire, "Solidification Study of Aluminum Alloys using Impulse Atomization: Part II: Effect of Cooling Rate on Microstructure," *Canadian Metallurgical Quarterly*, vol. 41, no. 1, pp. 97–110, 2002.

[74] J. Wiskel and H. Henein, "No Title," in *Proceedings of Fluid Flow Phenomena in Metals Processing* (N. El-Kaddah, D. Robertson, S. Johansen, and V. Voller, eds.), (Warrendale, PA), pp. 517–524, TMS, 1999.

[75] ASTM International, "E562-19e1: Standard Test Method for Determining Volume Fraction by Systematic Manual Point Count," tech. rep., ASTM International, West Conshohocken, PA, 2019.

[76] ASTM International, "E112-13: Standard Test Methods for Determining Average Grain Size," tech. rep., ASTM International, West Conshohocken, PA, 2013.

[77] M. Gündüz, H. Kaya, E. Çadırlı, and A. Özmen, "Interflake spacings and undercoolings in Al-Si irregular eutectic alloy," *Materials Science and Engineering*, vol. 369, pp. 215–229, 2004.

[78] K. Jackson and J. Hunt, "Lamellar and Rod Eutectic Growth," *Transactions of the Metallurgical Society of AIME*, vol. 236, pp. 1129–1166, 1966.

[79] R. Grugel and W. Kurz, "Growth of interdendritic eutectic in directionally solidified Al-Si alloys," *Metallurgical Transactions A*, vol. 18, no. 6, pp. 1137–1142, 1991.

[80] A. Garcia, T. W. Clyne, and M. Prates, "Mathematical model for the unidirectional solidification of metals: II. Massive molds," *Metallurgical Transactions B*, vol. 10, no. 1, pp. 85–92, 1979.

[81] J. E. Spinelli, A. A. Bogno, and H. Henein, "Two-Zone Microstructures in Al-18Si Alloy Powders," *Metallurgical and Materials Transactions A*, vol. 49, no. 2, pp. 550–562, 2018.

[82] "Density of molten elements and representative salts," in *CRC Handbook of Chemistry and Physics* (J. Rumble, ed.), Boca Raton: CRC Press/Taylor Francis, 101 ed., 2020.

[83] W. Hearn, *The Microstructure, Morphology and Mechanical Properties of Rapidly Solidified Al-10Si Alloy.* PhD thesis, University of Alberta, 2018.

[84] P. Villars and K. Cenzual, "PAULING FILE Multinaries Edition - 2012" in Springer Materials."

[85] B. Honerlage, "Landolt-Börnstein - Group III Condensed Matter · Volume 44A: "New Data and Updates for I-VII, III-V, III-VI and IV-VI Compounds" in SpringerMaterials."

[86] B. Honerlage, "Landolt-Börnstein - Group III Condensed Matter · Volume 44C: "New Data and Updates for III-V, II-VI and I-VII Compounds" in SpringerMaterials."

[87] D. Strauch, "Landolt-Bornstein - Group III Condensed Matter · Volume 44D: "New Data and Updates for IV-IV, III-V, II-VI and I-VII Compounds, their Mixed Crystals and Diluted Magnetic Semiconductors" in SpringerMaterials."

[88] D. Strauch, "Landolt-Börnstein - Group III Condensed Matter · Volume 44E: "New Data and Updates for several III-V (including mixed crystals) and II-VI Compounds" in SpringerMaterials."

[89] U. Rossler, "Landolt-Börnstein - Group III Condensed Matter · Volume 44F: "New Data and Updates for several Semiconductors with Chalcopyrite Structure, for several II-VI Compounds and diluted magnetic IV-VI Compounds" in SpringerMaterials."

[90] D. Strauch, "Landolt-Börnstein - Group III Condensed Matter · Volume 44G: "New Data and Updates for several IIa-VI Compounds (Structural Properties, Thermal and Thermodynamic Properties, and Lattice Properties)" in SpringerMaterials."

[91] H. Koch, J.-C. Jaquet, and U. Hielscher, "Process for grain refinement of aluminum casting alloys in particular aluminum/silicon casting alloys (US005250125A)," 1993.

[92] R. Pohanish, *Sittig's Handbook of Toxic and Hazardous Chemicals and Carcinogens.* Elsevier, 7th ed. ed., 2017.

[93] Works of the Department of Health and Human Services, *14th Report on Carcinogens 2016.* U.S. Department of Health and Human Services, 2016.

[94] B. Donelly and F. Abdel-Raouf, "Statistical Tables," in *Statistics*, ch. Appendix B, Indianapolis, IN: Alpha, 3rd ed., 2016.

Appendix A

Alternative nucleation agents

The heterogeneous nucleation modification mechanism has an underlying assumption that any compound used for this purpose should have a similar lattice structure and lattice parameters as AlP and Si. Both structures have a cF8 Pearson symbol, and their lattice parameters are 0.542 nm (AlP) and 0.545 nm (Si). Table A.1 contains a list of all cF8 compounds considered as possible replacements of AlP in primary Si modification by serving as heterogeneous nucleation agents. cF4 and higher order FCC structures (cF16, cF32,...) were also considered, but these categories are, respectively, limited to pure elements, or produce crystals so large that they do not fit the lattice parameter similarity criterion.

Table A.1: Compounds considered as potential nucleation agents of primary Si
[84, 85, 86, 87, 88, 89, 90]

Compound	Lattice Parameter (nm)
AlP	0.542
AgCl	0.579 (α-AgCl)
	0.629 (γ-AgCl)
AgI	0.597-0.638 (α-AgI)
	0.649-0.667 (γ-AgI)
AlAs	0.561

Compound	Lattice Parameter (nm)
AlSb	0.532
BAs	0.473-0.481 (ZnS structure) 0.453-0.461 (NaCl structure)
BaS	0.627-0.647
BeS	0.463-0.488
BeSe	0.481-0.523
BeTe	0.503-0.567
BN	0.358-0.363
BP	0.448-0.455 (ZnS structure) 0.427-0.433 (NaCl structure)
CaO	0.469-0.495
CdS	0.577-0.595
CeSe	0.600
CuBr	0.553-0.601 (ZnS structure) 0.514-0.564 (NaCl structure)
CuCl	0.525-0.569 (ZnS structure) 0.494-0.533 (NaCl structure)
CuF	0.496 (ZnS structure) 0.461 (NaCl structure)
CuI	0.589-0.631 (ZnS structure) 0.553-600 (NaCl structure)
DyAs	0.580
GaAs	0.565
GaP	0.532
GaSb	0.598

Compound	Lattice Parameter (nm)
GdN	0.500
HgS	0.585
HgSe	0.605-0.626
HgTe	0.635-0.666
InAs	0.592
InP	0.573
KBr	0.660
LaP	0.603
LiCl	0.513
LiF	0.403
MgO	0.421
NaBr	0.595
NaF	0.463
NiO	0.418
PrBi	0.646
PuC	0.496
RbF	0.564
SiC	0.435 (3C configuration)
SrO	0.516
TbTe	0.610
UC	0.497
YbO	0.488
YN	0.487
ZnSe	0.554-0.579 (ZnS structure) 0.516-0.532 (NaCl structure)

Compound	Lattice Parameter (nm)
ZnTe	0.600-0.623 (ZnS structure)
	0.575 (NaCl structure)
ZrO	0.462

To narrow down the list of cF8 compounds, their lattice parameters were compared to that of InP (0.573 nm). Selection of this benchmark is based on the known feasibility of Si modification by this compound, as outlined in US Patent No. 5250125A [91]. This document identifies GaP and InP as effective chemical modifiers of Al-Si alloys. While the modification mechanism is not outlined outright, both compounds form cF8 structures and have similar lattice parameters to Si, at 0.532 and 0.573 nm, respectively. Based on this, it is assumed that these compounds serve as viable sites for heterogeneous nucleation of primary Si, and their lattice parameters can thus be used to determine a range of lattice parameters that could work for this purpose. Of the two compounds, InP deviates the most from the lattice parameter of Si, by 5.1%. Based on this value, cF8 compounds with lattice parameters between 0.517 and 0.573 nm are considered plausible heterogeneous nucleation sites for Si. Table A.2 lists the compounds presented in Table A.1 that fit this lattice parameter criterion.

Table A.2: cF8 compounds of appropriate size

Compound	Lattice parameter (nm)	Melting T (°C)
AlAs	0.561	1740
AlSb	0.532	1060
GaAs	0.565	1230
GaP	0.532	1457
InP	0.573	1062
RbF	0.564	795

As seen in Table A.2, six compounds are considered possible nucleation agents for primary Si. Use of any of these compounds presents difficulties for the intended purpose, with their limitations being related to either health hazards or incompatible physical properties. AlAs, AlSb, GaAs, GaP, and InP all present significant health hazards when considering their use in

an industrial application. AlAs and GaAs are known carcinogens, and their use, as with other inorganic arsenic compounds, is heavily regulated [92, 93]. GaP presents similar limitations as AlP, producing toxic phosphine gas when in contact with water, steam, or moisture in air [31]. InP can produce toxic In vapours and partial oxidation products on decomposition (at around 800K) [32]. The main limitation in the use of RbF as a modifier lies on its physical properties. With a melting point of 795 °C, this compound does not solidify before Si; thus, it cannot serve as a heterogeneous nucleation site for Si grains. Given the limitations associated with processing Al-40Si with additions of any of the aforementioned compounds in an industrial scale, this approach was not pursued.

Appendix B

Equilibrium temperatures estimated from DSC

Differential Scanning Calorimetry (DSC) was used to identify the temperatures at which primary Si and the eutectic structure present in Al-40Si melted. Figure B.1 shows the measured heat flow with respect to time and sample temperature during melting and cooling of re-solidified 180-212 μm diameter Al-40Si powders. Four peaks are found in this plot; these are marked in yellow and display temperature and heat data automatically determined by the DSC software.

Plots similar to the one shown in Figure B.1 were produced for scanning rates of 20, 10, 5, and 1 K/s. For each of these plots, the leftmost two peaks, which correspond to the melting of primary Si and the eutectic, were tabulated as the liquidus and eutectic temperatures of Al-40Si when melted at each scanning rate. Figure B.2 presents a summary of the determined temperatures and their corresponding scanning rates (this plot is reproduced from Figure 4.2). Linear regression was done using the data in this plot to determine trendlines that correlate reaction temperature and scanning rate for each primary Si and the eutectic. The trendlines produced by linear regression are shown in Figure B.2 and are presented in Equations B.1 and B.2 in terms of reaction temperature (T_p, T_{eut}) and scanning rate (SR). The constants in each
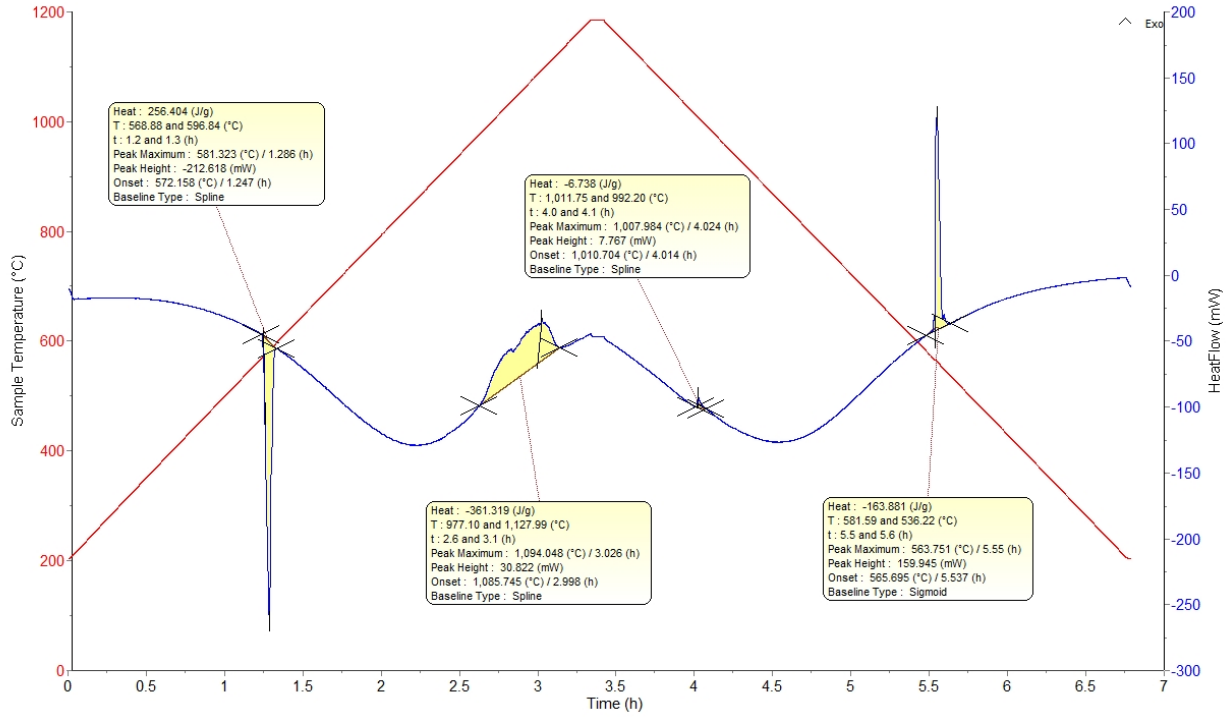
113

Figure B.1: DSC heat flow, re-solidified Al-40Si, 180-212 μm powder diameter sample, scanning rate: 5K/s

Equation B.1 and B.2 correspond to the estimated reaction temperatures when scanning rate is 0 K/s and are thus the estimated liquidus (1076.2 K) and eutectic (576.6 K) temperatures for this alloy.

$$T_p = -2.92 \cdot SR + 1076.2 \tag{B.1}$$

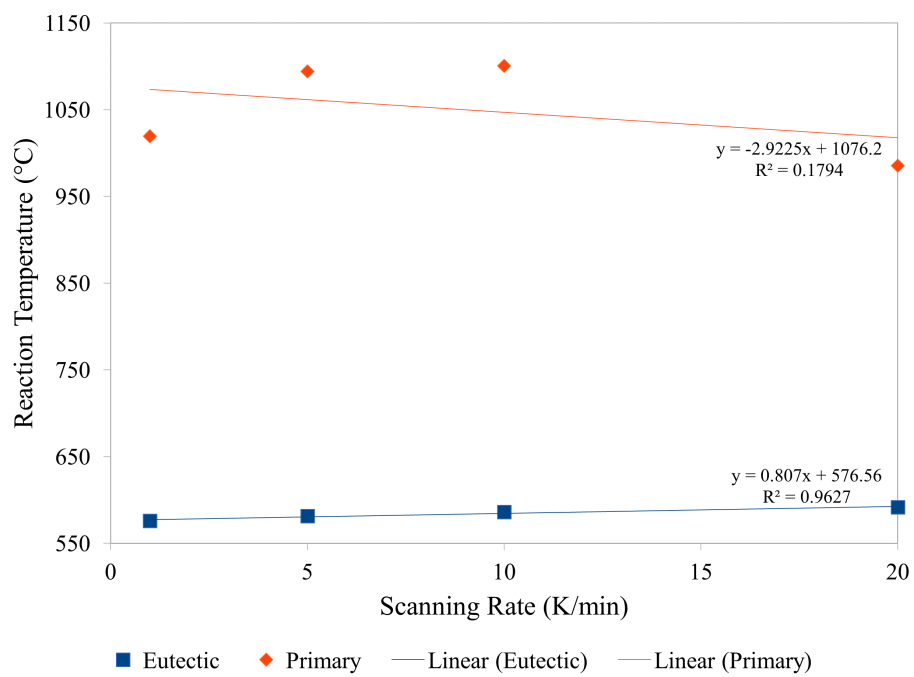$$T_{eut} = 0.81 \cdot SR + 576.6 \tag{B.2}$$

Figure B.2: Reaction temperatures of Al-40Si determined by DSC

Appendix C

Hypothesis testing

This appendix describes the methodology used to perform two-sample t-tests, which were used throughout this work to assess the statistical significance of differences in average and standard deviations measured in two samples. In this work, this approach was used to compare:

- vol% of the same phase/component in two powder sizes of the same alloy, and

- vol% of the same phase/component in samples of the same powder size for two alloys.

Consider the variation in primary Si vol% in Al-40Si as a function of powder size. Primary Si vol% was measured for powders of 90-106, 125-150, 355-425, 500-600, and 710-850 μm diameter. Of these, comparing measured primary Si vol% between 90-106, 500-600, and 710-850 μm powders illustrates the use and interpretation of two-sample t-tests. Equations C.1 and C.2 are used to consider the probability of two sample distributions belonging to the same population.

$$s_p^2 = \frac{((n_2 - 1)s_2^2) + ((n_1 - 1)s_1^2)}{n_1 + n_2 - 2} \tag{C.1}$$

$$t = \frac{\mu_2 - \mu_1}{s_p\sqrt{\frac{1}{n_1} + \frac{1}{n_2}}} \tag{C.2}$$

116

For this set of equations, μ, s, n are the sample average, standard deviation, and size, For each of these variables, the numbered subscript identifies to which sample the variable's value belongs. s_p is the pooled variance of the two samples being compared, and t is the t-statistic. For the three powder sizes being compared, primary Si vol%, standard deviation, and sample size are summarized in Table C.1.

Table C.1: Parameters for two-sample t-tests

Powder size (μm)	μ	s	n
90-106	36.8	5.0	10
500-600	33.9	3.6	10
710-850	32.3	2.2	10

A two-sample t-test, involves an initial assumption (null hypothesis, H_o) that the two samples belong to the same population. In the context of primary Si vol% measurements, the null hypothesis is that the average and standard deviation of primary Si vol% is the same for the two samples being compared. An alternative hypothesis (H_a) represents the possibility of the two samples belonging to different populations (i.e. primary Si vol% is different for both samples). The t-statistic calculated in Equation C.2 represents the normalized deviation between the means of the samples being compared. To decide whether to reject H_o in favour of H_a, t must be compared to a standard t-value. Selection of this t-value depends on the degrees of freedom ($n_1 + n_2 - 2$) of the combined samples and the confidence level desired. In this work, all vol% estimates are based on measurements taken from 10 droplets, resulting in 18 degrees of freedom. A confidence level of 95% is generally considered acceptable for most applications. These factors lead to a t-value of 2.10 [94]. For H_o to be rejected, t must be larger than the t-value. Otherwise, H_o is not rejected. Comparing the data for 500-600 and 710-850 μm powder sizes results in $t = 1.21$, and comparing 90-106 and 710-850 μm powders results in $t = 2.61$. These values indicate that H_o is rejected in favour of H_a for the comparison between 90-106 and 710-850 μm powders, while H_o is not rejected for the comparison between 500-600 and 710-850 μm powders. Thus, primary Si vol% is considered

to be different when comparing 90-106 and 710-850 μm powders, but not when comparing 500-600 and 710-850 μm powders.

Appendix D

Intermetallic compounds in Al-40Si-2.75Fe-2.75Mn-1.5Sc

This appendix contains a summary of the phases detected by X-Ray Diffraction (XRD) and compositions of select intermetallics measured by Electron Dispersive X-Ray Spectroscopy (EDX) in Al-40Si-2.75Fe-2.75Mn-1.5Sc.

D.1   XRD

X-Ray Diffraction was performed on two powder sizes of this alloy (125-150 and 710-850 μm). The resulting patterns are shown in Figures D.1 and Figure D.2. Both patterns show intense α-Al and Si peaks. Additionally, eleven intermetallic compounds were identified. A list of these compounds can be found in Table D.1. The most important finding from these results is the lack of the intermetallics predicted by G-S. Of the detected compounds, four were found in both powder sizes, four were found only in the 125-150 μm powders, and three were found only in the 710-850 μm powders. This division allows to consider the effect of cooling rate on the formation of certain compounds that are not present in both samples, as well as establish which compounds are less sensitive to varying cooling rate.

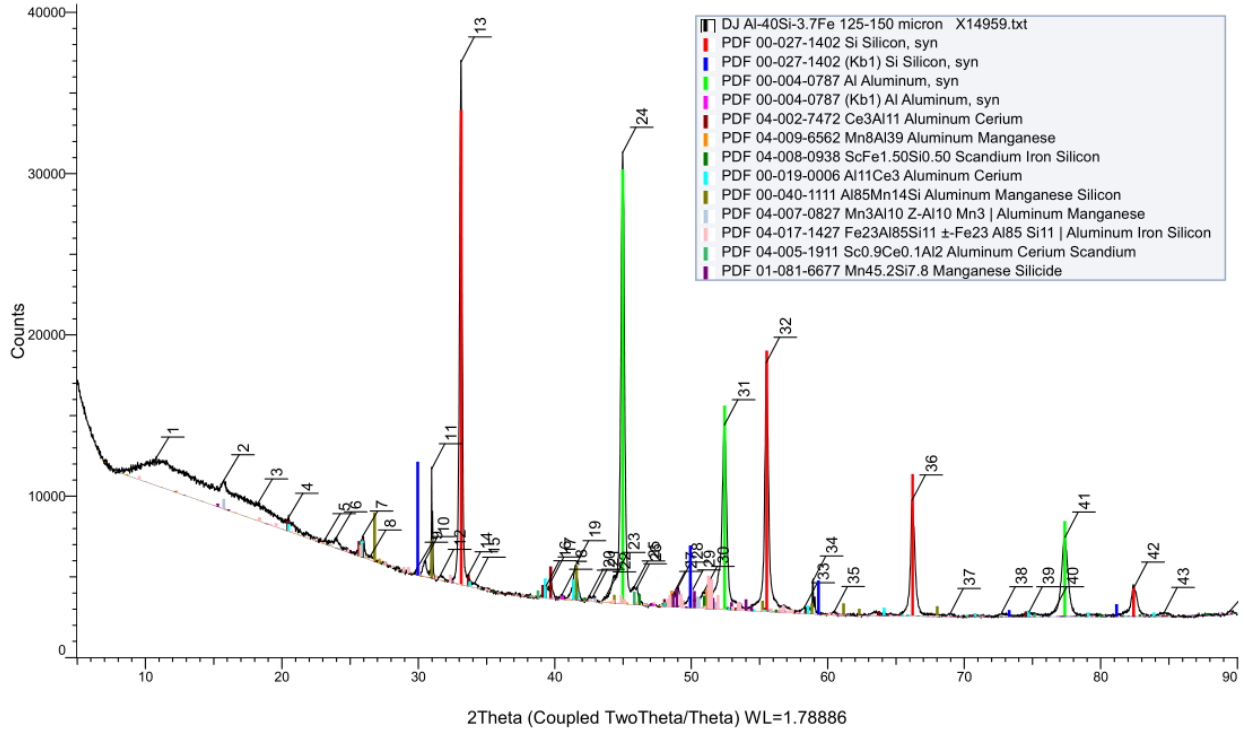Considering the composition of the alloy, the presence of two Ce-containing intermetallic

Figure D.1: XRD pattern of Al-40Si-2.75Fe-2.75Mn-1.5Sc, powder diameter: 125-150 μm

Table D.1: Intermetallic compounds detected in Al-40Si-2.75Fe-2.75Mn-1.5Sc by XRD

Found in both samples	125-150 μm only	710-850 μm only
$Al_{10}Mn_3$	$Al_{11}Ce_3$	$Al_{12.26}Si_{0.28}Fe_{6.46}$
$Al_{85}Fe_{23}Si_{11}$	$Al_{35}Mn_8$	$Al_{0.05}Si_{0.95}Mn$
$Al_2Sc_{0.9}Ce_{0.1}$	$Si_{0.5}Fe_{1.5}Sc$	$Al_{3.73}Si_{2.18}Fe_{2.09}$
$Si_{7.8}Mn_{45.2}$	$Al_{85}Mn_{14}Si$	

compounds ($Al_{11}Ce_3$ and $Al_2Sc_{0.9}Ce_{0.1}$) is curious. In the case of $Al_{11}Ce_3$, the compound could arise from contamination during sieving of the powders. Prior to processing of these powders, the sieves were used on various Ce-containing alloys (Al-40Si-1.5Ce, Al-5Ce, Al-20Ce). While the sieves are cleaned in an ultrasonic bath to dislodge stuck powders, there is always a possibility that powder from a previous alloy remains in the mesh and dislodges during a later sieving cycle. This has been observed in the past with the specific set of sieves used for this alloy, particularly for finer mesh sizes. The origin of the $Al_2Sc_{0.9}Ce_{0.1}$ detected
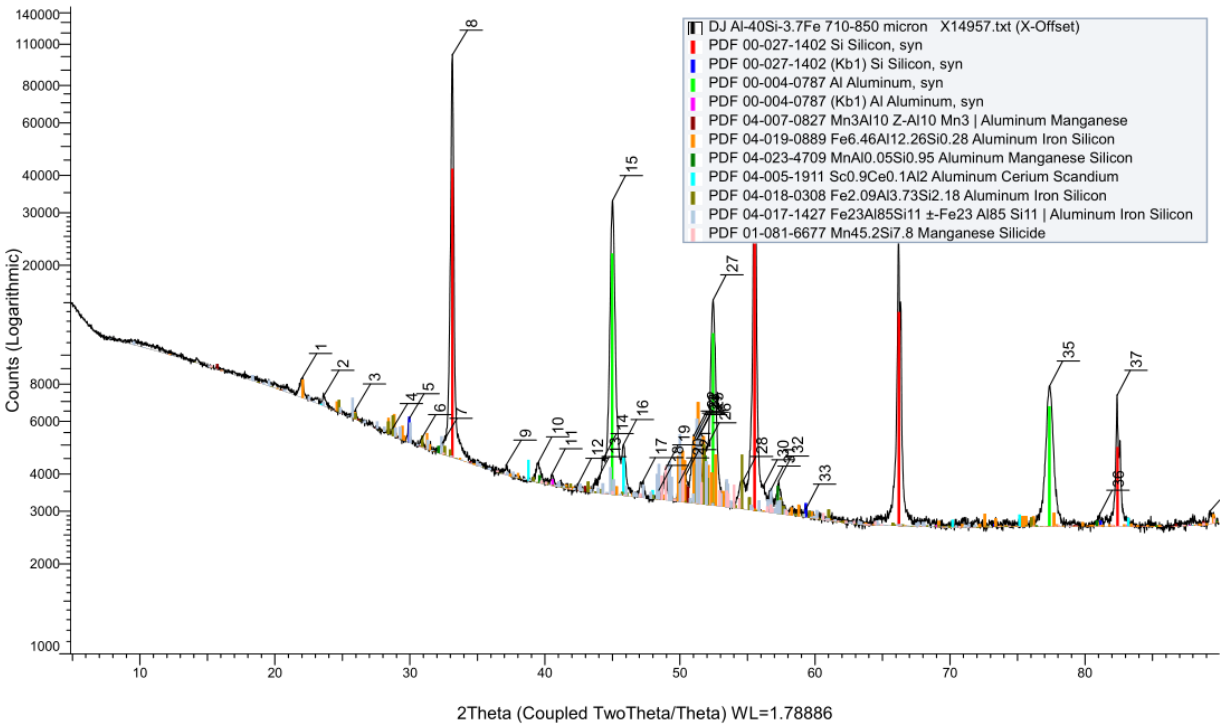
Figure D.2: XRD pattern of Al-40Si-2.75Fe-2.75Mn-1.5Sc, powder diameter: 710-850 μm

is less clear. One possibility is the misidentification of Al_2Sc due to a variation in the lattice parameter of the compound. No definitive explanation for the detection of this compound in these samples.

D.2 Microstructure and localized composition

Figures D.3 and D.4 provide a more detailed look at the eutectic structure of Al-40Si-2.75Fe-2.75Mn-1.5Sc. The eutectic in this alloy contains a variety of features, which vary depending on the powder size and precise location being imaged. Both images share the presence of an Al-Si eutectic structure as a common feature. The presence of this eutectic as a self-contained entity further contradicts the G-S solidification path for this system, which does not predict the formation of a binary Al-Si eutectic. A second common feature can be found

121

in a network of cellular intermetallic and α-Al matrix in both images. While morphology of this intermetallic network slightly varies with powder size, EDX area scans (presented in Table D.2) show a similar chemical make-up in both cases. These compositions are based measurements taken at five distinct locations presenting the cellular intermetallic + α-Al structure for each powder size.
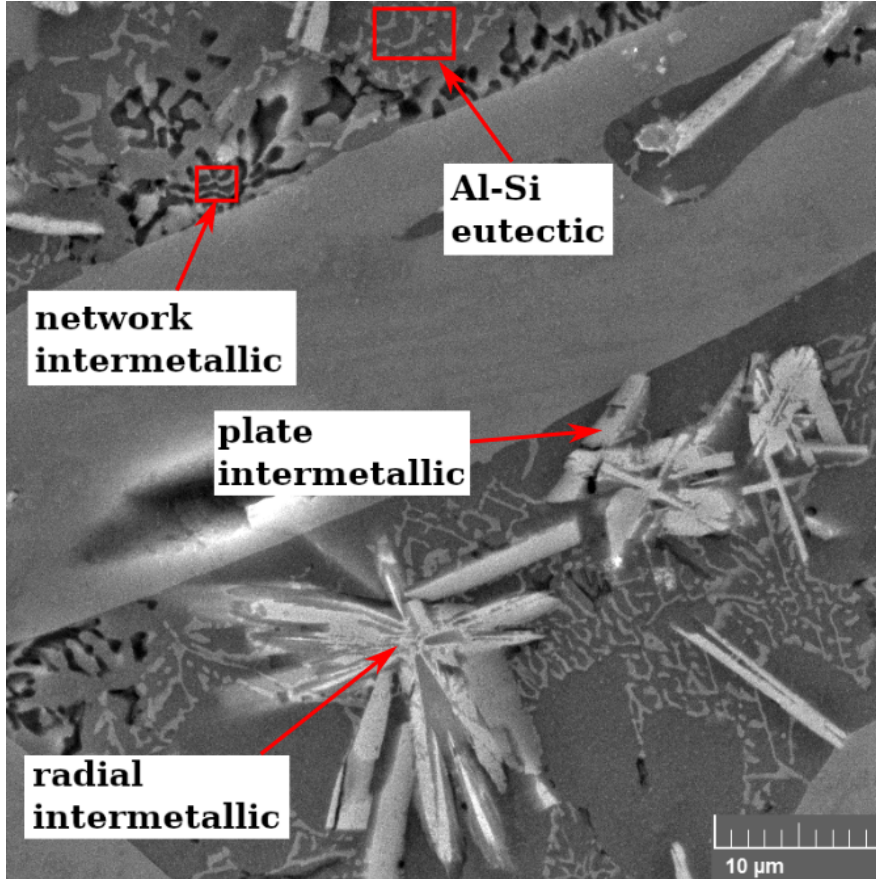

Figure D.3: Eutectic structure in IA Al-40Si-2.75Fe-2.75Mn-1.5Sc, 710-850 μm powder size

Table D.2: Composition of intermetallic network and α-Al in Al-40Si-2.75Fe-2.75Mn-1.5Sc

Powder size (μm)	Al (at%)	Si (at%)	Mn (at%)	Fe (at%)	Sc (at%)
106-125	83.2 ± 1.9	10.2 ± 1.4	2.9 ± 0.3	3.2 ± 0.5	0.6 ± 0.1
710-850	83.9 ± 3.3	9.9 ± 3.8	3.5 ± 0.9	2.2 ± 0.6	0.7 ± 0.9

As the combined intermetallic and α-Al is present in both powder sizes, the identity of the intermetallic is most likely one the compounds detected by XRD in both samples. The
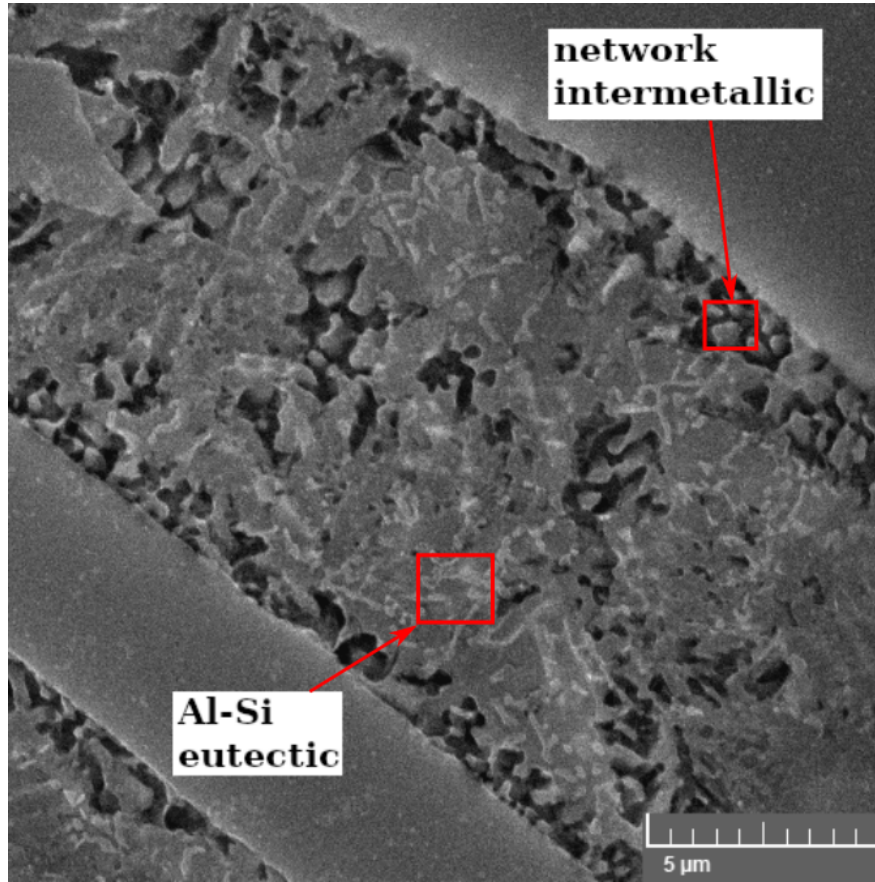
Figure D.4: Eutectic structure in IA Al-40Si-2.75Fe-2.75Mn-1.5Sc, 106-125 μm powder size

first limitation in matching up EDX and XRD results arises in the Sc content found in this structure for each powder size. The 106-125 μm powders contain close to 0.6 at% Sc, while the Sc content in the 710-850 μm powders is inconclusive. Additionally, none of the intermetallics detected by XRD contain all three Mn, Fe, and Sc. This last point in particular opens up the possibility of the structure in question containing multiple intermetallics. Three intermetallic compounds found in both samples ($Al_{10}Mn_3$, $Al_{85}Fe_{23}Si_{11}$, $Si_{7.8}Mn_{45.2}$) can potentially explain the presence of both Fe and Mn in this structure. The Sc content in this structure may be explained by either the single Sc-containing compound found in small powders ($Si_{0.5}Fe_{1.5}Sc$) or the Sc-containing compound found in both samples ($Al_2Sc_{0.9}Ce_{0.1}$). The identity of this last compound is dependent on whether the cellular intermetallic found in 710-850 μm powders truly contains Sc.

Figure D.3 contains two features not seen in Figure D.4. Table D.3 lists the average composition of the radial and plate intermetallic structures shown in Figure D.3. The compositions shown in this table are based on EDX point (plate morphology) and area (radial morphology) scans taken at five locations presenting the relevant structure. Given the fine size of these features, these compositions are assumed to generally describe the chemical make-up of each structure, but they are not intended to reflect the true distribution of these structures. As with the cellular intermetallic, both the plate and radial intermetallics contain Al, Si, Fe, and Mn. This in itself poses the same problem as with the cellular structure, since no intermetallic detected by XRD contains both Mn and Fe. In the case of the radial intermetallic, identification of the compound is even more complex due to the large amount of Sc in this structure. As shown in Figure D.3, the radial intermetallic contains light and dark regions, suggesting the possibility that this structure is made up of two intermetallic compounds. The plate intermetallic appears much more uniform in color and is thus thought to contain a single compound.

Table D.3: Composition of intermetallic structures observed only in
Al-40Si-2.75Fe-2.75Mn-1.5Sc powders of 710-850 μm diameter

Intermetallic shape	Al (at%)	Si (at%)	Mn (at%)	Fe (at%)	Sc (at%)
Plate	55.6 ± 5.1	30.9 ± 3.3	7.9 ± 1.3	5.0 ± 1.5	0.0 ± 0.1
Radial	38.1 ± 3.5	33.6 ± 1.7	9.9 ± 0.4	7.6 ± 0.5	10.8 ± 1.7